Polymer Based Nanocomposites as Multifunctional Structure for Space Radiation Shielding: A Study of Nanomaterial Fabrications and Evaluations

by

Siyuan Chen

A thesis

presented to the University of Waterloo

in fulfillment of the

thesis requirement for the degree of

Doctor of Philosophy

in

System Design Engineering

Waterloo, Ontario, Canada, 2018

Examining Committee Membership

The following served on the Examining Committee for this thesis. The decision of the Examining Committee is by majority vote.

External Examiner	Raghavan Jayaraman Associate Professor
Supervisor(s)	John T.W. Yeow Professor
Internal Member	Nima Maftoon Assistant Professor
Internal-external Member	Xiaosong Wang Associate Professor
Internal-external Member	Michael Pope Assistant Professor

Author's declaration

This thesis consists of material all of which I authored or co-authored: see Statement of Contributions included in the thesis. This is a true copy of the thesis, including any required final revisions, as accepted by my examiners.

I understand that my thesis may be made electronically available to the public.

Statement of Contributions

I hereby declare that I have contributed to the majority of research work in this thesis wherein Chapter 5 includes published article.

Chapter 5 has been incorporated within a paper that has been submitted for publication. The paper is co-authored by Dr. Li, Dr. Nambiar, Dr. Sun, PhD student Mr. Zhang, Dr. Zheng, my supervisor (Dr. Yeow) and myself. Dr. Li, Dr. Nambiar and I developed the methodology and experimental design. Dr. Li and I carried out the characterization experiments, collected and analyzed the experimental data, and I assisted with the writing of the paper. Citation of the article is as follows:

Li, Z., Chen, S., Nambiar, S., Sun, Y., Zhang, M., Zheng, W., & Yeow, J. T. (2016). PMMA/MWCNT nanocomposite for proton radiation shielding applications. Nanotechnology, 27(23), 234001.

My contributions to this thesis include design, development, characterization, testing and analysis of nanocomposites for proton and electron radiation shielding in space application.

Abstract

Radiation shielding in space missions is critical in order to protect astronauts and other payloads from radiation damage. Low atomic-number materials such as hydrogen are proved to be efficient in shielding ionizing radiations, but the relatively poor thermal and mechanical properties compared to metallic alloys has limited their applications. Conventional material aluminum (Al) is widely used in space applications as structural and radiation shielding material. However, the issues related to heavy weight and extra secondary radiation generation make pure metals not suitable for modern space radiation shielding. Currently, conventional shielding materials including Al, high density polyethylene (HDPE), and water have been jointly applied as radiation shielding parts on spacecraft. Disadvantages such as low thermal properties (HDPE), high atomic number (Al) and complex maintenance system (water) have resulted in heavy load and high-cost in space missions.

One approach to replace high atomic number metals is deploying hydrogen rich polymers enhanced with nanofillers associating mechanically strong composite carbon fiber reinforce plastic (CFRP) that has been proposed in this research. Polymer based nanocomposite can achieve improved physical properties such as thermal properties, while at the same time it can provide adequate radiation shielding function with lower weight and less secondary radiation generation. By reviewing nanotechnologies for radiation shielding, multi-walled carbon nanotube (MWCNT) and bismuth oxide (Bi_2O_3) nanoparticle were carried out to enhance properties of poly(methyl-methacrylate) (PMMA). The role of nanofillers embedded in PMMA matrix, in terms of radiation shielding effectiveness, were experimentally evaluated by comparing the proton transmission properties and secondary neutron production of the PMMA/MWCNT nanocomposite and electron transmission properties of PMMA/MWCNT/Bi_2O_3 nanocomposite with pure PMMA and Al.

The results indicate that the addition of MWCNT in PMMA matrix can not only further reduce the secondary neutron production of the pure polymer, but also show significant reduction in weight compared to Al. Furthermore, the adoption of Bi_2O_3 illustrates reduced areal density of nanocomposite over Al under the same electron radiation energies. However, enhanced thermal properties of nanocomposite is required to make it a potential candidate for radiation shielding in space applications. As a result, an optimization of nanocomposites and methods to apply its multiple functions onto CFRP structure have been accomplished. After all, a prototype was designed and produced with improved properties of nanocomposite. The low-cost component has shown potentials to replace conventional radiation shielding material Al alloys with high ratio of radiation shielding effectiveness and weight.

Acknowledgements

I would like to express my first and foremost gratitude to my supervisor, Professor John T.W. Yeow, for his guidance, inspiration and encouragement throughout my PhD career. He is always amazingly supportive and encourages every student to pursue his/her own passionate research topic. At the early stages of my research, I was hesitant to carry out my research topic since it is a bit non-conventional to our lab, and I also felt frustrated when things did not go as expected. However, he rebuilt the confidence in me and made me realize the significance of my work. He also spent much effort exploring the resources that I need for my research. I find him remarkably talented in research and discussing challenges in our meetings is always a rewarding experience. It has been an incredible journey to be part of this research lab and I have enjoyed every minute of it.

I thank all my colleagues work in our lab and all my friends' support, encourage and love me through this wonderful journey.

Lastly, but most importantly, I would like to thank my family for all their unconditional love and encouragement.

Dedication

Dedicated to my beloved parents, Daiguang Chen and Zhihua Yu

Table of Contents

List of Figures

List of Table

Abbreviations

GCR	Galactic cosmic rays
SPE	Solar particle events
TID	Total ionization dose
HZE	High energy and atomic number particles
Z	Atomic number
Al	Aluminum
TRIUMF	Canada's particle accelerator centre
ISS	International Space Station
HDPE	High-density polyethylene
PMMA	Poly (methyl methacrylate)
PEI	Polyetherimide
PSU	Polysulfone
CNT	Carbon nanotubes
CTE	Coefficient of thermal expansion
MWCNT	Multi-walled carbon nanotubes
CFRP	Carbon fiber reinforced plastic
-COOH	Carboxyl
Bi_2O_3	Bismuth oxide
LEO	Low-Earth-orbit
NEO	Near-Earth object
CME	Coronal mass ejections
ICME	Interplanetary coronal mass ejections
GEO	Geosynchronous earth orbit
MEO	Medium earth orbit
BFO	Blood-forming organs
RAD	Radiation Assessment Detector
MSL	Mars Science Laboratory
MEMS	Micro-electro-mechanical systems
PE	Polyethylene
UHMW-HDPE	Utrahigh molecular weight high density polyethylene
C-C	Carbon-carbon
PMP	Poly (4-methyl-1-pentene)
SWCNT	Single-walled carbon nanotubes
DIC	Diagnostic ion chamber
BIC	Backup ion chamber

WET	Water equivalent thickness
PDMS	Polydimethylsiloxane
B–K	Bragg-Kleeman
LDPE	Low density polyethylene
PP	Polypropylene
MAVs	Micro air vehicles
EIS	Extreme ultraviolet imaging spectrometer
PMI	Polymethacrylimide
DPM	Double planetary mixer
FTIR	Fourier transform infrared
DSC	Differential scanning calorimetry
Tg	Glass transition temperatures
TGA	Thermogravimetric analysis
TML	Total mass loss
CVCM	Collected volatile condensable material
WVR	Water vapor regained
RS	Range shifter
SRIM	Stopping and Range of Ions in Matter
WEAD	Water equivalent areal density
LINAC	Linear particle accelerator
AD	Areal densities
RMS	Root mean square
SEM	Scanning electron microscope
MU	Monitor unit
CSDA	Continuous slowing down approximation
BN	Boron nitride

Chapter 1 Introduction

1.1 Background and Motivation

Our space is an extremely dynamic place filled with ionizing radiation, energetic particles and trillions of objects, small and large, travelling at speeds in the range of thousands of kilometers per hour. The source of radiation particles is mainly from galactic cosmic rays (GCR), solar particle events (SPE) and trapped energetic radiation. The challenges of protecting astronauts and the hardware within spacecraft from harmful ionizing radiations during space missions have existed for several decades. The ionizing radiation can result in health hazards and tissue damage when human beings expose to it. These effects may produce immediate or delayed health problems [1-3]. Besides, radiation-induced damage effects on electronic devices are mainly irreversible, such as total ionization dose (TID) effects, displacement damage and single event effects [4].

High in density among GCR and SPE, proton radiation became major concerns in space applications [5]. To shield it, high electron density in atom is key for shielding material. Moreover, energetic electrons trapped in Van Allen radiation belts require high density mass as protection on spacecraft. Another small in quantity but powerful in energy radiation, high energy and atomic number particles (HZE), can barely be stopped by current radiation shielding technologies, thus they can easily pass through spacecraft and deposit energy on bio tissues and electronic devices [6]. When shielding materials activated to shield those ionizing radiations, the interactions between primary radiation particles and atoms of structural shielding materials can produce large quantities of secondary radiations that would cause extra damage effects on astronauts and payloads on spacecraft. This is due to the secondary radiations (neutrons and photons) generated by shielding ionizing radiations (nuclear reactions) which can initiate electromagnetic cascades, and it makes 100% radiation attenuation unachievable [5]. However, the interaction between radiations and matters varies depending on the kinetic energy, charge and collision angle of the primary radiations [6, 7]. Consequently, in order to maintain the normal operation of spacecraft and secure the health of astronauts in manned missions, acceptable radiation dose limit dealt by astronauts have been greatly studied [8]. Applied shielding materials must secure expected radiation dose to be as low as possible so that manned space exploration mission with longer time can be implemented.

According to the shielding principles for space application, a shielding material is considered effective if: 1) It has high electron density in order to increase the electromagnetic interaction

between target electrons and the incident charged particles; 2) It produces fewer secondary radiations in a space environment; 3) It is light in weight to reduce the cost on transportation [9-12]. Therefore, low atomic number (low-Z) materials have attracted wide interests in design of radiation shielding materials for space applications.

Modern spacecraft have equipped various radiation shielding structures and materials including aluminum (Al) [13-15]. Since Apollo missions, Al alloys, such as Al 2219-T87 and Al 6061-T6, are still significant components of shields on spacecraft and satellites due to its light weight and high strength [16].Vastly equipped on International Space Station (ISS), Al structure with areal densities of 2 to 20 g/cm^2 have been interpreted as reference radiation shielding on different parts of ISS. Besides that, new alloys and engineered materials are emerging that have the potential to replace the conventional 2000, 6000, and 7000 ingot metallurgy products. They are the low-density aluminum-lithium alloys, the powder metallurgy processed 7000 series alloys, the aluminum-based metal matrix composites, and metal-polymer hybrid composites. However, developing of state-of-art materials with lower atomic numbers is highly demanding in the future space applications.

New materials and structures are in sight of horizon for space missions. A class of materials with high hydrogen content has been investigated, such as inorganic compounds, water and liquid hydrogen. Due to feasibility and safety issues, they are not suitable to be widely applied on spacecraft [17, 18]. Radiation shielding properties of various polymers have been studied by NASA and other researchers [19]. Pure polymers, such as high-density polyethylene (HDPE), are usually composed of low-Z components (such as hydrogen), which make it appropriate for light-weight space radiation shield [1, 17, 20-22]. Due to poor value in mechanical strength and thermal properties when compared to the metallic counterparts, HDPE can only be applied as an associate shielding layer with Al [23]. Poly (methyl methacrylate) (PMMA) was selected due to its high mechanical and thermal properties over HDPE, and better radiation shielding effectiveness than other advanced polymers (such as polyetherimide (PEI), polysulfone (PSU) and polyimide) [1, 20-22]. Even though, enhancement of physical properties by adopting extraordinary advantages of nanomaterials into polymer matrix is a crucial approach. Numerous studies have shown that the composite materials using nanofillers exhibit enhanced mechanical strength and higher thermal stability in addition to the radiation resistance compared to pure polymer [24, 25].

Different nanofillers including carbon black materials have been reviewed, carbon nanotubes (CNT) was selected as an excellent candidate because of its high mechanical strength and thermal conductivity and negative coefficient of thermal expansion (CTE) [26]. Besides, studies have shown

evidences of proton and electron radiation shielding enhancement by adding CNT in nanocomposites [27, 28]. It was also found that CNT with multiple walls can provide extra stability against radiations, which exhibits high potentials of multi-walled carbon nanotubes (MWCNT) [29-31]. Moreover, based on the shielding theory, high atomic number (high-Z) material, such as bismuth, is good candidate for electron shielding due to its superb ability of absorbing and shielding photons [32-34]. Compared to Al, associating with PMMA polymer matrix, overall weight of high-Z element added nanocomposite is still competitive at the same electron radiation environment.

However, compared to metallic counterpart, Al, physical properties of polymer-based nanocomposite are still not adequate to perform as stand-alone radiation shielding structure. To resolve the inadequate mechanical and thermal properties of nanocomposite, assorting with another structure material, carbon fiber reinforced plastic (CFRP), is a potential method. CFRP have been used in space missions to reduce the overall weight without reducing mechanical properties. It usually is recognized as the one has extremely high tensile strength (1,860 MPa for M55J (6K) composite) compared to Al alloy (310 MPa) [35]. The thermal conductivity of CFRP depends on the direction of carbon fibers, and most carbon fibers used in CFRP can exceed 150 W/m-K in thermal conductivity [36-38]. In comparison, the thermal conductivity of Al is about 155-190 W/m-K [35]. Although CFRP shows advantages over Al, the material cannot provide adequate ionizing radiation protection for itself and payloads enclosed [39]. Therefore, benefitted from outstanding mechanical and thermal properties of CFRP, protection layers with exceeding radiation shielding properties, such as polymer-based multifunctional nanocomposite, can be cohered with the CFRP to form multifunctional structure for space radiation shielding applications.

Investigations of high energy proton and electron radiation shielding properties of nanofiller modified PMMA matrix would potentially inspire broad researches. Thus far, polymers-based multifunctional nanocomposite as radiation shielding for space application has attracted limitedly attentions. However, it should be widely emphasized that polymer-based nanocomposite itself has great potential to be space radiation shielding and the nanocomposite protected CFRP structure would be an appealing alternative to replace conventional material, Al, in various space applications.

1.2 Research Scope

As discussed above, this thesis (Polymer Based Nanocomposites as Multifunctional Structure for Space Radiation Shielding: A Study of Nanomaterial Fabrications and Evaluations) is focused on developing polymer-based multifunctional nanocomposite protected CFRP structure as space

radiation shield which can be used to compete with conventional material, Al. Accordingly, objectives of this research are illustrated in this section:

- **Investigation of Appropriate Material for Radiation Shielding Tests**

PMMA with 1, 3 and 5 wt% MWCNT with carboxyl (-COOH) group (MWCNT-COOH) were fabricated and their physical properties were evaluated. By analyzing characterization results, PMMA/3wt%MWCNT was carefully selected for further fabrication and tests.

- **Proton Radiation Shielding Test**

High energy proton beam (up to 105 MeV) was performed in Canada's particle accelerator centre (TRIUMF). Radiation shielding test process was well-design and illustrated. Proton radiation shielding effectiveness of selected PMMA/3wt%MWCNT nanocomposite was investigated. Compared to reference materials, such as Al, overall weight reduction has accomplished for proton shielding. Less secondary neutron radiation was measured from interaction between primary proton beam and nanocomposite compared to Al and pure PMMA. Characterization of materials were implemented and analyzed before and after irradiation. Details of each achievement have been discussed.

- **Electron Radiation Shielding Test**

Bismuth oxide (Bi_2O_3) nanoparticles were mixed into PMMA/3wt%MWCNT nanocomposite to enhance electron radiation shielding performance. Energies of electron up to 20 MeV used to simulate extreme space environment. As a result, PMMA/MWCNT/Bi_2O_3 nanocomposite can achieve weight advantages over PMMA/MWCNT and Al at various electron energies. Detailed analysis has been discussed.

- **Optimization of Nanocomposite and Bulk Fabrication Process**

Bulk fabrication method of nanocomposite was carried out to produce the radiation shielding layer on CFRP honeycomb structure (a 100 cm × 60 cm panel). Due to thermal expansion concern on PMMA/3wt%MWCNT during thermal cycling test, an optimized design of nanocomposite based on proton and electron radiation shielding test results was conducted. Addition of higher weight percentages (>3wt%) of MWCNT in nanocomposite were analyzed, fabricated and characterized. A well-designed prototype of multifunctional radiation shielding layer was cohered on CFRP

honeycomb structure. Distinctive designs of the optimized nanocomposites have been discussed in detail.

1.3 Thesis Outline

The thesis includes 8 sections:

Section 1 provides an overview of the research background, and also introduces the research motivation and scope.

Section 2 provides literature review on space radiation and its effects on matters followed by an in-depth review on innovative nanomaterials followed by comparison with conventional radiation shielding materials.

Section 3 introduces fundamental ideas on fabrication and material characterization methods used in this research.

Section 4 describes methods of suitable sample selection for radiation shielding tests (proton and electron tests).

Section 5 illustrates proton radiation shielding test followed by secondary neutron generation analysis and characterization of all materials.

Section 6 demonstrates improved nanocomposite for electron radiation shielding and results analysis of characterization and shielding properties.

Section 7 presents scaled-up fabrication method for optimized multifunctional nanocomposite associating with CFRP honeycomb as space radiation shielding.

Section 8 concludes the major contributions in this research and provides advises for future work.

Chapter 2 Literature Review

The radiation environment in space, consisting of trapped radiation belts, cosmic rays, and solar energetic particles is extremely hazardous for astronauts. Currently, most spaceflight missions are still around the Earth, such as low-Earth-orbit (LEO), the shielding provided by the Earth's magnetic field attenuates the major life biomedical effects of space radiation exposures. However, future human space missions will extend to Moon base, a near-Earth object (NEO), such as asteroid, habitations on Mars and outer space. The risks of space radiation will become more severe, as space missions to Mars or other planets require extended radiation exposure time beyond the protection of Earth magnetic field. Currently applied radiation shielding materials are still limited by the inadequate shielding effectiveness, low functions to weight ratio, high cost, and difficulties of manufacturing and handling. Developing innovative multifunctional lightweight shielding materials to sustain longer amounts of time for astronauts is a pressing matter to address the acute risks caused by space radiations.

2.1 Space Radiation

2.1.1 Radiation Sources

Space radiation is one of the most important concerns in space missions due to its harmful effects to the astronauts and the electronics on board. Objects in space sustain radiation particles mainly from three sources: galactic cosmic rays (GCRs), solar particle events (SPE) and trapped energetic radiation. Figure 1 illustrates these three radiation sources.

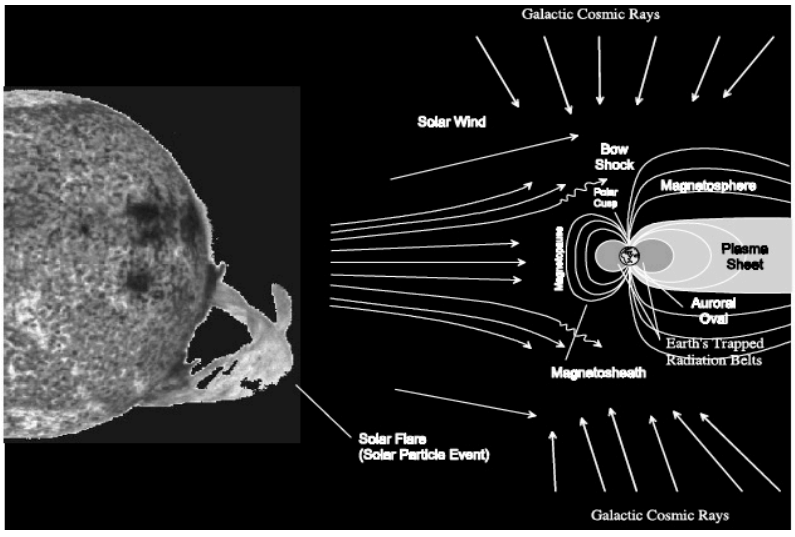

Figure 1: Three main radiation sources in space [6]

GCRs come from outside the solar system and are always present through it. 2% of GCR particles are electrons, while the other 98% of GCR particles are baryons, within which 85% are protons, 14% are α particles and about 1% are high energy and atomic number particles (HZEs). HZEs consist of ions with atomic number from 3 to 28 [5, 40]. The energy of GCRs particles falls mainly in the range of 10s of MeV to 10s of GeV per nucleon. The flux of GCR particles is affected by the solar activities in the solar system and by the magnetic field of Earth in LEO. Figure 2 shows the energy spectrum of GCRs in solar maximum and solar minimum. Near the poles of the Earth, the flux of GCR particles received by spacecraft in LEO reaches a maximum, as the magnetic field lines draw particles toward the earth, and the flux reaches a minimum near the equator, where the particles travel parallel to earth. Moreover, anomalous components, observed in GCR, are partially charged ions with relatively low energy, usually about 20 MeV/nucleon. The anomalous component contains particles from interstellar gas, which are neutral before entering the solar system, and are ionized by solar radiation. Because of the relatively low energy, coupled with weak penetrating ability, anomalous components cause little biological damage effects, and are of less concern [6, 17, 41, 42].

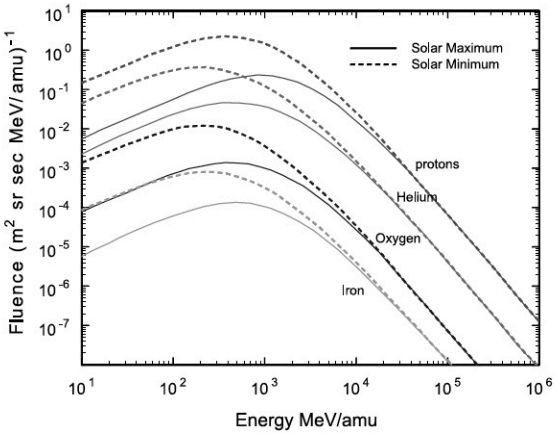

Figure 2: Energy spectrum of GCR in solar maximum and solar minimum [43]

Secondly, there are three main types of SPE: coronal mass ejections (CME), solar flares and solar winds. CMEs are the event of matter eruption from the sun. The matter that is erupted consists mainly of plasma, containing electrons and protons. A small amount of HZE particles with atomic number up to 26 (Fe) are also ejected during CME together with the electromagnetic radiation. The ejections that reach earth are termed interplanetary CME (ICME). The speed of ejected matter ranges from 20 km/s to 3,200 km/s, with average speed of 489 km/s. The duration of CME is in the order of days and is characterized by large fluxes of protons (10^9/cm^2) with broad angle in solar longitude extending from 60° to 180°. Solar activities are observed in an 11-year cycle with solar

maximum and solar minimum phases. SPE and solar flares are always detected in a solar maximum. Solar flares are sudden solar events that can create bursts of energy up to 6×10^{25} J and occur in active solar regions around sunspots. The duration of flare events is in the order of hours and is characterized by relatively large fluxes of electrons (10^7/cm^2 to 10^8/cm^2), with angle in solar longitude from 30° to 45°. Compared to CMEs and solar flares, solar winds are always present in the solar system, comprising of electrons and protons, with energy ranging from 1.5 to 10 keV. The speed of fast solar wind is about 750 km/s and the speed of slow solar wind is about 400 km/s. [44-46].

When protons and electrons from GCR and SPE interact with the Earth's magnetic field and atmosphere, energetic particles will be trapped forming the Van Allen radiation belt (Figure 3). The outer belt ranges from 13,000 km to 60,000 km above the Earth's surface. Particles found in the outer belt are mainly electrons. The inner belt ranges from 100 km to 10,000 km above the ground. Particles found in the inner belt are mainly protons and electrons. Energies of the electrons are less than 5 MeV in the inner belt and go up to 7 MeV in the outer belt. The intensity of the trapped protons decreases as a function of altitude from the Earth, and the energies of protons go up to several hundreds of MeV with major flux lower than 100 MeV (as shown in Figure 4) [47].

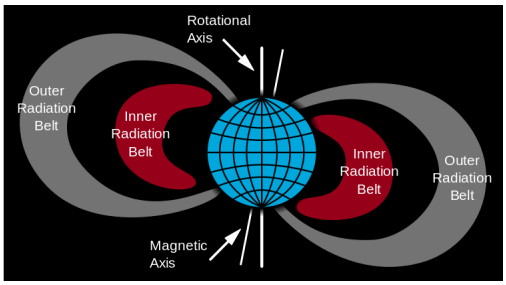

Figure 3: Van Allen Radiation Belt [48]

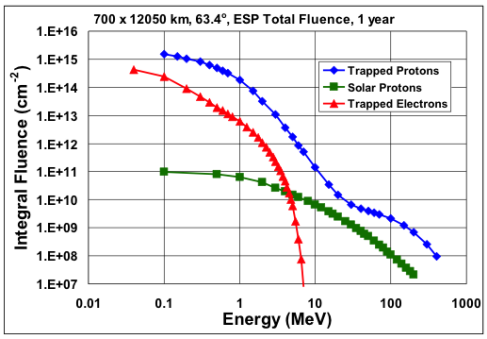

Figure 4: Proton and electron flux in energies [49]

2.1.2 Radiation Environment

Currently, increasing number of planet landing missions are in progress, like lunar and Martian missions. However, the mostly visited areas are still around our earth, such as low earth orbit (LEO), geosynchronous earth orbit (GEO) and medium earth orbit (MEO).

Earth Orbits

LEO has a range from the surface of earth to 2,000 km above the ground, and most current and previous spacecraft orbit within this region. Energetic protons in LEO are predominantly found trapped in the inner Van Allen Radiation Belt with the radiation dose rate of around 1 mSv/year. However, the flux of protons varies according to the change of inclination and altitude of spacecraft orbit. The inclination and altitude dependencies appear in the small inclination (0° to 30°) region, while the flux in medium inclinations (30° to 60°) increases more gradually with the rise of inclination and becomes stable when the inclination is higher than 60° [50]. When the altitude of orbits are ranging from 200 km to 600 km above the ground, the flux increases sharply with altitude and changes become less drastic when the altitude is higher than 600 km [45, 51]. The altitude of the inner radiation belt mostly exceeds the orbit of the International Space Station (ISS) (320 km to 400 km). However, when the ISS travels above the South Atlantic Anomaly region, which is off the coast of Brazil, half of the ionizing radiation energy absorbed in the ISS comes from the trapped protons in the inner belt due to this abnormal drop of geomagnetic field. Typically, electrons in the LEO have energies up to 7 MeV [52] and majority of the protons in the LEO have energies less than 10 MeV, while protons with energies in the range of 10 to 500 MeV form a relatively smaller segment in the proton energy spectrum. One example, as shown in Figure 5, is the proton energy spectrum of the orbit of international space station. It is evident that the proton flux decreased with the increase in proton energy, and protons with energies less than 10 MeV has the most flux.

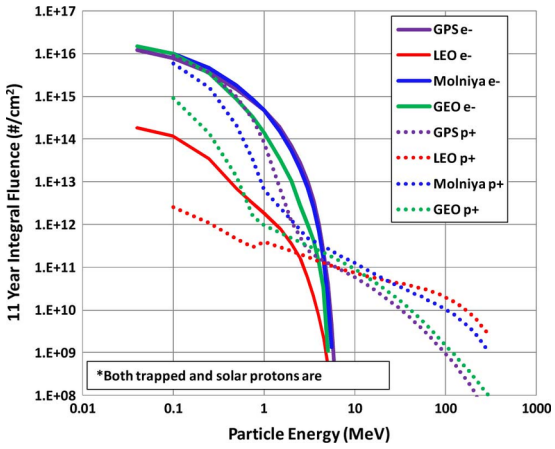

Figure 5: LEO proton and electron energy spectrum for the orbit of international space station [53]

The orbit at 35,786 km is the geostationary (or geosynchronous) orbit (GEO), at which the satellites remain stationary over a single line of longitude. The satellites in GEO are exposed to the outer Van Allen Radiation Belt where the trapped protons from solar flares and cosmic rays can give radiation dose rate about 0.1 Sv/year [45].

The MEO can be identified as the region of space from 2000 km (maximum boundary of LEO) to 35,786 km (altitude of GEO). Telecommunication satellites, designed for geographical positioning systems, are commonly used in this region which lies in between the lower and upper Van Allen belts. Gerald et al. reported that the radiation environment in MEO depends on the altitude and inclination with the dose rate from protons and electrons around 1 Sv/year [51, 54].

Data collected from early NASA missions illustrate that the radiation dose encountered by spacecraft can range from 110 to 1,270 μGy/day in LEO and higher range from 10.3 to 1,154 mGy/day in GEO [6]. Although numerous advanced materials have been used in space applications, the crews in space station can still receive different types of radiation ranging from 80 to 160 mSv/six-months, which is much higher than that of 2 mSv/year on Earth [55].

Lunar Missions

Spacecraft outside the earth's magnetic field are mostly exposed to the particle radiations from the GCR and the SPE, and the radiation effects from nearby planets. For lunar missions, the GCR could create minor risks to astronauts due to the short duration out of shelters. During the non-SPE solar minimum conditions, the dose equivalent rate in interplanetary space on lunar surface can range from 0.5 to 1.4 Sv/year or 1.8 mSv/day behind 40 g/cm^2 of Al and regolith shields [56, 57]. The

probability of suffering the SPE during solar maximum in a 6-month mission is about 1% to 10%. The 95% confidence interval dose would be higher than the 30-day limit for human, and the 30-day limit of dose equivalent for blood-forming organs (BFO) (0.25 Sv) [57]. Moreover, astronauts in extra-vehicular activities on the moon during August 1972, could have been subjected to high SPE (15 Sv to the skin and 2 Sv to the bone marrow) which can lead to acute radiation health effects [3].

Mars Missions

According to a report from National Aeronautics and Space Administration (NASA), areas of maximum exposure to radiation on Martian surface will be the outbound. During a 500-day mission on the Martian surface, astronauts exposed to the radiation with cumulative absorbed dose of 300 mSv may lead to 5% increase in health risks to fatal diseases such as cancer [58]. Simonsen et. al. reported that the mars atmosphere, which can provide 30% GCR dose reduction with the areal density of 16 g/cm^2 of Al, can reduce: (i) the BFO dose equivalent from SPE to about 300 to 350 mSv per event, (ii) the point estimate of dose equivalent from about 570 mSv/year to about 320 mSv/year at solar minimum, and (iii) 220 mSv/year to about 150 mSv/year at solar maximum [59]. Based on the current transit technologies, the space mission from earth to mars takes around 180 days (NASA's design reference mission) [60]. Tripathi et al. provided that the estimate annual GCR dose equivalent is around 1 Sv during the cruise to mars at solar minimum [61]. Table 1 shows the radiation dose equivalent for both of Martian surface and cruise to Mars. Moreover, the Table 2 illustrates the sub-surface dose equivalent rate on mars. These data were achieved by the Radiation Assessment Detector (RAD) on the Mars Science Laboratory's (MSL) Curiosity rover under proper shielding in space [58]. Figure 6 shows the approximate radiation dose comparison during different periods.

Table 1:Overview of radiation environment in Mars during 2012–2013 solar maximum (GCR and SPE) [58]

	Dose-equivalent rate (mSv/day)	Medium-size SPE dose equivalent (mSv/event)	Total mission dose equivalent (mSv)
Mars surface (500 days)	0.64 ± 0.12	0.025	320 ± 50
Cruise phase (2 X 180 days)	1.84 ± 0.30	1.2 to 19.5	662 ± 108

Table 2: Overview of sub-surface radiation in Mars

Depth below surface	Effective shielding mass (g/cm^2)	GCR dose-equivalent rate (mSv/year)
Mars surface (RAD)	0	232
–10 cm	28	295
–1 m	280	81
–2 m	560	15
–3 m	840	2.9

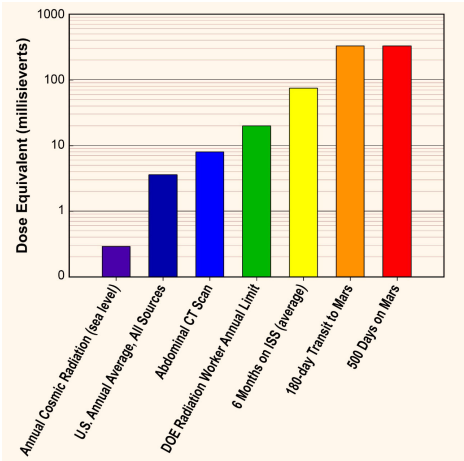

Figure 6: This chart compares the radiation dose equivalent for a 500-day stay on Mars to the dose associated with a 180-day journey to Mars, a 6-month stay on the International Space Station and several Earth-based sources of radiation. Image credit: NASA [58].

2.1.3 Effects of Space Radiations

Ionizing radiations can result in health hazards and causes tissue damage when exposure to it. However, the implications of such exposures are related to factors of radiation type, radiation energy level, the absorbed dose, exposure time and so on. Cosmic radiation imposes important safety concerns for space exploration missions. Several studies have speculated the radiation risks associated with exposure to both GCR and SPE [1, 2]. The radiation-induced health risks include carcinogenesis, cardiac problems, cataracts, and other acute radiation syndromes [1]. Damage to

neuronal system has been a potential concern related especially to the heavy ions present in the GCR.

High-energy particles affect biological tissue by depositing energy and inducing damage effects. These effects may produce immediate or delayed health problems. First, the interaction between the projectile particles and the cells may result in cell death or irreparable modifications to the genetic material (e.g., DNA mutations) [62]. Secondly, even for a relatively low dose (i.e. no short term damage effects are evident), due to exposure to low energy particles, or short exposure time or type of radiation, the cumulative dosage may result in slight aberration of chromosomes inducing delayed effects, such as organ degradation (cataract, heart disease, etc.) and carcinogenesis [4].

As introduced in previous section, exposure radiation dose varies in different space environment. It is still a critical need in quantifying and elucidating the risks of space radiation induced effects. Risk assessment on astronauts during multiple space missions has been studied [8, 63-65]. This has resulted in dose limits guidelines of radiation exposure (Table 3).

Table 3: Example career effective doses limits for up to1 year missions for a 3% risk of exposure-induced death (REID) and estimates of average life loss if death occurs [8]

Age in years	Dose Limit-Male Astronauts (Average Life-lose Per Death in Years)	Dose Limit-Female Astronauts (Average Life-Loss Per Death in Years)
25	520 mSv (15.7)	370 mSv (15.9)
30	620 mSv (15.4)	470 mSv (15.7)
35	720 mSv (15.0)	550 mSv (15.3)
40	800 mSv (14.2)	620 mSv (14.7)
45	950 mSv (13.5)	750 mSv (14.0)
50	1150 mSv (12.5)	920 mSv (13.2)
55	1470 mSv (11.5)	1120 mSv (12.2)

Shielding and structural materials in spacecraft protect astronauts and devices from hazardous radiations to reduce exposure radiation dose. However, the interactions between primary radiation particles and atoms of shielding and structural materials produce large quantities of secondary radiations that cause damage effects [6, 17, 66, 67].

When primary radiation particles from the GCR, the SPEs and in the trapped radiation belt pass through spacecraft and launch-vehicles, nuclear interactions occur and produce secondary radiations (neutrons, photons and electrons), the energy of which varies from 0.001 to 5 GeV.

There are two types of nuclear interactions: target fragmentation and projectile fragmentation. The interaction varies depending on the kinetic energy, charge and collision angle with the primary particles. γ-rays and neutral pions produced in these nuclear reactions can initiate electromagnetic cascades [6, 7].

(i) Target fragmentation: The target fragmentation always happens when trapped protons of GCR protons interact with a heavy nucleus (Al nuclei of structural spacecraft material for instance) or with carbon and oxygen nuclei of human tissue.

(ii) Projectile fragmentation: The projectile fragmentation usually happens when HZE particles interact with target nuclei. The by-products are high-energy secondary neutrons and protons. The fragmented particles retain much of the kinetic energy of the primary HZE particles and they keep interacting with remaining materials, causing continuous nuclear reactions.

In summary, due to the energy deposition from the injected particles and the nuclear damages in the particle-target interaction process, the high-energy radiation particles can induce damages to the structural materials and the electronic components in the spacecraft [6]. In manned space missions, exposures to high-energy particle radiation have alarming health concerns such as carcinogenesis, cardiac problems, cataracts, and damages to the neuronal system [62, 68-71]. Thus, radiation shielding is an important design criterion for materials used in space exploration studies.

2.1.4 Ionizing Radiation Shielding Principles

Particle radiations such as proton and HZE radiation are considered to contribute the most to the absorbed dose in space missions [6]. Furthermore, due to the existence of high-Z material on spacecraft, secondary radiation including electrons and neutrons is another shielding concern. By studying the different physics principle, specific shielding principle should be followed when designing space radiation shields.

(i) Shielding Protons and HZEs

In order to shield protons and HZE particles efficiently, shielding materials should have high electron density, maximize the probability of projectile fragmentation as well as minimize the shielding atoms' fragmentation.

Proton and HZE particles are positively charged particles with masses greater than thousands of times that of an electron. The nucleus occupies only 10^{-5} of the atom's volume. Therefore, in the

process of protons and HZE particles passing through matter, they rarely strike a nucleus, and most of the energy is lost by ionizing or exciting atoms in the material through the interaction with electrons. As a result, the most important consideration for proton and HZE particle radiation shielding is to find materials with high electron density. The electron density is defined as the number of electrons per unit space and it can be calculated through equation below [9, 72].

$$Electron\ density = \rho N \frac{Z}{A};$$

where, ρ is the density of the material; N is the Avogadro's number: $N = 6.022 \times 10^{23}$; Z is the atomic number of the material; A is the atomic weight (A = Z + number of neutrons in the nucleus). According to the above equation, there are two key factors that affect the electron density of materials. One is the mass density of the material, and the other is the ratio of Z/A. For space exploration applications, materials should be as light as possible with low mass density. Thus, the factor Z/A is an important factor for designing effective shielding materials against proton and HZE particle radiation. The higher the ratio of Z/A, the more efficient the element's shielding. The curves in Figure 7 show the calculation results of Z/A corresponding to Z of atoms from Z = 1 to Z = 90. It is found that hydrogen atom has the highest ratio of Z/A, which is more than 50% that of other atoms.

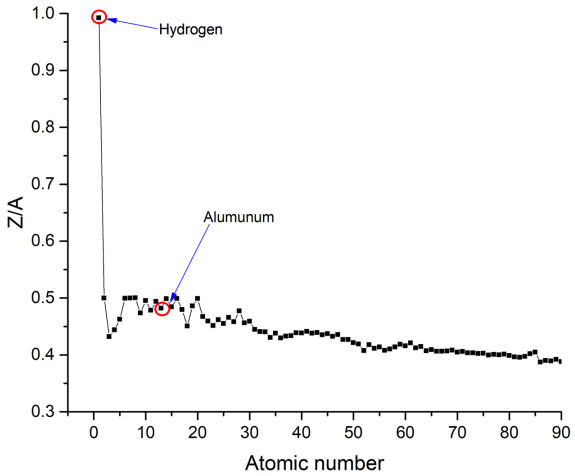

Figure 7: Calculation of Z/A for atoms with atomic number Z from 1 to 90

The second consideration regarding proton and HZE particle radiation shielding material design is to maximize the probability of projectile fragmentation and to minimize the fragmentation of the target atoms. Although protons and HZE particles lose their energy mostly through the interactions

with electrons, nuclear reactions may occur between the incident particle radiations and nuclei of the target material (for e.g., structural materials used in spacecraft) when incident particles have sufficiently large kinetic energies. The nuclear interaction including elastic and inelastic collisions is approximated by the Bradt–Peters equation:

$$\sigma = \pi r_0^2 c_1(E)(A_P^{\frac{1}{3}} + A_T^{\frac{1}{3}} - c_2(E))^2 \ ;$$

where, σ (the total fragmentation cross section) is proportional to $A_T^{\frac{1}{3}}$ which represents atomic mass of the shielding material. This equation suggests lighter the material, smaller the nuclei it has, more nuclear interactions will happen, and thus more effective the material can stop incident GCR ions. However, a cascade of secondary emissions, such as electrons, light ions, gamma rays and neutrons, will occur from nuclear collisions and fragmentation when incident GCR interact with radiation shielding materials [23].

(ii) Shielding Electrons

It is similar to other heavy charged particle radiations, Coulomb interaction plays a key role when electron passing through matters. However, compared to positively charged ions, electron particle collide have the equal mass which results in billiard-ball collisions that can produce much more scattering. For electrons have energies greater than 10 keV, they have larger energy-loss per collision. This means much longer range and lower ionization density electron has in shielding materials compared to positive ions [73].

Regarding low energy electrons, Coulomb interaction with positively charged nucleus bends the electrons results in generation of bremsstrahlung radiation which refers to secondary photons. The energy of photon highly depends on atomic number Z, scattering angle and energy of incident electrons. The probability for energy loss due to bremsstrahlung radiation compared to ionization strongly depends on Z, as shown in equation:

$$\frac{Z_{radiactive}}{Z_{electronic}} \approx \frac{ZE}{800MeV} \ ;$$

The equation indicates that high-Z materials (Z = 80-90) can produce greater quantity of photons than low-Z ones which stop electron mainly by ionization when shielding high energy electrons (10-100 MeV) [10]. As a result, high-Z materials can achieve more attenuate of electron energy since more energy deposit into matters (collision) and carried away by secondary radiation

generation (radioactive); however, for low-Z materials, less electron attenuation but less secondary radiations (mostly Auger electrons and Bremsstrahlung radiation) are expected [74, 75]. To effectively shield electron radiation, adopting advantages of both high- (i.e. high stopping power) and low-Z (i.e. less secondary radiations) materials into one component/composite is an appropriate approach [28, 76, 77].

(iii) Shielding Secondary Radiations

As introduced above, secondary radiations from proton interacting with matters are much harmful than that of electron radiation because of the neutral charged neutrons which will not be affected by negatively charged electron field. For neutron shielding, the typical strategy consists of two steps. First is to slow down the fast neutrons to thermal energies with energy about 0.025 eV. This can be achieved by applying light elements to shielding applications. Hydrogen is particularly effective because of the maximum energy transfer from neutron to hydrogen nucleon in the collision. Suppose the energy Q is transferred to a nucleus of mass m in a single elastic collision with a neutron of atomic mass M and energy E_n, the equation below can be used to describe the relation between Q and E_n.

$$Q = \frac{smME_n}{(M+m)^2} \ ;$$

The atomic mass of a neutron is 1 (M = 1), for different atomic masses of different atoms. Only when m = 1 (hydrogen atom) can the maximum energy (all the energy of the neutron) be transferred through the collision process. By the increase of the atomic mass, the energy transferred decreases (Figure 8). The second step is to absorb the thermal neutrons using materials with high thermal neutron captures cross sections. Carron, N.J. et al. have shown the stable isotopes with relatively large thermal cross sections. From the results, all isotopes with capture γ-ray produced may require extra photon radiation shielding. In comparison, B_{10}, He_3 and Li_6 capture thermal neutrons through (n; α) reaction without emission of γ-ray [11, 12, 78, 79].

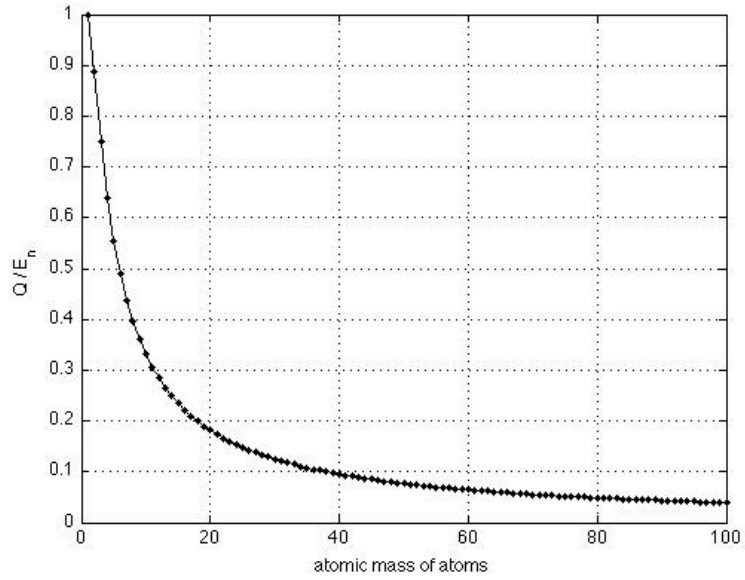

Figure 8: Q/E_n vs. atomic mass [11]

2.2 Conventional Reference Materials

In order to overcome various limitations and maintain the normal operation of spacecraft electronics and to secure the health of astronauts in manned missions, some materials have been developed [71, 80, 81]. In this section, conventional materials including Al alloys are discussed.

Aluminum Alloys

For more than 50 years, Al and its alloys have been the primary structural material for space applications: satellites, rockets, spacecraft and launch vehicles. Al is lighter than other heavy metals, which can reduce the cost in space applications, and also has the ability to endure the stresses that occur during launch and operation in space. Al has been used in space missions including the Apollo missions, Skylab, the Space Shuttle, and the international space station. Since Apollo missions, Al alloys, such as Al 2219-T87 and Al 6061-T6, are still significant components of shields on spacecraft and satellites due to its high strength [16]. The Al alloys are the main structure on Whipple shields, which can provide protection against small size debris and meteoroids. The Figure 9 shows the Al sheet shields the projectile with velocity of 6.7 km/s.

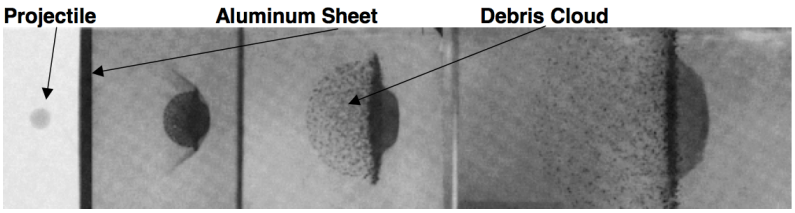

Figure 9: This sequence of high-speed x-ray photography shows the high velocity impact of a 3/8" (9.53 mm) aluminum projectile, penetrating a 0.2753" thick aluminum sheet. The projectile is traveling at 14976 mph (6.7 km/sec). Space debris and micrometeorites are a significant threat to spacecraft and satellites [82].

New alloys and engineered materials are emerging that have the potential to replace the conventional 2000, 6000, and 7000 ingot metallurgy products. They are the low-density aluminum-lithium alloys; the powder metallurgy processed 7000 series alloys, the aluminum-based MMCs, and metal-polymer hybrid composites. Incremental improvement in yield strength of aluminum alloys is shown schematically in Figure 10, in specific stiffness in Figure 11.

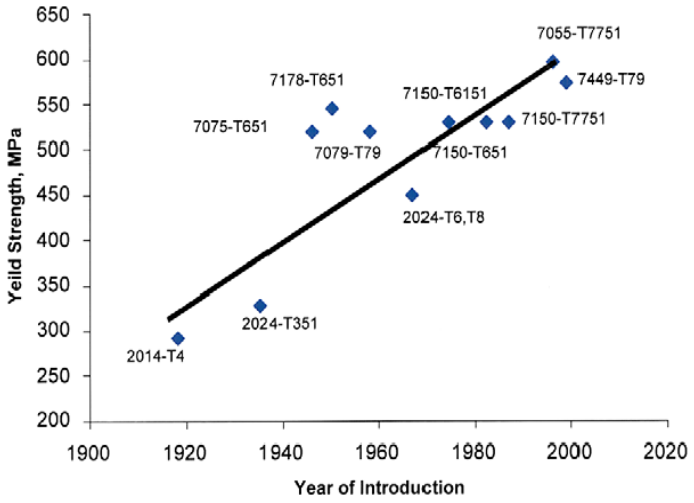

Figure 10: Plot of yield strength for new Al alloys as a function of the year of introduction [83].

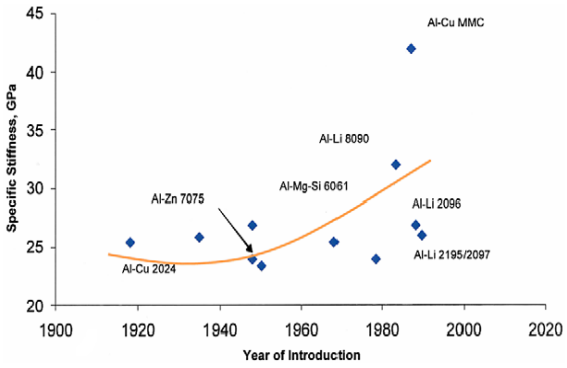

Figure 11: Plot of the density normalized modulus of Al alloys as a function of the year of introduction [83].

Regarding radiation shielding, Al has been conventional shielding on spacecraft for years [14]. Its shielding effectiveness has been vastly studied as a standard shielding material in space applications [15]. In manned space mission, applied material for radiation shielding should be able to achieve radiation-dose attenuation rate of more than 50%. Typically, 2-5 g/cm^2 (areal density) of Al is used as radiation shielding walls on spacecraft, but about 20 g/cm^2 of Al is equipped as effective shield in several parts on ISS to protect specific payloads, which is able to fully stop 100 to 200 MeV proton radiation (Figure 12). This shielding is therefore able to efficiently protect ISS from trapped radiations and SPE [13]. Another study suggests the effective 20 g/cm^2 Al shielding for transition from Earth to Mars, and half shielding material is acceptable on Martian surface.

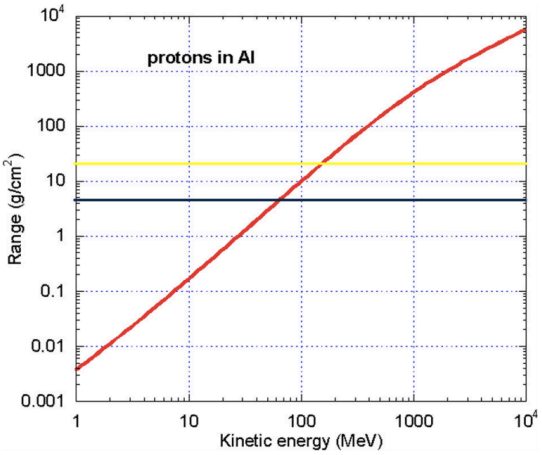

Figure 12: Energy-range relationship for protons in aluminum. Horizontal lines represent typical thickness of the Al spacecraft walls (5 g/cm^2, green line) and the effective thickness due to the presence of payloads and racks (20 g/cm^2, yellow line) [13]

However, due to high atomic number, Al is high in weight and producing more secondary radiations than low-Z materials. Disadvantage of heavy weight will increase space mission cost and reduce the duration due to the extra consumption of the fuel. Massively generated secondary radiations, such as photons, electrons and neutrons from interaction between protons and metallic atoms will result in further damages and extra radiation dose to the loaded devices and astronauts.

2.3 Requirements for Alternative Radiation Shielding Materials

It has now become a priority to try and find materials that can effectively replace Al as a radiation shielding material. The alternative radiation shielding materials should provide sufficient, sometimes an improved protection against exposure to hazardous space radiations. This section will discuss about other requirements than radiation shielding for the new materials.

(i) Thermal Properties

The main environment effects for the devices in space consist of incoming energy from the sun and the heat radiated from the device-electronics. The heat sources from spacecraft include batteries, photovoltaic cells, radioisotope thermoelectric generator, thermal control systems, science instruments and etc. The power supply systems for components on spacecraft also generate heat. Moreover, the spacecraft and the electronics are exposed to sunlight that is about 25% stronger in space than on the ground [84]. In the space environment, vacuum and abrupt load changes at eclipses result in heat dissipation different from that on the earth's surface, which contains oceans and atmosphere as heat sinks. For instance, typical day-night temperature variation on Earth, with a continental climate, is about T_{mean} ±10 C° with an annual mean of $T_{annual,\ mean}$=15 ℃, whereas those values are ±100 ℃ and 1 ℃ on the Moon respectively, and nearly the same on an artificial satellite, or an EVA suit, all being exposed to the same external environment [85].

Currently, the spacecraft is designed and built with a thermal control system that keeps the astronauts and devices in a comfortable environment. The solution to the temperature control problem is a good thermal design (taking decisions to achieve the goal), in order to: (i) Protect the equipment from damaging hot temperatures, either by proper heat insulation from external sources, or by proper heat removal from internal sources. One of the applications is thermal protection system (TPS) during ascent and descent through atmospheres, where surface temperatures may exceed 1,200 ℃. (ii) Protect the equipment from damaging cold temperatures, by proper heat insulation from external sinks, by enhanced heat absorption from external sources, or by heat release from internal sources. Every non-inert system must dissipate heat to the environment (to

compensate entropy generation within), because thermal buffering is impractical in the long term. Consequently, thermal control system is basically to make spacecraft operating under a proper environment. Table 4 shows the operational temperatures on spacecraft.

Table 4: Operating temperature of components on spacecraft

Component/System	Operating Temperature (°C)	Survival Temperature (°C)
Digital electronics	0 to 50	-20 to 70
Analog electronics	0 to 40	-20 to 70
Batteries	10 to 20	0 to 35
IR detectors	-269 to -173	-269 to 35
Solid-state particle detectors	-35 to 0	-35 to35
Momentum wheels	0 to 50	-20 to 70
Solar panels	-100 to 125	-100 to 125

Heat transfer refers to the energy transmission process from one area to another via energy carriers. In gas phase, gas molecules can carry energy via random molecular motion (diffusion) or via an overall drift of molecules in certain direction (advection). Similarly, in liquids, heat can be transferred via diffusion or advection of molecules. In solids, phonons and electrons are the carriers of energy.

In any solid polymer, phonons, electrons and photons can transport energy. Because of the insulator property of polymers thus its electrons cannot move freely, phonon, which is the quantum mechanical quantized modes of vibrations energy, plays a major role in the heat dissipation [86]. From the general overview, it is well established that low thermal conductivity is usually a characteristic of pure polymers. Therefore, enhancement of thermal conductivity in polymer matrix is of importance to maintain material temperature within designed working temperature.

(ii) Light-weight

Applying materials with low areal density would help reduce fuel costs, as fuel can be conserved for each payload. Especially for functional structures on spacecraft, such as radiation shielding components, light in weight will allow more applicable devices and astronauts to be added into payload. For evaluating different materials in regard to density requirements, a function to weight ratio is considered. The materials with higher ratios will be lighter than their competitors, while achieving the same level of radiation shielding function. An example of an excellent shielding material is the usage of hydrogen. Although hydrogen is the most efficient radiation shielding

element with light-weight advantage, its application in space is limited due to the unacceptable processing, difficulty to compress hydrogen into liquid or solid form and heavy equipment to contain it. This results in much more weight disadvantage over Al as shielding material.

(iii) Long lifetime

Besides light-weight function, materials possess relatively long service lifetime has been achieved. For example, the digital micro-mirror devices, which are arrays of micro-electro-mechanical systems (MEMS) commonly used as slit-masks in multi-object spectrometers that are scientific instruments on Hubble Space Telescope, can have up to five years of lifetime in shielded spacecraft during space missions [87].

Under more extreme conditions, the ordinary materials, such as polymers, may not be able to maintain their properties that make them attractive candidates under conditions on Earth. An effective radiation shielding material should not only attenuate projected radiation particles, but should also show strong resistivity against radiation damage effects. A material that degrades quickly is not a reliable shield for long-term space mission. Polymers being irradiated by different types of radiation can display damage effect, such as scission and crosslinking of the polymer chain, micro-cracking within the molecular network, and mass loss. All of these effects can alter the composite's properties and degrade the performance of materials from their original design.

(iv) Low cost

As discussed above, due to the most of materials and components possess heavy in weight and short lifetime, the maintenance missions have to be implemented almost every year, which is additional mission cost. Maintenance missions need to be supported by advanced spacecraft, such as Space Shuttle, which was a reusable LEO spacecraft in U.S., has the payload capacity of 27,500 kg. Another spacecraft Saturn V, which was an American rocket, can load 140,000 kg to LEO, and in order to achieve the mission, cost was more than 13,000 USD/kg [88, 89]. Nowadays, a reduction of cost per kg is expected by development of reusable launch system from SpaceX [90]. Moreover, the cost of material fabrication should also be counted as well.

(v) Material compatibility

Some shielding materials can be used as a protective material when substrates or devices are required to be protected. In order to be a promising candidate for space radiation, the shielding material should have adaptability to a variety of space environment and good compatibility with the

substrates structures, such as carbon fiber reinforced plastic (CFRP), in order to sustain long-term protection, some adhesive materials can be applied while the adhesion between coating and substrate is not achievable. Thus, the compatibility among shields, substrate and adhesive (if applied) need to be evaluated, which depends on three factors: the feasibility of bonding techniques, the bonding strength of each technique, and the space environment effects on the bonding materials.

2.4 Multifunctional Nanocomposite for Space Radiation Shielding

According to the shielding principles and the requirements discussed above for space applications, a shielding material is considered effective if: 1) It has high electron density in order to increase the electromagnetic interaction between target electrons and the incident charged particles; 2) It produces fewer secondary particles in a space radiation environment; 3) It is light in weight to reduce the cost on transportation and power, and 4) It has proper thermal properties. Therefore, low atomic number (low-Z) materials are widely considered in the design of radiation shielding materials. The elements with atomic number $Z \leq 6$ are usually considered to be the low-Z elements, and thus, the materials that are composed of these low-Z elements (low-Z materials) are widely considered to have an optimal balance between the four requirements.

2.4.1 Low-Z Materials

(i) Hydrogen Compounds

Hydrogen is considered as the most efficient shielding element. The hydrogen atom has the highest Z/A (the atomic weight/atomic number of the material) value (Z/A=1) and contains no neutron in the nucleus. Thus, hydrogen rich materials are high in electron density and elicit no secondary neutron production. Instead of using pure hydrogen, various hydrogen compounds are studied for designing radiation-shielding materials with high hydrogen content. For example, Metallic hydrides: LiH, BeH_2, MgH_2, $LiBH_4$, $NaBH_4$. Hydrogen content, shown as a weight percentage, of metallic hydrides and their densities are listed in Table 5. As a result, LiH, which is an inorganic and colorless compound, is mostly considered and $LiBH_4$ is proposed as a potential material to be studied [17, 18].

Table 5: Density and hydrogen weight percentage of metallic hydrides [17]

Material	LiH	BeH_2	MgH_2	$LiBH_4$	$NaBH_4$	TiH_2	ZrH_2
Density (g/cm^3)	0.78	0.65	1.45	0.66	1.07	3.75	5.56
wt% of H	12.7	18.3	7.7	18.4	10.7	4.04	2.16

Hydrogen and its compounds are considered as the most efficient shielding element due to its high Z/A value, but the application of pure hydrogen and water is limited by the difficulties of storage, transportation, maintenance, and related safety issues [17]. After that, researchers have investigated hydrogen storage materials; however, the experimental results are preliminary and not repeatable. Some compounds like BeH_2 has uncertainties in reactivity and toxicity, so it is also not considered [18]. Besides, the safety issues limit the feasibility of LiH for space applications. Thus, the feasibility and safety issues of shielding materials are important concerns.

(ii) Hydrogen Rich Polymers

Pure polymers are usually composed of low-Z component, which makes them be suitable for space radiation shielding [17]. These materials have weight advantage compared to metallic materials when exposed to the high-energy particle radiation in space. Commonly used polymers in space include epoxy resin, polyethylene (PE), polyetherimide (PEI), polysulfone (PSU), polyimide and PMMA [1, 20-22].

Furthermore, Ultem 1000 PEI is an amorphous polymer with high strength and good flame and heat resistance. It is also hydrolysis resistant with high resistance to acidic solutions and repeated autoclaving cycles. The density of Ultem 1000 PEI is 1.128 g/cm^3. Its tensile strength is 16,500 psi (about 113.8 MPa) and its deflection temperature is 200 °C [91]. Another structural polymer, polysulfone, possesses high glass transition temperature (above 190 °C) which benefits broadened working temperature of -100 °C to 190 °C [92]. However, compared to PE, both PEI and PSU radiation shielding effectiveness advantages over Al when shielding GCR are 11% less (Figure 13) [93]. Besides that, low content of hydrogen in polyimide results in poor radiation shielding effectiveness, even it is known as its super high working temperature (above 500 °C) and tensile strength (231 MPa) [94].

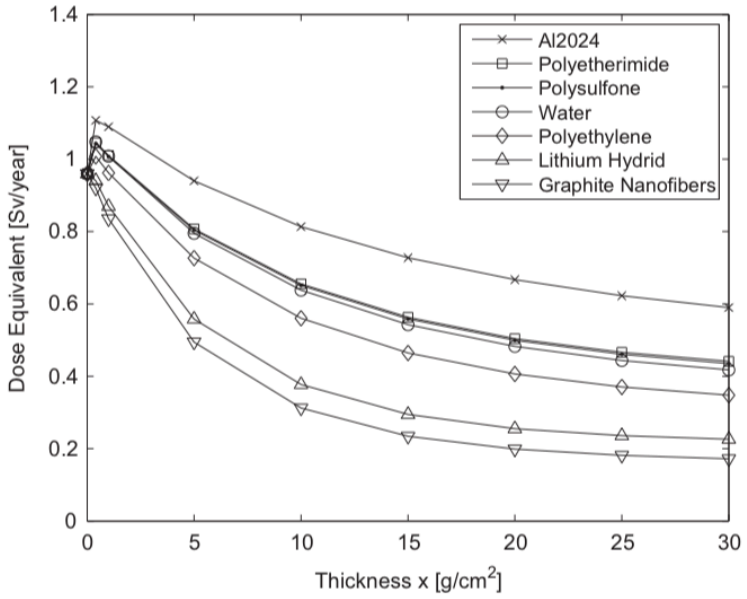

Figure 13: Yearly dose equivalent H for GCR during transfer at solar minimum in Sv/year for different materials calculated with HZETRN [93]

Polyethylene (PE) with molecular formula $(CH_2)_n$ has been widely and deeply studied for radiation shielding [95, 96]. NASA has chosen PE as the reference material against which other shielding materials are compared due to the high hydrogen content of 14 wt%. Moreover, ultrahigh molecular weight high density polyethylene (UHMW-HDPE) and high-density polyethylene (HDPE) are the main polymers applied as space radiation shielding materials. They are commonly used as reference as well to compare new developed materials by NASA and other researchers [13, 97-99]. It has 23% weight advantage compared to Al exposure to GCR due to the high hydrogen content [93]. Francis A. Cucinotta et al. pointed out that REID of PE (1.7-3.5%) shows lower probability than that of Al (2.0-4.4%) for 20 g/cm^2 shields for 40-yr males on Mars swing-by mission [99].

PMMA has been studied as shielding material for GCR as well, and positive results of protecting human tissues have been reported [100-102]. Regarding proton radiation shielding, compared to Al, PMMA is showing less proton stopping range and secondary protons generation [72, 103]. Zeitlin et al. reported one of the PMMA, poly (methyl methacrylate), radiation shielding properties in 2006 [104]. They tested the radiation shielding properties of 24 types of materials under HZE particle beam (Fe_{56}). Results of radiation testing are provided in Figure 14, in which;

$$\delta D_n = \delta D / sample\ thickness$$

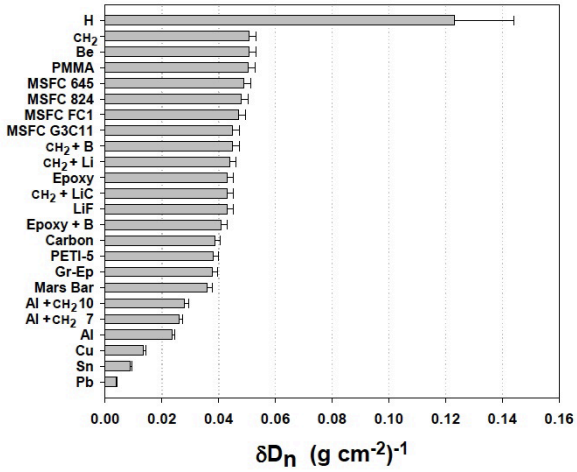

Figure 14: δD_n of materials [104]

Samples under test are different in thicknesses and different densities, thus, the δD should be normalized to areal density having δD_n. The higher the δD_n value, the better shielding effectiveness the samples have. It is firstly found that pure hydrogen is the best shielding material against HZE particle radiation; PE, and low-Z elemental materials such as Be and PMMA have the second best shielding effectiveness over other composite materials and elemental materials.

Comparing PMMA to HDPE, PMMA has stronger mechanical properties and higher working temperature. The details are listed in Table 6 [105, 106]. Since wide working temperature is a significant concern for material used on spacecraft, especially as shielding material. Consequently, PMMA possesses glass temperature above 100 °C had become our prioritized candidate for development of new radiation shielding materials rather than HDPE which has melting point of 80 °C [107].

Table 6: Basic properties of HDPE and PMMA [105, 106]

Materials	HDPE	PMMA
Tensile strength (MPa)	32	70
Z/A	0.57	0.539
Thermal conductivity (W/m-K)	0.3	0.25
Coefficient of thermal expansion (10^{-5} cm-cm/°C)	6-7	6

2.4.2 Nanocomposites

Nanofiller induced nanocomposite can be a solution to improve overall properties (such as radiation shielding effectiveness and physical properties) of polymer matrix.

(i) Radiation Resistance

Regarding to radiation shielding, the radiation-induced free-radical formation is responsible for the degradation of the material properties. Generally, upon photon/particle irradiation, the ionizing energy absorbed by the polymer backbone initiates a free radical process [108]. Subsequently, the polymer then undergoes chain scission (results in reduction of tensile strength and elongation) and crosslinking (increases tensile strength and but reduces elongation), both of which alter the material characteristics of the polymer. Regarding to the nanocomposite materials, the enhancement in the matrix material properties has been attributed to the properties of the filler material, uniform dispersion of the filler within the polymer matrix, the type of interaction between the filler and the polymer (interfacial effects), and the size effects of the filler [109, 110]. Therefore, the reinforcement of polymer with nanomaterials, which present good radiation resistance has shown to improve radiation-resistance properties of the composite materials [24, 25, 27, 28, 76, 77].

Both experimental and simulation studies reported that nanocrystalline materials showed radiation-resistance when compared to their polycrystalline counterparts. This property of nanomaterials has been attributed to the large volume-fraction of grain boundaries that may serve as effective sinks for defects produced upon irradiation of ions and proton beams [111-114]. Recently, Bai et al. proposed a "self-healing" mechanism especially near the nanograin boundaries through efficient annihilation of interstitial defects produced upon irradiation [115]. Subsequently, one may hypothesize that incorporation of nanocrystalline materials into polymeric matrix may impart their radiation-resistant behavior to the nanocomposite. However, besides carbon based crystalline materials, most of them are always formed with large amount of high-Z materials, such as metallics, which will increase weight factor of nanocomposite and largely produce secondary radiations in radiation shielding applications [116].

Carbon based materials have been investigated as radiation shielding applications. Carbon-carbon (C-C) material has also been widely considered for space applications. The C-C material is made of carbon fibers and carbonaceous matrix such as graphite. Zhong et al. reinforced the UHMW-HDPE fiber/epoxy composite using graphite nanofibers [117]. The material was tested under HZE particle radiation with energy 1 GeV/nucleon. The addition of graphite nanofibers proved to be able to enhance the mechanical and thermal properties of UHMW-HDPE fiber/epoxy composite without reducing the radiation shielding effectiveness.

Since the discovery of carbon nanotubes in 1991 by Iijima, CNT have been looked at extensively by researchers in various fields such as chemistry, physics, materials science, and electrical engineering. CNT are unique nanostructured materials with remarkable physical. These properties have inspired interest in using CNT as filler in polymer based composite systems to obtain ultra-light structural materials with enhanced radiation shielding and other characteristics.

Though several groups have investigated polymer composites with CNTs for improving the thermal and the mechanical properties of polymers [20, 118-120], only few groups have reported the ionizing radiation resistivity in CNT films and CNT-based polymer composites [28, 121-123]. Clayton et al. studied the material properties of poly(4-methyl-1-pentene) (PMP) reinforced with 0.5 wt% loading of single-walled CNT [20]. They illustrated its high radiation and mechanical performance that can replace PE as shielding materials against GCR. Peter J. Boul et al. simulated LEO environment by using proton beams with energies of 10 and 30 MeV to detect deformations of single-walled carbon nanotubes (SWCNT). Slight I_D/I_G ratio increase of proton irradiated samples shows proton beam induced disorder in SWCNT film [121].

Moreover, our group, previously, reported the stopping properties of SWCNTs-based polymer composite under high-energy proton beam [27]. The energy levels of the incident proton beam were set to 63 and 105 MeV with beam density of 5 nA (2×10^8 protons cm^{-2} s^{-1}). The beam spot-size at the position, where the samples were tested, was 19 mm in diameter. The dose rate characteristics (BIC/DIC vs. RS values) of the samples are shown in Figure 15. The $RS_{90\%}$ (range shifter) values and Water equivalent thickness (WET) of the samples (listed in Table 7) were calculated. Subsequently, the stopping range and the weight of each of the materials corresponding to the same proton energy were compared. The calculated SR_{AD} of materials are plotted in Figure 16a. In comparison with Al, both PDMS and PDMS/SWCNT have a weight advantage. As shown in Figure 16b, it is found that both of the pure polymer, Polydimethylsiloxane (PDMS), and the PDMS/SWCNT composite has weight advantage over Al, which are up to 18.3% and 20.84% lighter than Al respectively when proton energy is 105 MeV. Moreover, the performance of pure PDMS decrease along the increase of proton energy due to extra secondary radiations produced at higher proton energies. And by adding SWCNT, the nanocomposite performs better by the increase of proton energy. This is caused by secondary radiation absorption ability of SWCNT in the nanocomposite.

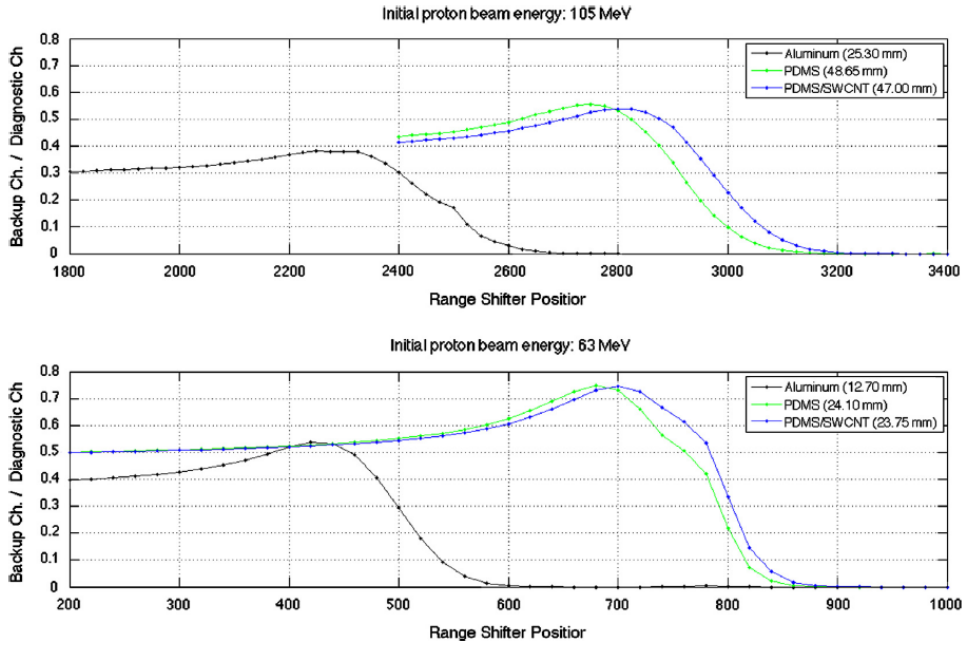

Figure 15: Dose rate characteristics of Al, PDMS and PDMS/SWCNT under initial proton beams of 105 and 63 MeV. The thickness of each sample is indicated in the legend [27]

Table 7: Material specifications, WETs and their corresponding ion energy [27]

Initial Proton Energy (MeV)	**Material**	**Density (g/cm^3)**	**Thickness (mm)**	***RS*$_{90\%}$**	**Experimental WET (mm)**
105	Al	2.698	25.30	2368	52.77
105	PDMS	1.033	48.65	2844	47.22
105	PDMS/SWCNT	1.038	47.00	2889	46.70
63	Al	2.698	12.70	462	25.26
63	PDMS	1.033	24.10	717	22.30
63	PDMS/SWCNT	1.038	23.75	738	22.05

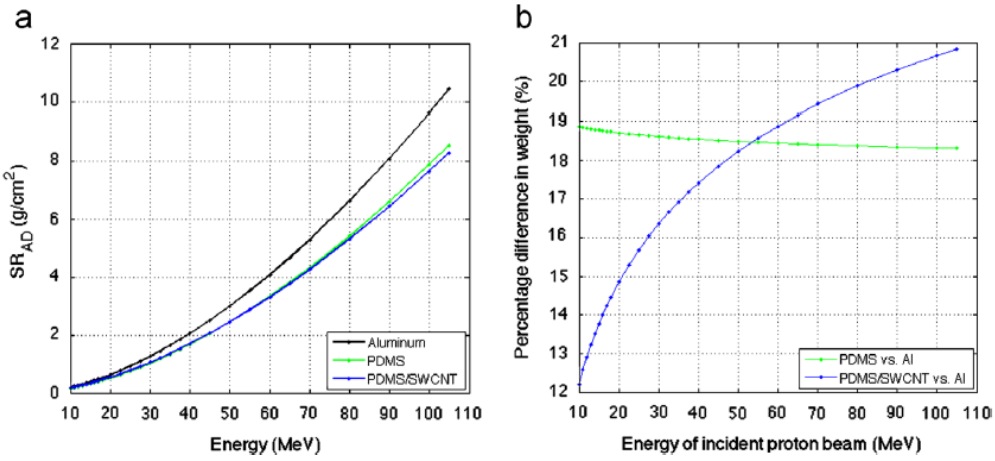

Figure 16: SR$_{AD}$ of Al, PDMS and PDMS/SWCNT and Percentage in weight of PDMS and PDMS/SWCNT with respect to Al [27]

Experimental results and calculations show that a relatively low loading (1.12 wt%) of SWCNTs improve the proton shielding ability of PDMS matrix. An indirect method, based on Bragg-Kleeman (B–K) rule, for measuring the proton stopping range in solid materials has been proposed. The weight reduction effects contributed by the SWCNTs become evident at higher proton energies (higher than 53.59 MeV); the weight advantage increases with increasing energy. The stopping range of the nanocomposite is affected by the structure and distribution of the filler material. The non-uniform dispersion of non-functionalized SWCNTs might have affected the overall weight reduction and material-reinforcement properties of the nanocomposite. The effects of uniformly distributed SWCNTs over the stopping range and material properties of the nanocomposite are suggested for further studies.

S. Mathew et al. investigated deformation difference between SWCNT and MWCNT, and they found less I_D/I_G ratio (less disorder) in Raman spectrum in MWCNT after 2 MeV irradiation [29]. Besides that, other studies demonstrated SWCNT could suffer more from charged particle radiations than MWCNT [30, 31]. The inter-layer covalent bonding found in MWCNT after ionizing radiation can cause bridging inter-layer graphene layers, which results in increase of thermal conductivity as number of graphene increases [124-127]. As a result, MWCNT is an excellent candidate for ionizing radiation applications.

Regarding electron radiation shielding, one group has shown the etched depth of different PMMA-CNT films that were exposed under UV and 20 keV electron beam for 15 min (Figure 17) [28]. Addition of CNT is showing less etch depth if nanocomposite with a threshold of 0.5wt% CNT.

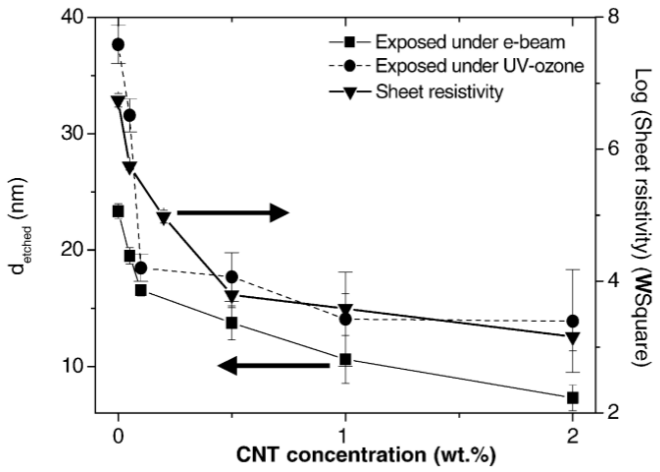

Figure 17: Etched depth vs. CNT concentration under e-beam and ultraviolet ozone [28].

As introduced in section 2.1.4, secondary radiations (electrons, light ions, gamma rays and neutrons) generated by interaction between GCR and shielding materials are harmful to payloads. During shielding and absorbing neutrons by hydrogen rich polymers, extra hazardous gamma rays will be delivered. Herein, nanofiller possess high stopping power and bandgap is desired to stop electrons and absorb gamma rays. However, stopping power of carbon (1.79 MeV cm^2/g at 10 MeV electron) shows limited capability in shielding high energy electrons compared to conventional electron/photon shielding material lead (Pb) (2.41) [76]. Due to toxic concerns of Pb, various lead-free materials have been developed for radiation shielding applications. By adding nanofillers with similar shielding properties as high Z material Pb into polymers is an efficient way to increase stopping power but still keep light in overall weight [128]. For instance, Gadolinium oxide (Gd_2O_3) has been used to absorb photons within polymer matrix in some studies [128, 129]. However, the high cost to its nanopowders limited its applications [130, 131].

Bismuth oxide (Bi_2O_3) with bandgap of 2.3-3.3 eV has been investigated as an effective radiation shielding material [32-34]. Compared to lead and most of its compounds, bismuth oxide is provided with higher bandgap, non-toxic property, and higher total stopping power (Bi: 2.433 and Pb: 2.407 MeV cm^2/g at electron energy of 10 MeV) (Figure 18) [132-136]. Therefore, addition of Bi_2O_3 in PMMA polymer matrix will potentially improve the attenuation of electron radiations.

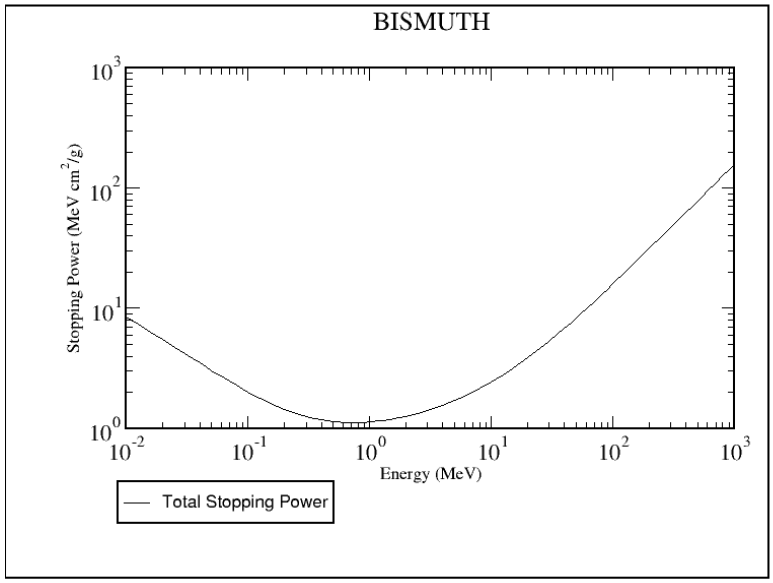

Figure 18: Stopping power for electrons (Bismuth) [132]

(ii) Mechanical Properties

The mechanical properties of CNT suggest that they may be used as reinforcing fibers in high-toughness nanocomposites, where stiffness, strength and low weight are important considerations. The strength of composites depends on two variables. First, there should be a high degree of load transfer between the matrix and the nanotubes. When the interfacial adhesion between the phases is weak, the nanotubes behave as holes or nanostructured flaws, inducing local stress concentrations, and the benefits of the CNT properties are lost. Second, the nanotubes should be well dispersed. If they are poorly dispersed, the nanotubes will fail by separation of the bundle rather than by failure of the nanotube itself, resulting in significantly reduced strength.

Carbon-based filler materials such as carbon nanofibers and nanotubes are used as mechanical reinforcement in a variety of polymers (resins and plastics) exhibiting high strength-to-weight ratio. Some studies discussed about mechanical strength enhancement by embedding CNT into polymer matrix [137-139]. For example, the nanocomposites of a high-performance polymer-polybenzimidazole and carbon nanofibers or other nanomaterials have been studied for durable space applications [140, 141]. Other than the carbon nanofibers, the carbon nanotubes (CNT) can improve the material properties of polymer nanocomposites at relatively low loading of CNTs due to its properties of exceptionally high elastic-modulus and tensile strength (about 1 TPa and tens or hundreds of GPa respectively) along with excellent thermal and electrical conductivity, and very high resistance to oxidation in air (700 °C) [20, 110, 142]. Thus the carbon nanocomposites can be suitable candidates in applications requiring mechanically strong, ultra-lightweight materials [143]. Moreover, studies have also shown that the composite materials using other nanofillers exhibit enhanced mechanical strength and higher thermal stability in addition to the radiation resistance compared to the polymer without filler [140, 144, 145]. Some researches for nanocomposites are illustrated below.

There are numerous possible applications; some examples are aerospace structural panels, sporting goods, ultra-lightweight thin-walled space structures for use in space, and high stiffness-to-weight space mirror substrates. A new application for these types of nanocomposites is automobile bumpers. The bumper made of CNT nanocomposites will have good mechanical properties and lower weight than the standard fiberglass bumpers, since only 1-5 wt% CNT will be needed compared to 30 wt% or more of fiberglass.

(iii) Thermal Properties

As discussed in the previous section, the properties of reinforced polymers greatly depend on the filler material. Since most of the polymers have very low thermal conductivity, most of the research is focused on using fillers with high thermal conductivity. In this regard, the carbon-based nanomaterials, including CNT and graphene, will reinforce not only the radiation resistivity and radiation shielding performance but also the thermal conductivity. This is because of the extremely high thermal conductivity of the nanotubes and graphene.

The reported thermal conductivity of individual MWCNT (with outer diameter of 14 nm and length of 2.5 μm) is higher than 3,000 W/m-K [146], and SWCNTs can reach about 6,000 W/m-K theoretically [147]. The theoretical thermal conductivity of SWCNT is more than the twice as the reported value of MWCNT (>6000 W/m-K). On the other hand, the thermal conductivity of graphene is similar to CNT, which can reach the range of 3,000-5,000 W/m K under the room temperature, which is determined by the spectral position and integration intensity of graphene's G mode [148]. In comparison, the thermal conductivity of Al is only about 240 W/m-K, which is less than one tens of the value of pure CNT and graphene.

The polymers including epoxy resin and elastomers usually have thermal conductivity of less than 1 W/m-K. By adding CNTs, graphite or both at the same time, the thermal conductivity of polymers can be increased by up to thirty times [149]. MWCNTs with volume percentage of 0.4% in thermal conductive elastomer have thermal conductivity of 1.21 W/m-K, which is 105% more than that of the matrix (two parts silicone elastomer Sylgard 160 (s160), 0.59W/m-K) [150]. By adding SWCNTs to low density polyethylene (LDPE) and high density polyethylene (HDPE) with weight percentage of 2 wt.%, respectively, the thermal conductivity of the LDPE was increased by 592% and the HDPE was increased by 600% [151]. However, the enhancement of thermal conductivity is nonlinear with increasing CNT fraction. Figure 19 shows the thermal conductivity enhancement of polymer matrix with different volume fraction CNT.

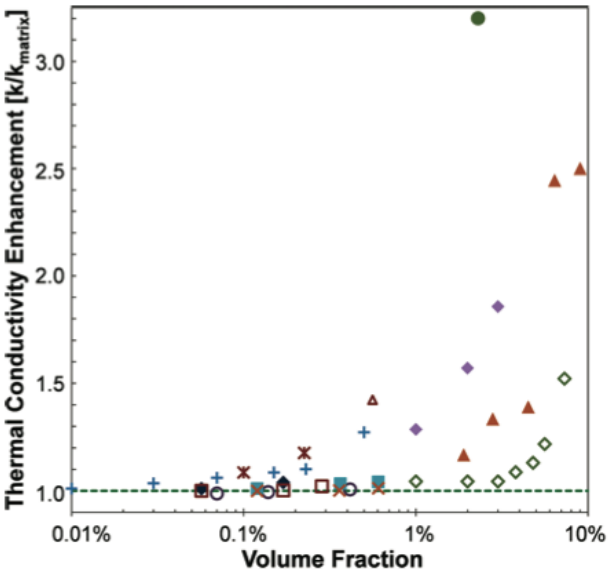

	Matrix	CNT Details	Reference
+	Epoxy (Epon 828)	HiPCO SWCNT	Bryning *et al.*[6]
×	Epoxy (Epon 828)	Laser Oven Grown SWCNT	Bryning *et al.*[6]
●	Epoxy (Epon 862)	HiPCO SWCNT	Du *et al.*[23]
○	Epoxy (Bakelite L13i)	SWCNT	Gojny *et al.*[5]
■	Epoxy (Bakelite L13i)	DWCNT	Gojny *et al.*[5]
×	Epoxy (Bakelite L13i)	DWCNT-NH_2	Gojny *et al.*[5]
◆	Epoxy (Bakelite L13i)	MWCNT	Gojny *et al.*[5]
□	Epoxy (Bakelite L13i)	MWCNT-NH_2	Gojny *et al.*[5]
◆	Silicone	MWCNT	Hu *et al.*[8]
◇	Polymethylmethacrylate	SWCNT	Bonnet *et al.*[9]
▲	Polymethylmethacrylate	SWCNT	Guthy *et al.*[10]
△	Polyethylene	SWCNT	Haggenmueller *et al.*[24]

Figure 19: Thermal conductivity enhancement vs. CNTs volume fraction [120].

The thermal conductivity reinforcement effect of CNT is strongly affected by the aspect ratio, distribution and the way of interacting with polymer matrix of CNT. Due to the existence of interface thermal resistance, it is suggested by Shenogin et al. that CNT-polymer composite with optimal covalent bond density can minimize the interface resistance; and second, optimal geometric parameter selection of CNT to present high aspect ratio will enhance the thermal conduction within the composite materials [152]. Even at low loadings of CNT in polymer, the percolation threshold can be achieved in the nanocomposite, which means that the CNT in polymer matrix come in contact with each other to form a network. Zhong et al. have reported the reduction of contact resistance with longer CNT and larger overlap of CNT such that well dispersed CNT in polymer shows better thermal conducting performance [153]. Aligned CNT in composite will allow anisotropic thermal performance with extremely high thermal conductivity in a given direction which indicates that heat can efficiently transfer through nanotube axis [154]. Moreover, higher CNT concentration in the composite materials without affecting the overall mechanical properties will present higher thermal conductivity. Figure 20 shows the thermal conductivity of composites with uniform and poor dispersion of CNT. Another important aspect to improve the thermal conductivity is the crystallinity of molecules because polymer needs strong bonds to transfer phonons. Liao et al. reported the influence of crystallinity on the dispersion of MWCNT in polypropylene (PP) matrix; however, MWCNTs can obtain better dispersion in low crystallinity PP rather than higher [155].

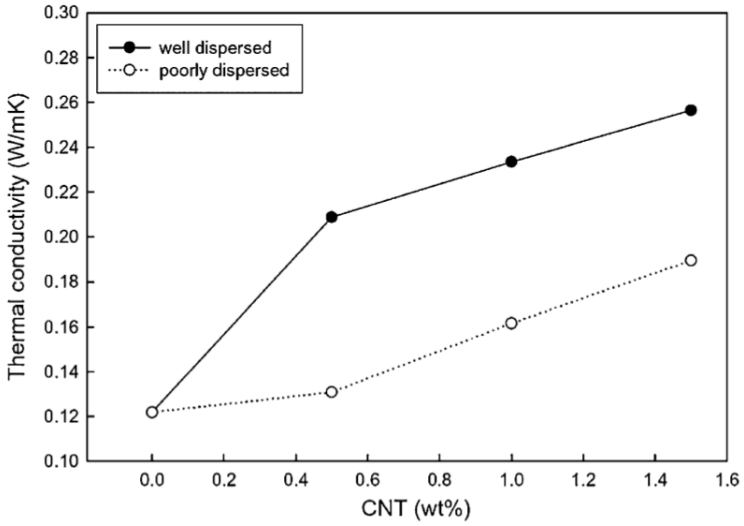

Figure 20: Thermal conductivity of nanocomposites depends on CNT loading [156].

2.4.3 Multifunctional Structure for Space Radiation Shielding

However, pure polymers are weak in mechanical strength and low in thermal conductivity when compared to the metal counterpart Al. Compared to metals with metallic bonds between their atoms, polymers containing mostly the covalent bonds are not strong enough [157, 158]. As discussed in some studies, multilayered structure is recommended as a new approach to innovative space radiation shielding [23]. Kaul et al. designed a three-layer PE based composite, RXF1, for space radiation shielding purposes due to the lightweight and higher shielding effectiveness compared to Al [21]. The first layer is a ceramic material, which contains Al_2O_3, B_4C and SiC. This layer is used for protecting spacecraft or interstellar bases from meteoroid collisions. The second layer is made of a PE matrix incorporated with ultra-high molecular weight PE fibers. This layer provides protection against both meteoroid collision and space radiation. The third layer is epoxy resin reinforced with interwoven PE fibers. The third layer is the major layer for radiation protection. These three layers are compressed together forming a multifunctional-layered composite. Thus, extra layer providing outstanding mechanical and thermal properties in multifunctional structure is discussed in this section.

Carbon fiber reinforced polymer, carbon fiber reinforced plastic or carbon fiber reinforced thermoplastic (CFRP, CRP, CFRTP or often simply carbon fiber, or even carbon), is an extremely strong and light fiber-reinforced polymer which contains carbon fibers. However, various new fibers and resins have been developed to produce improved CFRP, such as the one containing M55J

(6K) carbon fibers and RS-3 epoxy-based resin. It has been used in space due to the high stiffness-to-weight ratio.

CFRP is used extensively in aerospace and space applications. The Airbus A350 XWB is built of 53% CFRP including wing and fuselage components, the Boeing 787 Dreamliner, 50%. Specialist aircraft designer and manufacturer Scaled Composites have made extensive use of CFRP throughout their design range including the first private spacecraft Spaceship One. CFRP is widely used in micro air vehicles (MAVs) because of its high strength to weight ratio. Ultralight aircraft such as the E-Go, rely heavily on CFRP in order to meet the category weight compliance requirement of less than 115 kg (254 lb) without pilot or fuel [159]. Moreover, this type of resin-based carbon fiber reinforced composite material has been used as electronic enclosure materials [160-162], solar sails [163], outer panels of satellites [164], and has even been used for the sandwich structural components and struts on Equator-S spacecraft [39]. Some examples of applications of CFRP materials in space missions are listed.

CFRP K1100-M40J/RS-3 for SAR antenna enclosure: The enclosure requires high thermal conductivity to transport dissipated power and enough electrical conductivity for electromagnetic radiation shielding and circuit grounding. The dimensions of the enclosure are about $84.2\text{mm} \times 119.6\text{mm} \times 340.4\text{mm}$, in a rectangular box shape with surface area of 158,887.7 mm^2. The chosen CFRP material for this application, K1100/M40J fibers laminated with RS-3 resin, can provide thermal conductivity of 1.675 W/m-K. The density of such a material is about 1.698 g/cm^3 [160].

CFRP M55J/RS-3 for extreme ultraviolet imaging spectrometer (EIS) housing: The structure of EIS requires high stiffness and dimensional stability in order to maintain the resolution of optical components. Weight constraints from the launching vehicle (M-V launcher) also require the structural materials to have a high strength to weight ratio. CFRP, which made of M55J fiber laminated with RS-3 resin, provides longitudinal tensile modulus of 298 GPa, which is almost three times the tensile modulus of titanium alloys. The size of this particular enclosure is 3.2 meters in length [162].

CFRP developed for Light-weight Exploration Rover (ROV-E): ESA has supported the development of lightweight technology for exploration rovers through FP7, where the Mass is a major issue for interplanetary missions. One of the objectives is to improve the existing and investigate the new technologies for the multifunctional structures. The ROV-E integrates not only

structural and thermal functions in the component but also electrical, health monitoring, EMI-EMC shielding, power, storage and mobility functions for rover driving and steering.

CFRP for sandwich structure components and struts on Equator-S spacecraft: The experimental platforms of the Equator-S spacecraft were made of polymethacrylimide (PMI) foam reinforced with two layers of CFRP on both sides. The thickness of PMI foam is 24 mm and the thickness of CFRP is 1.4 mm. The struts were 20 mm in diameter, which were fully made of CFRP material [39].

However, there are two major factors that limit the applications of CFRP materials in space missions. Firstly, CFRP materials suffer from degradation due to the exposure to radiation sources (electrons, UV, X-rays) and extreme space environment (vacuum, thermal cycle). Secondly, CFRP materials cannot provide enough particle radiation protection for the devices enclosed. Therefore, outer layers of materials coated on the CFRP components are an ultimate option for providing protection to both the payloads and the CFRP materials themselves [39].

As reviewed in section 2, proton and electron radiations have been considered as major harmful radiation sources in this study. Based on the radiation shielding theories, low-Z (such as hydrogen) and high-Z (such as lead) materials are efficient to stop proton and electron radiations respectively. Many materials including aluminum and polymer composites have been widely investigated for space radiation shielding applications. Currently, numerous hydrogen rich materials with excellent radiation shielding effectiveness compared to Al are consistently reported from research labs and industries. However, critical challenges associated with the research fields remains in the development of a multifunctional radiation shielding structure to replace Al in space applications. By reviewing previous researches, polymer PMMA and nanomaterials (MWCNT and Bi_2O_3) with outstanding radiation shielding effectiveness and physical properties were studied for space radiation shielding applications. Incorporated with CFRP, by providing the same radiation shielding effectiveness compared to Al, polymer-based nanocomposites with enhanced physical properties by nanofillers are expected to be light-weight than metallic shielding materials. In addition, other apparent advantages of using those materials such as low-cost and high adoptability are also implanted in the research. In this thesis, methods of fabrications and evaluations of polymer nanocomposite involving multifunctional CFRP structure are well displayed.

Chapter 3 Fabrication Process and Characterization

This section is intended to illustrate background of main apparatus used for material fabrication and characterization. Adequately understanding of these tools can be helpful to interpretation of methods used and results discussed in the subsequent sections.

3.1 Fabrication Methods

Three common methods for bulk fabrication of polymers and composites are: (i) Melt mixing processing which involves application of heat above the melting point followed by sufficient agitation; (ii) Solution processing using solvent to reduce the viscosity of the polymer followed by casting it into mold (of desired dimensions) in a vacuum oven to evaporate the solvent; (iii) Polymerization process from monomers. However, for bulk fabrication, solution processing method would evaporate tons of toxic chemical into atmosphere, causing environmental concerns [165, 166].

In situ bulk polymerization of PMMA and its composites had been widely studied. Definitely, it is a good method to conduct interactions between functional groups and polymer matrix [167]. Dispersion quality of MWCNT in polymer matrix has been analyzed. Usually, long time ultra-sonication and other strong mechanical interruption are required to break agglomerations between MWCNT to improve uniformity of nanocomposites [168]. However, deformations and precipitation of CNT at high concentration of fillers were observed. Besides, unstable molecular weight in each reaction was found in polymerization process, thus the process for bulk fabrication is not suitable.

Melt mixing process is an efficient method to fabricate nanocomposite. In melt mixing process, MWCNT are mechanically dispersed into a melted polymer matrix using a mixer. The idea is to break MWCNT aggregations and prevent reformation by fluid shear forces [169]. This simple process is compatible with other techniques such as injection and compression molding. Besides that, less deformation and sufficient interaction between MWCNT and polymer chains can be found. Therefore, it is ideal for both research and scale-up industrial fabrication.

Eventually, melt mixing process was used in this research. Commercial PMMA powders were purchased (182230 ALDRICH) and applied for further fabrication and tests (Table 8). Carboxyl functionalized (-COOH) MWCNT (diameter = 10–20 nm, length = 10–30 μm, ~1.9–2.1 wt% of -COOH content) were purchased from Nanostructured & Amorphous Materials (USA) (Table 9). Related material information of abovementioned MWCNT (MWCNT is short for MWCNT-COOH

in subsequent chapters) are listed in Table 9. Regarding electron shielding materials, bismuth oxide nanopowders in diameters of 90-210 nm were ordered from Sigma-Aldrich (637017 ALDRICH).

Table 8: Properties of purchased PMMA [170]

Density at 25 °C (g/cm^3)	1.188
Formula	$(C_5H_8O_2)_n$
Flash point (°C)	> 250.00
Molecule weight	average Mw ~120,000 by GPC
Transition temp (°C)	*Tg* (DSC) 105 (midpoint)

Table 9: Properties of MWCNT-COOH [171]

Average Diameter (nm)	10-20
Average Length (µm)	10-30
Apparent Density (g/cm^3)	at 20 ° C, ~ 2.1 g/cm³
Carbon Purity (wt%)	> 95
Content of -COOH	1.9-2.1 wt%

3.1.1 Torque Rheometer

As shown in Figure 21, a melt mixer, Haake Rheocord 90, from Thermal Scientific was used to fabricate samples. The mixer is able to operate at a programmed speed versus time to record response (torque) of mixing materials. Different materials can be mixed with additives of various types and concentrations. By measuring melting behaviour, consumed energy or melt viscosity, material or composite quality can be analyzed [172-174].

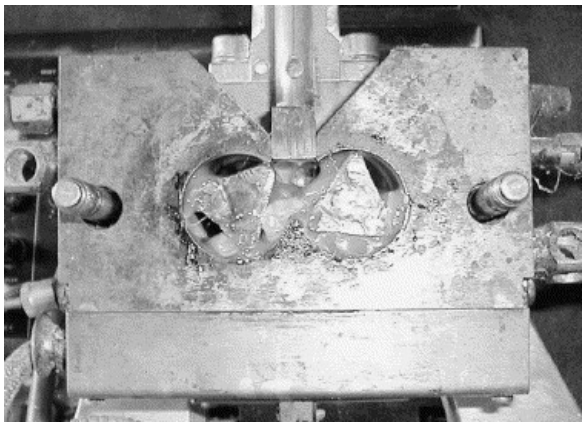

Figure 21: Cross section of a melt mixer [172]

3.1.2 Twin Screw Extruder

Figure 22 illustrates a basic structure of single screw extruder. Polymer beads are firstly gravity-fed into the barrel through a hopper. The rotating screw pushes the fed material towards the end of barrel through friction force. The whole process can be separated into three sub processes: 1) solids conveying: once the powders are fed into the barrel, they gradually heat up to the melting point starting melting process; 2) melting: all of the fed materials melt in this region; and 3) melt-pumping: the melt material will be pumped to the end of the barrel and be compressed into the mold [175].

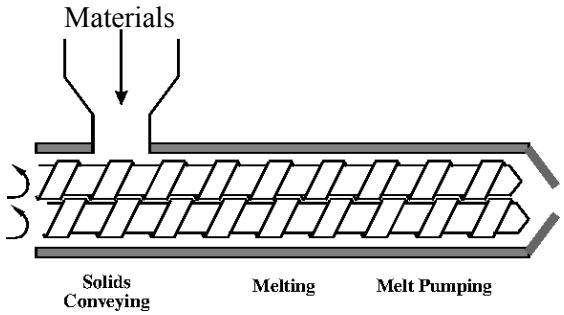

Figure 22: Schematic diagram of a typical twin-screw extruder [176]

Twin-screw extruder, Coperion ZSK 25mm is energy efficient with wide range of applications. It is a reliable instrument for materials research and scale-up fabrication [177] [178]. The basic parameters of the extruder are listed in Table 10. The ratio between outer and inner diameter (D_o/D_i) of screws is 1.55 which has been proven to be optimal for applications that require a high torque [179]. Due to the high viscosity of PMMA, proper specifications, such as feeding rate, screws speed, temperature of each zone and torque should be well designed. Amine et al. used feeding rate of 3 kg/h with 120 rpm screw speed to achieve well dispersed PMMA/CNT nanocomposite [180]. They found that increasing the feeding rate can reduce the mixing performance, while increasing the screw speed can enhance the dispersion [180]. Moreover, Zhang et al. reported a feeding rate of 3.6 kg/h, screw speed of 120 rpm to mix PMMA matrix and CNT as well as the mixing temperatures, which ranged from 180 °C to 235 °C, in different zones. Table 11 illustrates parameters used in our research.

Table 10: Basic Specifications of Coperion ZSK 25mm

Specific torque	15 Nm/cm^3
Diameter of screws	25 mm
Maximum screw speed	1,200 min^{-1}
D_o/D_i	1.55

Table 11: Recipe of Nanocomposite on Extruder

Torque (Nm/cm^3)		11.25-12.75
Screw speed		103 rpm
Feeding rate		3 kg/h
Zone temperatures (°C)	Zone 1	170
	Zone 2	200
	Zone 3	200
	Zone 4	200
	Zone 5	195

3.1.3 Planetary Mixer

Planetary mixer has been used to melt and mix PMMA and MWCNT nanocomposite. The viscosity of PMMA can range from 1,000 to 1 million cP at different temperatures. The suitable mixer for viscous materials, such as PMMA, must therefore utilize agitators that move through the batch regardless of product the flow. This is exactly the advantage of the double planetary mixer. Powerful, variable-speed drives and heavy construction enable this mixer to deliver high torque throughout its entire speed range. Due to involvement of MWCNT, which is fragile under high-shear mixing or ultra-sonication, the gentle mixing condition is ideal for producing nanocomposite. Double planetary mixers are robust machines capable of handling materials have high viscosity (about several million cP). The gentle and thorough folding action imparted by the orbiting blades carefully mixes ingredients into a viscous batch that would otherwise break apart from excessive shear. Double planetary mixer (DPM) moves material by rotating two identical blades on their own axes as they orbit on a common axis (Figure 23). The blades continuously advance along the sidewalls of the mix tank, removing material from the walls and transporting it towards the interior [181-183].

Figure 23: Side view of DPM tank and agitators

3.1.4 Vacuum hot press

Hot press has been widely used in some studies (Figure 24) [184-186]. With controlled temperature and compression pressure, customized progress can be designed for different applications. It is an ideal method to mold hot melt materials, such as thermoplastic polymers and composites, into flat pieces. Materials in powder or grinded small pieces are placed between top/bottom mold plates. When the loaded materials have been heated up to melting temperature, plates are closed followed by incident pressure until materials are molded into the desired thickness.

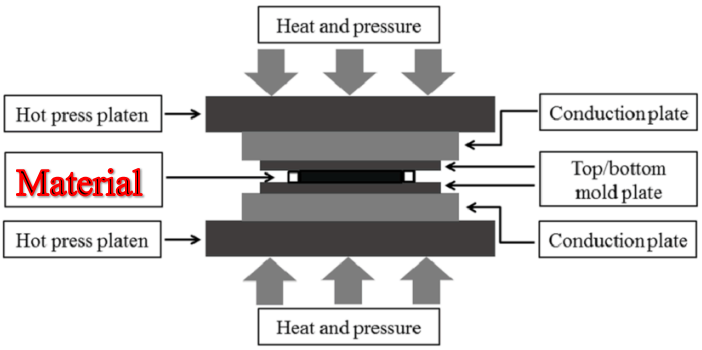

Figure 24: Schematic representation of the hot press machine [186]

3.1.5 Benchtop Injection Machine

Injection machine is commonly used in material processing [187, 188]. This process involves hot melt polymers in heating channel and injecting them through a nozzle into a designed mold which followed by cooling and demolding. Controlling the flow rate of polymer injection is critical because low flow rate can result in a partially filled mold. Based on the equation below, where v is the velocity in ms^{-1}, A is the cross section of the heating channel in m^2 and Q is the volume flow rate in m^3s^{-1}, higher flow rate (Q) can result in increased velocity of polymer (v). The temperature can be set above the melting temperature of materials to achieve acceptable viscosity so that materials can be injected into the designed metallic mold. This machine (model WZ20000) in Figure 25 was manufactured by Dongguan Kunlun Testing Instrument Co., Ltd.

$$v = \frac{Q}{A}$$

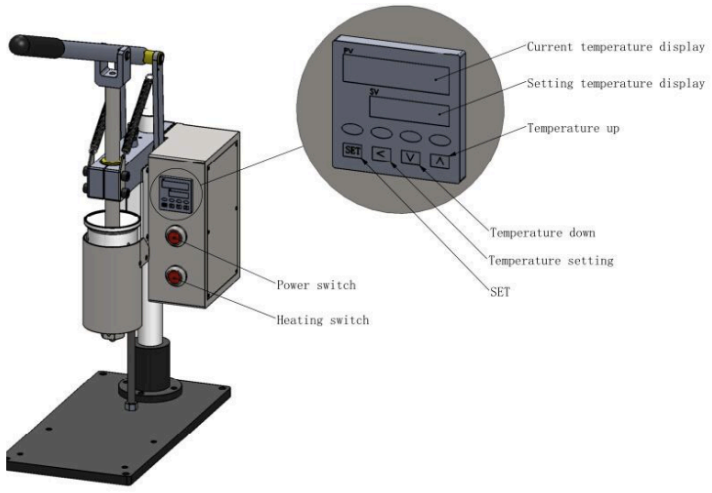

Figure 25: Injection machine

3.2 Material Characterization

3.2.1 Raman Spectroscopy

Raman spectroscopy is a commonly used technique to provide a fingerprint of the molecular structure. A visible laser light provides energy to vibrate molecular in materials so that the energy of the laser photons being shifted up or down, and then the shifted intensity of the laser will offer information of measured materials (Figure 26) [189].

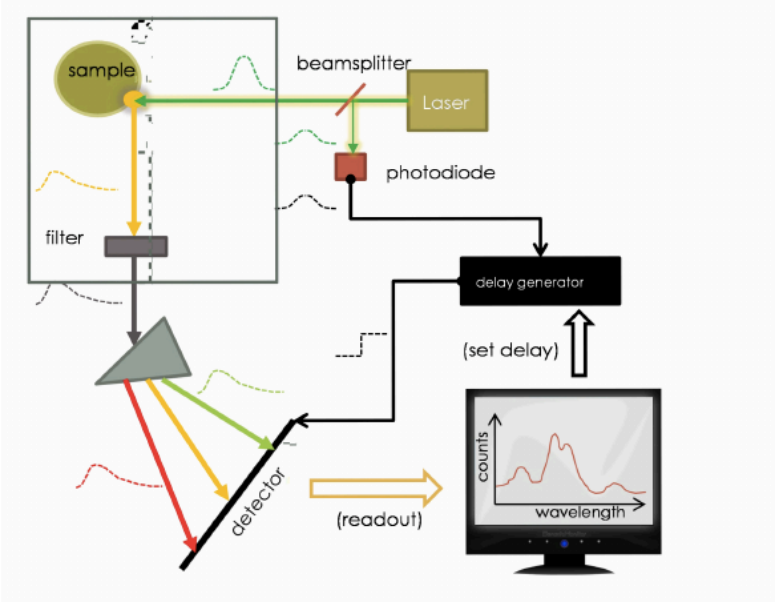

Figure 26: Schematic diagram of Raman spectroscopy [190]

The recorded Raman shifts are typically presented in wavenumbers, which have units of inverse length, which is directly related to energy, and the following equation is used:

$$\Delta\omega = (\frac{1}{\lambda_0} - \frac{1}{\lambda_1});$$

where $\Delta\omega$ is the Raman shift expressed in wavenumber, λ_0 is the excitation wavelength, and λ_1 is the Raman spectrum wavelength. Characterization of carbon materials using Raman spectroscopy has been studied for years to identify their properties in composites [191, 192].

3.2.2 Fourier Transform Infrared Spectroscopy

Similar to Raman technique, but Fourier Transform Infrared (FTIR) spectroscopy provides complementary information (Figure 27). When IR radiation is passed through a sample, some radiation is absorbed by the sample and some is transmitted. The resulting signal at the detector is a spectrum representing a molecular 'fingerprint' of the sample. The usefulness of infrared spectroscopy arises because different chemical molecules produce different spectral fingerprints. It is commonly used to identify functional groups, such as carboxylic (-COOH), on inorganic materials [193].

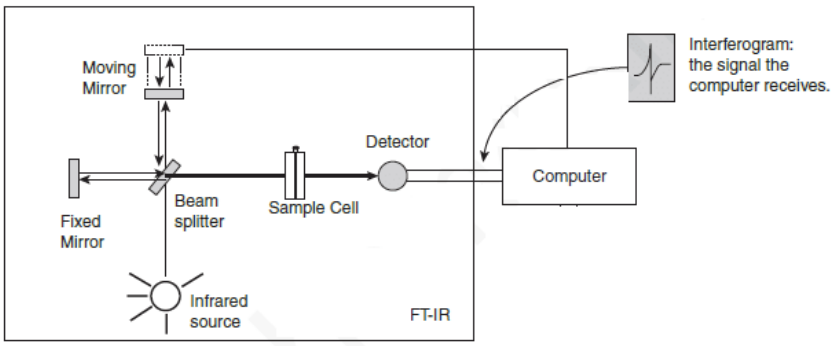

Figure 27: Scheme of FTIR [194]

3.2.3 Differential Scanning Calorimetry

Differential Scanning Calorimetry (DSC) measures the amount of heat transfers through both measuring and reference samples. The result of a DSC experiment is a curve of heat flux versus temperature. With DSC technique, it is possible to observe fusion and crystallization events as well as glass transition temperatures (*Tg*) of polymers (Figure 28) [195-197].

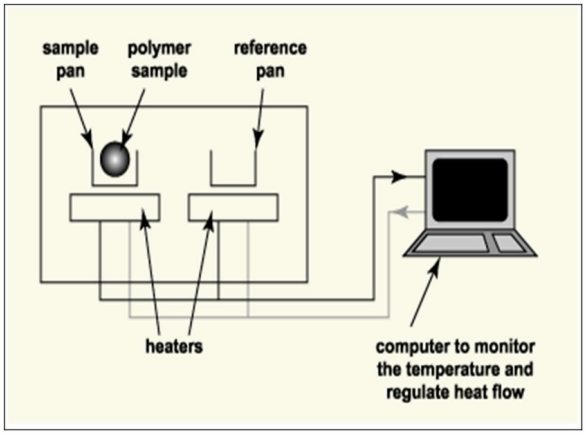

Figure 28: Scheme of DSC [198]

3.2.4 Thermal Cycle Chamber

Environmental chamber ZPHS-16-6-6-SC/AC (Cincinnati Sub-Zero Products Inc.) is used to test and store products by subjecting them to various temperature and humidity conditions. This chamber allows us to program and run basic temperature cycling or fast temperature cycling with working temperature range of -70 °C to 190 °C [199].

Some other studies have investigated thermal cycling process for space applications [200-202]. Thermal cycling test with temperature range of -100 to 100 °C was critically designed for radiation shielding materials. However, the machine can only reach -70 °C at low temperature. Thus, the upper bond of testing temperature shifted higher to 150 °C.

Besides that, to achieve an expanded limit of thermal cycling, liquid nitrogen was used to simulate temperature of -170 °C, and 130 °C is set as upper bond of testing temperature. The temperature of thermal cycling switches between -170 °C and 130 °C with temperature held stable at peaks for 30 minutes. Ten thermal cycles were applied to the materials in order to simulate the space environment. However, the rate of temperature change (10 °C/min) between -170 °C and 130 °C cannot be precisely controlled in our laboratories. Testing samples were left in room temperature for 30 minutes before entering next peak (-170 °C or 130 °C). Therefore, all tested samples were under thermal shock when switching between hot and cold temperatures. Liquid nitrogen container with a thermocouple and the oven applied temperature of 130 °C are shown in Figure 29.

Figure 29: Testing sample in liquid nitrogen (left) and oven (right)

3.2.5 Thermogravimetric Analysis

Thermogravimetric Analysis (TGA) apparatus can be used to identify components and thermal stability of materials with designed temperature [197]. TGA analysis measures the amount of weight change of a material, in powder or small pieces, as a function of increasing temperature with Weight change sensitivity of 0.01 mg (Figure 30).

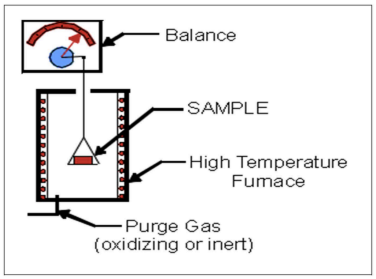

Figure 30: Scheme of TGA [198]

3.2.6 Thermal Conductivity Test

The apparatus for thermal conductivity measurement was assembled by Microelectronics Heat Transfer Laboratory at the University of Waterloo following ASTM D5470-95 standard, which is a guideline applied to test thin electrical insulation materials (Figure 31). The dimension of samples needs to be 2.5 cm by 2.5 cm with proper thickness, such as 0.5 mm for polymers and composites due to their low thermal conductivity in general. At least 3 pieces with the same dimensions were required from each material. Thus, 3 values of thermal resistance, which is linear, based on the 3 different thicknesses, can be obtained. Then, the thermal conductivity is calculated according to the slope of thermal resistance vs. thickness [203, 204].

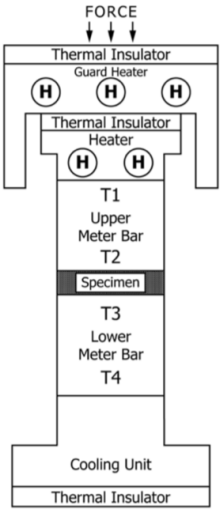

Figure 31: Scheme of thermal conductivity test apparatus [205]

3.2.7 Tensile Strength Test

The tensile strength test was tested with Instron 5548 Micro Tester in CAMJ lab (Figure 32). Following the ASTM D638-14 standard, testing materials are required to be cut in dog bone shape (Figure 32). Tensile strength of each specimen can be recorded while the centre of the dog bone is broken [206-208].

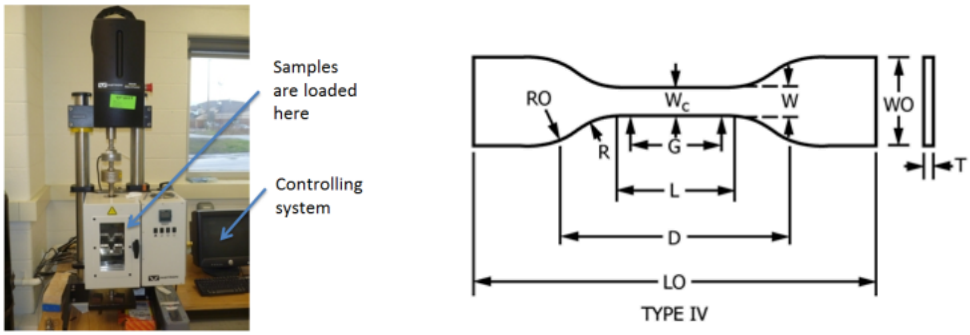

Figure 32: Instron 5548 Micro Tester (left) and dog bone shaped sample (right) [208]

3.2.8 Bonding Test Process

PosiTest Pull-Off Adhesion Tester was used for adhesive strength test on bonding (shown in Figure 33). Following the standard ASTM D4541 standard, the pull-off tester evaluates the breaking pull-off strength of coating on a substrate at breaking point. By determining the maximum pull-off force, the strength can be obtained [209, 210].

Figure 33: PosiTest Pull-Off Adhesion Tester [211]

3.2.9 Outgassing Test

Outgassing occurs when a material is placed in a vacuum environment, subjected to heat, and some of its constituents are volatilized or emitted. It is necessary to do the outgassing test in a very clean environment for space applications [212, 213]. During outgassing test, the total mass loss (TML) and collected volatile condensable material (CVCM) of materials are determined when they are exposed to a heated high vacuum environment (5 x 10^{-6} Torr). In addition, the amount of water vapor regained (WVR) can also be obtained after completion of exposures and measurements of TML and CVCM. According to ASTM E595 standard, which was developed by NASA to screen low outgassing in adhesives and other materials for space applications, the material can pass the test only if it satisfies the requirements listed in Table 12. The details of outgassing test on our samples are given in Appendix.

Table 12: Limits of Low Outgassing Test.

ASTM E595	
Acceptable limits for space applications	TML < 1.0%
	CVCM < 0.1%

Chapter 4 Nanocomposites for Radiation Shielding Tests

Well dispersed nanofiller in nanocomposites possess better radiation shielding effectiveness than nanocomposites with poorly dispersed nanofillers. Investigation of dispersity of functionalized MWCNT with -COOH group in polymer matrix is crucial. Before radiation shielding tests, thermal and mechanical properties of fabricated nanocomposites were looked into. Samples with excellent enhanced thermal stability and tensile strength were selected for proton and electron radiation shielding tests. The methods of both radiation shielding tests are introduced in this section.

4.1 Sample Selection for Radiation Shielding Tests

4.1.1 Fabrication of PMMA and Nanocomposites

The melt mixer and a hot press instrument were used for PMMA nanocomposite fabrication. Fabricated samples were cut into specific shape required for further characterization and test. PMMA with various weight percentages (1, 3 and 5wt%) of MWCNT (PMMA/MWCNT) are produced. The photo of fabricated samples is shown in Figure 34. The fabrication steps of PMMA and its nanocomposites are listed:

PMMA:

Step 1: Pour as-received PMMA powders into hot press (15 cm × 15 cm) at temperature of 180 °C and compression force of 40,000 N.

Step 2: Cool the hot press down with air cooling then take it out.

PMMA/MWCNT:

Step 1: Setup the temperature and mix sheer rotating rate and pre-heat the melt mixer.

Step 2: Pour the PMMA powders into the mixer and keep the setups for 30 minutes.

Step 3: Pour related MWCNT-COOH loadings into mixer and keep the process for another 1 hour after torque of mixing material reaches stable level.

Step 4: Pour well mixed composite out into hot press (15 cm × 15 cm), and mold samples at temperature of 180 °C and compression force of 40,000 N.

Step 5: Cool the hot press down with air cooling then take it out.

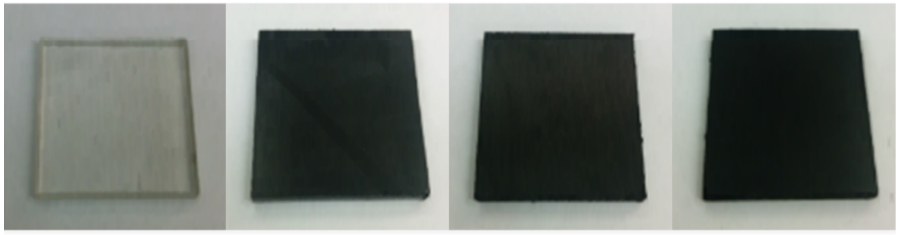

Figure 34: Fabricated (a) PMMA. (b) PMMA/1wt%MWCNT, (c) PMMA/3wt%MWCNT and (d) PMMA/5wt%MWCNT

4.1.2 Raman Spectroscopy and Fourier Transform Infrared Spectroscopy

Raman spectroscopy is an important tool for characterizing carbon-based nanostructures. Quality of the pristine and functionalized MWCNT has been assessed by the shift and width variation of peaks in the results of Raman spectroscopy [214].

Non-functionalized MWCNT were purchased from Nanocyl (Belgium) to compare with MWCNT with -COOH group. The Raman spectra of pristine MWCNT and MWCNT-COOH are shown in Figure 35. There are two prominent bands at 1320 cm^{-1} (D band) which indicates the presence of disorder in carbon structures, and the band at 1580 cm^{-1} (G band) which is the vibration mode of the C-C bond. The G' band in the Raman spectrum is at 2645 cm^{-1} which exhibits the MWCNTs contain graphene systems [214, 215]. The ratio of the intensities of the D and the G band (I_D/I_G) indicates the disorder and the defect density in graphene structures, which is often used to define the quality of carbon nanotubes [216]. The I_D/I_G of functionalized and pristine MWCNT are 2.08 and 1.65 respectively, the higher value of I_D/I_G for functionalized MWCNT indicates higher disorder and defects in the nanotubes [217]. With respect to the wavenumber, the functionalized MWCNTs shifts to higher spectrum for each band, which indicates less intertube interactions for MWCNT-COOH [214, 218].

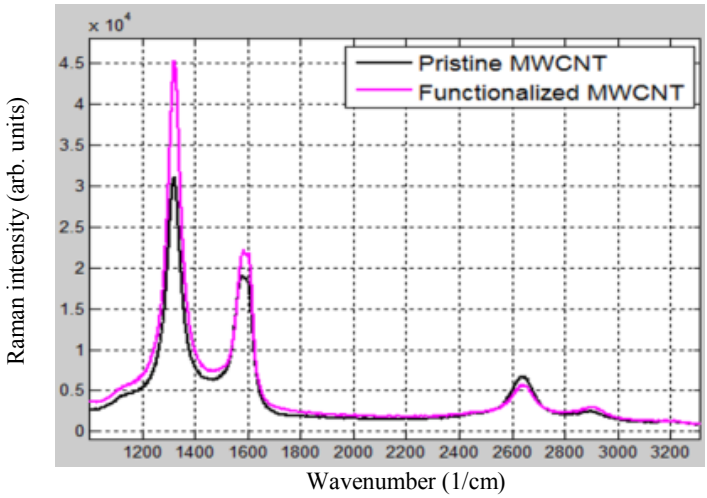

Figure 35: The Raman spectra of pristine MWCNT and functionalized MWCNT

Fourier Transform Infrared Spectroscopy (FTIR) results of pristine MWCNT and MWCNT-COOH are shown in Figure 36. For MWCNT-COOH, the most prominent peaks at 1044 cm^{-1} and 1723 cm^{-1} are attributed to carboxylic groups on the MWCNT, which has contributed C=C stretch at peaks of 1530-1560 cm^{-1} [219, 220]. Two bands at 2850 cm^{-1} and 2920 cm^{-1} are attributed to the defects of asymmetric and symmetric stretch of H-C-H bonds on MWCNT-COOH [220]. By analyze the results of Raman and FTIR, existence of -COOH group in functionalized MWCNT is proved and it is used in all the further tests and fabrications.

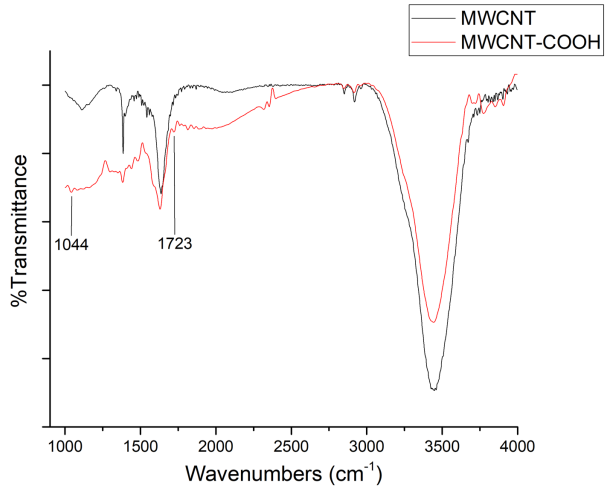

Figure 36: FTIR of pristine MWCNTs and functionalized MWCNT

4.1.3 Tensile Strength Test

PMMA and nanocomposites were measured and compared. All samples were laser cut into dog bone shape based on the ASTM D638-14 standard with testing speed of 5 cm/min (shown in Figure 32 right). Tensile strength data of PMMA and nanocomposites before and after thermal cycles are listed in Table 13.

Table 13: Tensile strength data

Materials		Before thermal cycles (MPa)	After thermal cycles (MPa)
PMMA		19.01	43.30
PMMA/MWCNT	1 wt% MWCNT	27.39	21.58
	3 wt% MWCNT	17.83	31.65
	5 wt% MWCNT	12.83	26.41

According to Table 13, before thermal cycles, PMMA/MWCNT (1 wt%) possessed highest tensile strength (27.39 MPa) followed by PMMA/MWCNT (3 wt%). After 10 thermal cycles treatment, tensile strength of samples except PMMA/MWCNT (1 wt%) had increased at different percentages. The lower tensile strength before thermal cycles should be caused by non-observable deformation, such as bending, during laser cut, which can melt or burn materials on its pass way. After thermal cycles, PMMA/MWCNT (3 wt%) shows highest tensile strength compared to other nanocomposites.

4.1.4 Thermogravimetric Analysis

Temperature was set increasing from room temperature to 800 °C at ramp of 20 °C/min in nitrogen environment. Figure 37 shows weight percentage changes of pristine MWCNTs (black), PMMA (green) and PMMA with 1 wt% (red), 3 wt% (blue) and 5 wt% (pink) MWCNTs. Pure PMMA and PMMA/ MWCNT (1 wt%) have similar curves, and the plot of PMMA/MWCNT (3 wt%) is extremely close to that of 5 wt% nanocomposite. For pure PMMA and 1 wt% complete degradation of the polymer occurred at 425 °C but with the incorporation of 3 and 5 wt% MWCNTs, the complete degradation temperature was found to be slightly shifted towards a higher temperature (from 427 °C to 440°C). Moreover, the degradation beginning point is 200 °C for PMMA and 1 wt%, but it is 250 °C for 3 wt% and 5 wt% ones, which achieved about 25% improvement. The weight reduction of PMMA and 1 wt% were much faster than 3 and 5 wt% for temperatures below 350 °C. Pristine MWCNTs lost about 27wt% in total when the temperature reached up to 800 °C. Zhaoxia Jin et al. has reported that addition of CNT in polymer nanocomposite can slow down

thermal degradation process of PMMA [221]. In conclusion, both 3 and 5 wt% MWCNT nanocomposites showed enhanced thermal stability than pure PMMA and 1 wt% PMMA/MWCNT.

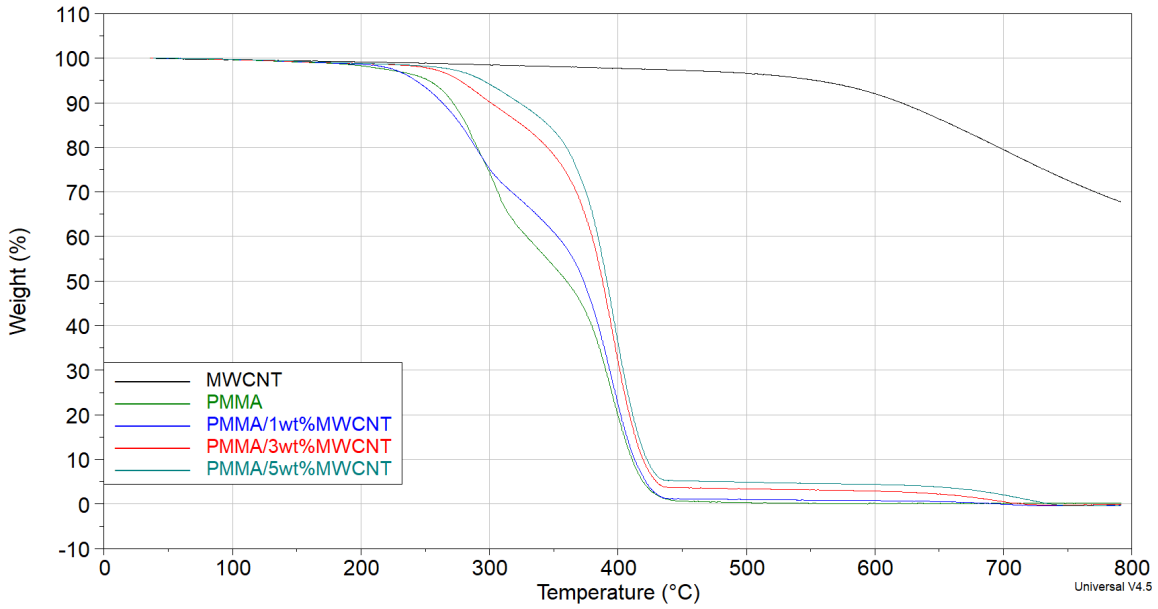

Figure 37: TGA plot of pristine MWCNT, PMMA and nanocomposites

4.1.5 Thermal Cycles

Based on the working temperature listed in Table 4, range of -100 to 130 °C was designed for thermal cycling. However, the machine in our lab was unable to reach temperatures below -68 °C, thus the test range shifted about 30 °C to higher range between -68 °C and 150 °C with temperature plateaus held for 30 minutes. 5 thermal cycles were applied on PMMA and PMMA with MWCNT-COOH sheets. According to the photos of sample after thermal cycles (Figure 38), samples with 5 wt% loading of MWCNT appear to have almost no differences comparing to as fabricated samples; the one with 3 wt% MWCNT loading appear to have some bubbles; but the sample with 1 wt% MWCNT loading shows the greatest morphology changes. Sample with 3 and 5 wt% MWCNT loading in PMMA matrix are showing better thermal stability according to the appearances. This phenomenon may be caused by addition of MWCNT which can fill in micro-gaps occurred during fabrication in polymer matrix.

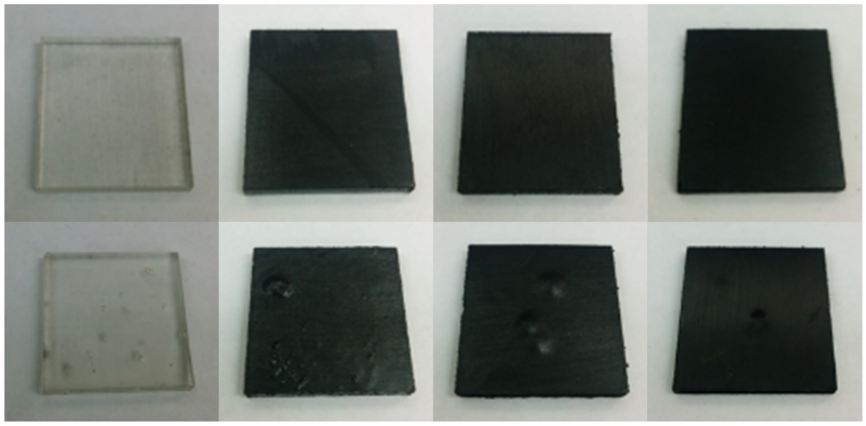

Figure 38: All samples (a): pure PMMA, (b): PMMA/1wt%MWCNT, (c): PMMA/3wt%MWCNT, (d): PMMA/5wt%MWCNT) before 5 thermal cycles (first line) and after (second line)

4.1.6 Summary

To pick an outstanding recipe for radiation shielding tests, the results have been discussed below:

Tensile Strength Test:

1. After thermal cycle treatment, tensile strength was increased for samples with 3 and 5 wt% of MWCNT loading except for the PMMA/1wt%MWCNT; however, the decrease for 1 wt% was not significant; the strength order: PMMA/MWCNT (3wt%): 31.65MPa > PMMA/MWCNT (5wt%): 26.41MPa > PMMA/MWCNT (1wt%): 21.58MPa;
2. PMMA/MWCNT (1 wt%) presented highest tensile strength before thermal cycles. However, its strength decreased after thermal cycle and became the weakest sample;
3. PMMA/MWCNT (3 wt%) presented similar strength as control, though the increased strength after thermal cycle was less than the change of control.
4. PMMA/MWCNT (5 wt%) presented the lowest tensile strength before thermal cycle treatment and the second lowest strength after thermal cycle treatment.

TGA:

Nanocomposites added by 3 wt% and 5 wt% MWCNT have higher beginning degradation temperature (250 °C) than pure PMMA and 1 wt% MWCNT loaded nanocomposite (200 °C). Moreover, complete degradation of pure PMMA and 1 wt% MWCNT loaded nanocomposite occurs at ~425 °C but with the incorporation of 3 wt% and 5 wt% the complete degradation temperature of nanocomposite was found to be about 3% higher than 1 wt% MWCNT loaded nanocomposite. Thus, Nanocomposites with 3 wt% and 5 wt% MWCNT were considered.

Surface Morphology Inspection:

Visual inspection of the surface morphology of samples before and after thermal cycles was performed. As shown in Figure 38, there were significant visual changes on the PMMA with MWCNT loading of 1 wt% in comparison to 3 and 5 wt% samples with the least changes observed in the 5 wt% nanocomposite.

Visual inspection of samples, 3 and 5 wt% MWCNT loaded nanocomposites after 5 thermal cycles showed less changes compared to PMMA with 1 wt% MWCNT and control. Similarly, the temperature of thermal decomposition was observed about 25% higher for PMMA mixed with 3 and 5 wt% MWCNT compared to PMMA and 1 wt% MWCNT loaded nanocomposite in TGA plot. Furthermore, PMMA with 3 wt% MWCNT presented higher tensile strength (Table 13) than other nanocomposites after thermal cycling treatment. It was also reported that the functionalized MWCNT is able to achieve electrical conducting percolation of 3 wt% [222].

In order to have a balance among mechanical strength and thermal properties, PMMA with 3 wt% of MWCNT loading was hereby selected for further tests including proton radiation shielding test. In addition, outgassing properties of PMMA/3wt%MWCNT nanocomposite and pure PMMA have been tested in a commercial lab. The result suggests both materials fabricated in our lab can pass low outgassing materials standard for space applications (shown in Appendix).

4.2 TRIUMF

TRIUMF is Canada's national particle accelerator center, which is consistently recognized as Canada's premier physics laboratory and an international leader of subatomic physics research center. TRIUMF has the world's largest cyclotron located on the south campus of its own founding member, University of British Columbia in Vancouver. Proton sources up to 520 MeV can be generated in the facilities [223]. As shown in Figure 39, proton source for proton therapy with energy of 105 MeV was used in our research.

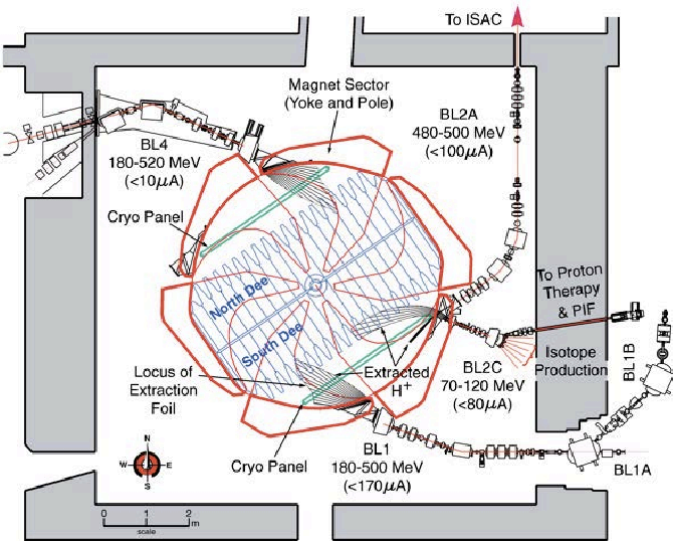

Figure 39: Scheme of cyclotron in TRIUMF [224]

4.2.1 Experiment Setup

To simulate the space radiation environment and test shielding materials, we accessed to a particle-radiation facility (on BL2C, TRIUMF, Vancouver, BC, Canada) with high-energy proton beams. The experimental set-up for the proton radiation tests is shown in Figure 40. For space applications the average proton energies are lower than proton source BL2C (<120 MeV). Also, the proton energy that produces most of the dose to payloads after aluminum shielding is in the range of 30-100 MeV, so the measurements from BL2C are relevant for space applications.

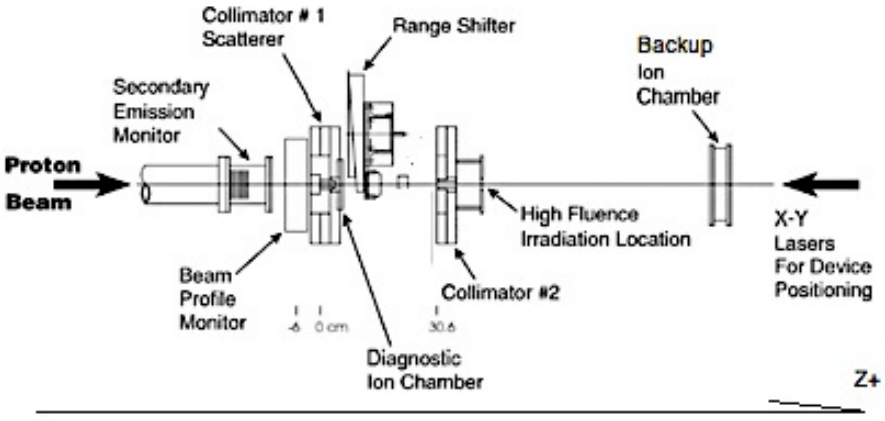

Figure 40: Device arrangement of stopping power measurement

- Proton beam properties: (i) Energy levels of proton beam were set to 105 MeV and 63MeV; (ii) Intensity of proton beam was 4~5 nA (1~2×10^8 protons/cm^2/s); (iii) Beam size at the position, where the sample was placed, was 19mm in diameter.

- Diagnostic ion chamber and backup ion chamber: Both of them measure the radiation dose, which is the energy deposited by protons. Readouts of chambers are proportional to the number of protons that transmitted the chambers. Name the readout of backup chamber as BIC and the readout of the diagnostic ion chamber as DIC. The ratio of BIC/DIC is calculated to obtain relative dose change, which is also the dose transmission rate, of the penetration process through shielding materials.

- Range shifter: Range shifter (RS) is a rotatable and auto-controlled Lucite plate. The position of Lucite plate that is located in the beam has adjustable thickness ranging from 0 to 40mm. The thickness adjustment resolution is 0.01mm, which is labeled by RS values from 0 to 4000. By rotating the Lucite plate, energy of initial incident proton beam on the shielding materials can be adjusted. Rotation angle and stopping time can be automatically controlled. [225] RS values can be converted to water equivalent thickness (WET) according to Equation 1. Water equivalent thickness is defined as [226]:

$$WET = 1.156 \times (2.23 + 1.0075 \times 10^{-2} \times RS_{90\%})$$

- Sample frame: A height adjustable sample frame is placed next to collimator #2 with diameter of 19 mm at the Z+ direction. Shielding materials under test is placed on the top of the frame and fully block the hole of collimator #2.

Specifications for samples under test are all given in Table 14. Sample thickness were simulated by Stopping and Range of Ions in Matter (SRIM), which was used to simulate the interaction processes between the incident protons and the target material [227]. For a given composition and mass density of a material, the proton stopping range can be calculated using SRIM. The stopping range of all materials, considered for the experiments, was obtained using SRIM.

Table 14: Samples specifications

Materials	Aluminum	PMMA	PMMA/MWCNT
Density	2.698 g/cm^3	1.194 g/cm^3	1.204 g/cm^3
Length x breadth	4 x 4 cm		
Sample #1 Thickness	6.24 mm	9.10 mm	9.08 mm
Sample #2 Thickness	12.54 mm	24.80 mm	24.82 mm
Sample #3 Thickness	18.86 mm	34.02 mm	34.30 mm
Sample #4 Thickness	25.2 mm	43.40 mm	43.44 mm

As shown in Figure 41, the proton beam direction is aligned to go through testing samples [163]. Range shifter is placed between proton beam source and samples. A neutron detector (BF_3) is added at the side of the sample for detecting the generated secondary neutron caused by the proton radiation. The neutron detector is placed at the same horizontal plane of the sample.

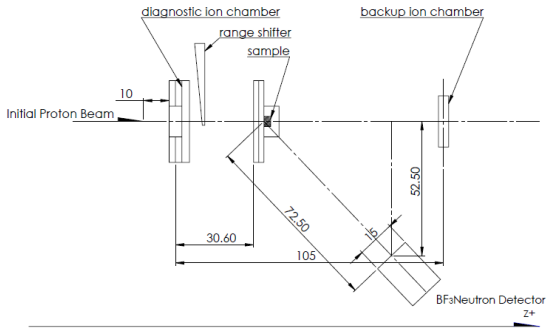

Figure 41: Experimental setup illustration, unit in cm

4.2.2 Experiment Procedure

Once it is setup, proton beam with energy of 100 MeV was delivered, and a range scan was carried out from the lowest range shifter (RS) value of 200 to beyond the end of the range at steps of 100 (approximate 1 mm RS). The incoming protons were measured by Diagnostic ion chamber DIC and the protons passing through the sample were measured with ion chamber BIC. After the protons were essentially all stopped, the signal from the BIC monitored any charged particles or neutrons interacting nearby. This signal was very small. Once the end of range was found a more accurate scan at steps of 20 can be used to measure the end of range to an accuracy of 0.1 mm RS.

All samples are tested under the same procedure. Due to the thickness limitation of the range shifter, extra Lucite plates, which are made of the same materials as the one of range shifter, are placed between the range shifter and the sample. The procedure is illustrated in steps:

Step 1: Range shifter (RS) scan from 200 to 3800 with step-in RS of 100 div.

Step 2: Record the counts at diagnostic ion chamber (DIC) and backup ion chamber (BIC), and then calculate their ratio (BIC/DIC).

Step 3: Observe the plotted curve of BIC/DIC vs. RS, determine the detailed plotting range of RS (Table 15 and Figure 42).

Step 4: In the detailed plotting range of RS, step-in RS is set to 20 div, repeat RS scan.

Step 5: Record the counts at DIC and BIC and calculate the ratio of BIC/DIC.

Step 6: Plot the curve of BIC/DIC vs. RS and calculate the RS position at 90% of the peak BIC/DIC value.

Step 7: WET of the RS at 90% for each material (denoted as $t_{RS90\%}^{WET}$), at the position of RS90%, was calculated using the following equation: $t_{RS90\%}^{WET} = 1.156 \times (2.23 + 1.0075 \times 10^{-2} \times RS_{90\%})$.

Step 8: The stopping range of proton beam in water with the incident proton energy E, denoted as t_E^{WET}, was calculated by SRIM.

Step 9: WET of each material under test, t^{WET}, was obtained using the following equation: $t^{WET} = t_E^{WET} - t_{RS90\%}^{WET}$.

Step 10: Move the range shifter to the positions of 3800, $RS_{90\%}$ and 200. At each position, apply proton beam and records the counts at DIC and BF_3. Three pairs of counts (DIC and BF_3) are recorded at each RS position for secondary neutron evaluation.

Table 15: Details of range shifter

	Aluminum (mm)	**RS Range**	**PMMA (mm)**	**RS Range**	**PMMA/MWCNT (mm)**	**RS Range**	**Lucite Thickness (mm)**
#1	6.24	2000 to 3500	9.10	2000 to 3500	9.08	2000 to 3500	30.06
#2	12.54	2000 to 3500	24.80	1800 to 3300	24.82	1800 to 3300	18.12
#3	18.86	1800 to 3000	34.02	1500 to 3000	34.30	1500 to 3000	11.94
#4	25.20	1800 to 3000	43.40	1800 to 3300	43.44	1800 to 3300	0

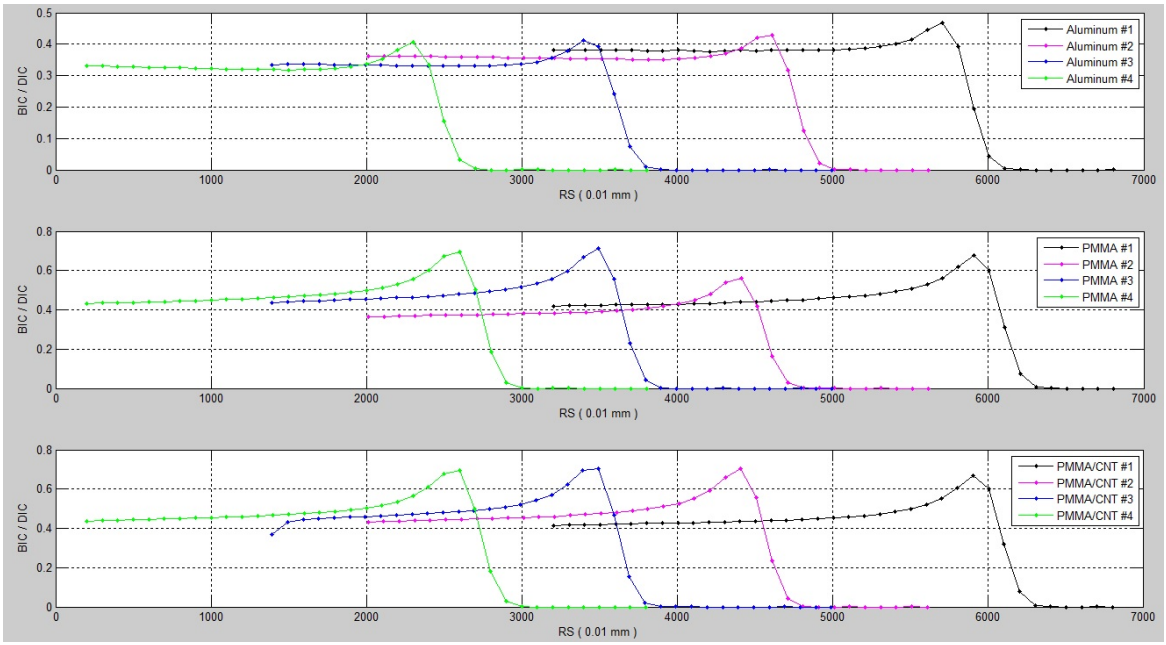

Figure 42: BIC/DIC vs. RS curves with step-in RS of 100 div.

4.2.3 Experiment Results

(i) Proton Radiation Shielding

WETs of samples and the corresponding stopping energies of protons are calculated. Compensated RS90%, Sample thicknesses, Proton energies, and Water equivalent thicknesses are calculated and summarized in Table 16.

Table 16: WETs of samples and the corresponding stopping energies for each sample

	Compensated $RS_{90\%}$ (0.01 mm)	RS WETs (mm)	Sample Thickness (mm)	Sample WETs (mm)	Stopping Energy (MeV)
Aluminum #1	5781.6	69.91	6.24	13.01	37.50
Aluminum #2	4661.2	56.87	12.54	26.05	55.05
Aluminum #3	3511.4	43.47	18.86	39.45	69.31
Aluminum #4	2373.6	30.22	25.20	52.70	81.45
PMMA #1	5996.5	72.42	9.10	10.50	33.32
PMMA #2	4464.2	54.57	24.80	28.35	57.69
PMMA #3	3558.1	44.02	34.02	38.90	68.77
PMMA #4	2650.3	33.45	43.40	49.47	78.63

PMMA/MWCNT #1	6004.1	72.51	9.08	10.41	33.15
PMMA/MWCNT #2	4479.3	54.75	24.82	28.17	57.49
PMMA/MWCNT #3	3526.8	43.65	34.30	39.27	69.13
PMMA/MWCNT #4	2646.9	33.41	43.44	49.51	78.66

There are three types of samples and each sample has four different thicknesses. Thus, four WET were obtained for each type of materials. Areal density of material is used to evaluate the proton shielding efficiency by timing material thickness with material density. Areal densities of materials and the water equivalent areal density (WEAD), which is calculate by timing WET with water density, corresponding to WET are summarized in Table 17.

Table 17: Areal Densities and WEADs

Aluminum				
Density	2.698 g/cm^3			
	Thickness (mm)	Areal Density (g/cm^2)	WETs (mm)	WEAD (g/cm^2)
Sample #1	6.24	1.68	13.01	1.30
Sample #2	12.54	3.38	26.05	2.61
Sample #3	18.86	5.09	39.45	3.95
Sample #4	25.20	6.80	52.70	5.27
PMMA				
Density	1.194 g/cm^3			
	Thickness (mm)	Areal Density (g/cm^2)	WETs (mm)	WEAD (g/cm^2)
Sample #1	9.10	1.09	10.50	1.05
Sample #2	24.80	2.96	28.35	2.84
Sample #3	34.02	4.06	38.90	3.89
Sample #4	43.40	5.18	49.47	4.95
PMMA/MWCNT				
Density	1.204 g/cm^3			
	Thickness (mm)	Areal Density (g/cm^2)	WETs (mm)	WEAD (g/cm^2)
Sample #1	9.08	1.09	10.41	1.04
Sample #2	24.82	2.99	28.17	2.82
Sample #3	34.30	4.13	39.27	3.93
Sample #4	43.44	5.23	49.51	4.95

Areal density of materials and their WEADs follow linear relationships. Thus a line fitting is applied to the data given in Table 17 with regards to the weight efficiency for shielding proton. PMMA and PMMA/MWCNT were found to be 18.89% to 19.89% and 17.86% to 18.71% lighter than Al respectively (Table 18).

Table 18: Weight comparison among materials for proton stopping

	Slope ***k*** **(RMSE[1])**	Compared to Al[2]
Aluminum	0.7744 (0.0932)	--
PMMA	0.9564 (0.0881)	**18.89% to 19.89% lighter than Al**
PMMA/MWCNT	0.9475 (0.1207)	**17.86% to 18.71% lighter than Al**

[1] RMSE: Root Mean Square Error: $RMSE = \sqrt{\frac{\sum_{t=1}^{n}(\hat{y}_t - y_t)^2}{n}}$

Where:

n is the number of the measured data and n = 4

$\hat{y}_t$ is the fitted value;

y_t is the measured value for n times

[2] If two materials (M_1 and M_2) with areal densities AD_1 and AD_2 can both fully stop protons with energy of E. Their water equivalent areal densities are the same: $WEAD = k_1 \times AD_1$ and $WEAD = k_2 \times AD_2$, respectively. Then the weight efficiency of M_1 compare to the one of M_2 in percentage will be:

$$\gamma = \frac{AD_1 - AD_2}{AD_2} \times 100\% = \frac{WEAD/k_1 - WEAD/k_2 \times 100\%}{WEAD/k_2} = \frac{1/k_1 - 1/k_2}{1/k_2} \times 100\% = \frac{k_2 - k_1}{k_1} \times 100\%$$

(ii) Neutron Radiation

From the neutron experimental setup, it was found that the neutrons detected by BF_3 were from both the irradiated samples (SN_{sample}) and the materials used in the setup (SN_{setup}) encountered by the incident radiation before reaching the sample. The samples not only generated SN_{sample}, but also attenuated the SN_{setup}. Therefore, the readouts of sample group #4, which is the thickest group of all the samples, was considered suitable for evaluating secondary neutron generation. Samples in group #4 maximized the shielding of the SN_{setup} and contributed the most SN_{sample}. Furthermore, in order to evaluate the SN_{setup}, the readout of the BF_3 with no sample were also recorded and used as background signal.

Three readouts of DIC and BF_3 for each sample in group #4 at each energy level were recorded as shown in Table 19. The ratios of BF_3/DIC and their averages were also calculated. Table 20 shows the average BF_3/DIC ratio of background secondary neutron generation at two different range shifter position.

Table 19: Data for secondary neutron detection

	DIC	BF_3	BF_3/DIC	Energy (MeV)	DIC	BF_3	BF_3/DIC	Energy (MeV)	DIC	BF_3	BF_3/DIC	Energy (MeV)
Aluminum #4	25810	258930	10.03	101.46	25798	217315	8.42	81.45	25703	190997	7.43	65.95
	25652	258075	10.06		25520	215310	8.44		25401	189130	7.45	
	25951	260991	10.06		25899	218056	8.42		25561	190180	7.44	
			10.05				8.43				7.44	
PMMA #4	27071	261566	9.66	101.46	26240	208344	7.94	78.63	26196	190195	7.26	65.95
	27060	260419	9.62		27176	214779	7.90		26234	189949	7.24	
	27083	262023	9.67		27113	215363	7.94		26150	190162	7.27	
			9.65				7.93				7.26	
PMMA/MWCNT #4	29594	282842	9.56	101.46	29180	228586	7.83	78.66	29654	212824	7.18	65.95
	29648	282981	9.54		29202	229750	7.87		29104	208548	7.17	
	29683	282697	9.52		29546	231806	7.85		29041	207624	7.15	
			9.54				7.85				7.16	

Table 20: Background measurements

Range shifter position (0.01mm)	**Average**
200	9.80
3800	7.43

4.3 LINAC

A linear particle accelerator (LINAC) is a type of particle accelerator that accelerates charged subatomic particles or ions to a high speed by subjecting them to a series of oscillating electric potentials along a linear beamline [228]. The medical-purpose LINAC machine, used in this research, is located at the Grand River hospital, Waterloo. It is capable of producing electron beam (up to 20 MeV) and photons (up to 15 MeV) for multiple purposes (Figure 43). Regarding electron radiation, electron source generated from accelerator is constrained to beam by electron applicator before reaching targets.

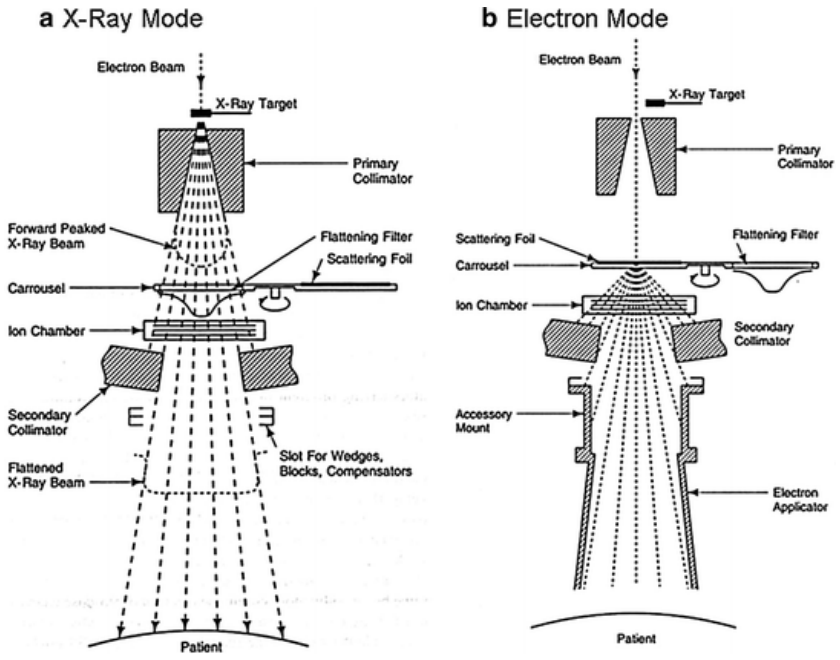

Figure 43: Scheme of LINAC [229]

In our study, electron beam mode was used to simulate electron radiation in space. Energies of electron beam was set to be 9, 12, 16 and 20 MeV. As discussed in literature review, electron with energies up to 7 MeV have most dense dose in LEO. However, looking upon interplanetary travel, such as journey to Jupiter, electron flux with energies up to 20 MeV predominantly contribute radiation dose on spacecraft.

PMMA with 3wt% of MWCNT was selected for proton radiation shielding; therefore, the sample, PMMA/3wt%MWCNT, was chosen for further enhancement to shielding high energy electron radiations. As discussed in section 2.4.2, Bi_2O_3 in nanocomposite is expected to effectively attenuate electron beam. Therefore, the nanopowders were dispersed in PMMA/3wt%MWCNT to form new nanocomposite PMMA/2.1wt%MWCNT/30wt%Bi_2O_3. The same fabrication process was used as PMMA/3wt%MWCNT followed by the same hotpress and laser cut procedure to produce square shaped test specimens. Detailed electron radiation shielding experiment is discussed in chapter 6.

Chapter 5 PMMA/MWCNT Nanocomposite for Proton Radiation Shielding Applications

5.1 Introduction

For outer space activities, energetic-particle-radiation from GCR and solar particle events are one of the major concerns [230, 231]. The energies of the radiation particles are in the range of 1MeV/nucleon to 10 GeV/ nucleon. About 80% of the GCR is comprised of highly energetic protons capable of having damaging effects on electronics and astronauts by energy deposition and atom displacement in the irradiated materials [6, 41, 232]. During manned missions, exposure to either long-term dose accumulation or short-term radiation may result in fatal health problems such as carcinogenesis, organ failure or even genetic mutation [233-237]. In order to protect the payloads and the astronauts from the adverse effects of particle radiation, a lightweight effective shielding layer incorporated as part of the structural material may be a solution for a successful space mission.

In principle, materials with higher charge-to-mass ratio (Z/A) will be more efficient in absorbing energy from incident-charged particles through Coulomb interactions [12, 238]. In comparison with low-atomic-number (low-Z) materials, high-Z materials, such as aluminum alloys, that are heavier in weight achieve the shielding performance similar to that of low-Z materials. Hydrogen has the highest Z/A ratio, but pure hydrogen or even water is difficult to store and consequently adds to the overall launch cost. As a result, the use of pure hydrogen and water are limited in the space industry. However, the materials rich in hydrogen content, such as low-Z polymers, are considered good shielding materials against particle radiation [233, 238-240]. Compared with aluminum alloys, low-Z polymers, such as PE and PMMA, are lower in mechanical strength, and electrical and thermal conductivity. Subsequently, numerous studies have investigated different types of polymer-based composites in order to find lightweight alternatives to aluminum alloys with acceptable strength and good performance against radiation [238, 241, 242]. Without significantly affecting the overall weight, nano/micro-sized fillers can be dispersed in the polymer matrix in improve mechanical strength, electrical properties, thermal properties, electromagnetic interference shielding, photon radiation shielding and neutron attenuation characteristics [243-250]. However, the addition of the fillers was found to have minimal impact on the radiation shielding efficiency of the polymer composites against charged particles [238, 251].

Moreover, radiation damage induced by secondary neutrons cannot be ignored. Compared to other ionizing radiation sources, the secondary neutrons are more difficult to shield because of their

electroneutrality. The nuclei of these high-Z materials have higher possibility to fragment upon energetic particle radiation and generate secondary radiation, which include neutrons, protons, electrons and even x-rays and γ-rays. The secondary radiation would induce additional radiation damage in addition to that from primary radiation [241]. Targeting methods that reduce the possibility of generating secondary neutrons could be more weight-efficient in reducing radiation induced damage. As a result, evaluation of shielding materials should also include the measurement of secondary radiation, especially the secondary neutrons.

CNT has been demonstrated as efficient filler materials for enhancing the polymer's mechanical strength, electrical and thermal conductivity and providing the function of electromagnetic shielding [252-255]. However, to the best of our knowledge, the role of CNT in reducing the generation of secondary neutrons upon interaction with high-energy particle radiation has not been documented. In comparison with SWCNT, MWCNT have better resistance to radiation. Carbon atoms of MWCNTs have a higher atom displacement threshold than those of SWCNT and the knocked-off carbon atoms can be quickly relocated to the neighboring wall, minimizing the structural damage [256]. The MWCNT also require less energy than SWCNT to break the van der Waals force within the CNT bundles, thus MWCNT can achieve better dispersion in the polymer matrix performing with better reinforcement effect [257, 258]. On the other hand, PMMA was chosen as polymer matrix for loading CNT because the composition of PMMA contains low-Z elements (carbon, hydrogen and oxygen) resulting in a lower possibility of secondary neutron generation. Furthermore, the performance of PMMA against radiation in space has been extensively studied [259-263]. Thus the focus of our research is on the shielding performance of the CNT.

In this study, the PMMA/MWCNT nanocomposite was fabricated with 3 wt% of MWCNTs and the proton transmission and secondary neutron generation properties were evaluated under proton radiation with energy up to ~80 MeV. The performance of the nanocomposite was also compared with that of pure PMMA and aluminum. Moreover, material properties of both pure PMMA and PMMA/MWCNT samples were investigated using TGA, DSC and a tensile strength tester.

5.2 Methods

PMMA/MWCNT nanocomposite was fabricated and the material properties were compared to those of the pure PMMA. Pure PMMA and aluminum were used as reference materials. The proton transmission properties of the three materials and the secondary neutron generation under proton

radiation were inspected in Canada's national laboratory for particle and nuclear physics, Vancouver, BC, Canada.

5.2.1 Fabrication

PMMA/MWCNT samples were fabricated using melt-mixing and hot-pressing processes. PMMA powder (Sigma Aldrich, #182230) was, firstly, fed into the melt-mixer (Haake Rheocord 90) at 200 °C forming a melt-flow of the polymer. Carboxyl functionalized MWCNT (MWCNT- COOH) (Nanostructured & Amorphous Materials, USA) were then added to the melt-mixer and mixed with PMMA for an hour. Functionalized MWCNTs were used to improve the dispersion quality of the MWCNTs in PMMA through increased interfacial bonding between the surface of the MWCNT-COOH and the polymer chains. PMMA/MWCNT nanocomposites and pure PMMA pellets were then pressed into 3 mm thick individual sheets through a compression molding technique. Each of the samples was pressed at 180 °C under a pressure of about 1.6 MPa. Aluminum plates (McMaster-Carr Supply Company, Al 1100, thickness of 1⁄4′′) were machined into a size of 4 × 4 cm for use as reference material in order to compare the shielding performance of the PMMA samples. Both pure PMMA and PMMA/MWCNT sheets were also machined into the dimensions equal to the aluminum samples.

5.2.2 Characterization

The fabricated PMMA and PMMA/MWCNT samples were characterized with TGA, DSC, and tensile strength measurement. The TGA of PMMA and PMMA/MWCNT were measured after the proton radiation test in order to inspect the radiation effects on the thermal stability of the materials. Another thermal property, the glass transition temperature of PMMA and its nanocomposite has been measured by DSC. Furthermore, in order to study the effects of any air trapped during material fabrication and the effects of radiation exposure on the samples, an environmental chamber was used to perform thermal cycling treatment on the irradiated and non-irradiated PMMA and the PMMA/MWCNT samples.

TGA was performed on Q500 from TA instruments. The sample weight loss corresponding to the increase in the temperature (from 0 °C–800 °C) was monitored at a rate of 20 °C min^{-1}. The TGA results of both the irradiated and non- irradiated PMMA and PMMA/MWCNT samples were evaluated and compared.

DSC was performed on Q2000 from TA instruments in order to measure the glass transition temperature (*Tg*). The heat flow change versus temperature change ranging from 25 °C–180 °C was recorded to measure the *Tg*. The temperature of the whole measurement process was first increased from 25 °C–180 °C with rate of 10 °C min−1 and then decreased from 180 °C–25 °C with rate of 20 °C min^{-1}. The pure PMMA and PMMA/MWCNT samples for the DSC test contained non-irradiated samples, irradiated samples (middle portions of the square samples that proton beam transmitted), and a non-irradiated portion of the irradiated samples (corner portions of the square samples that were not on the prime proton beam direction).

The tensile strengths of both the irradiated and non- irradiated pure PMMA and PMMA/MWCNT samples were measured with an Instron 5548 Micro Tester following the ASTM standard of D638-10. Samples were prepared with the required shape and dimensions with a laser engraving system (universal Laser System VersaLASER 2.30).

The environmental chamber from Cincinnati Sub-Zero Products Inc. can provide an environment with controllable temperature and humidity. Both of the pure PMMA and PMMA/MWCNT samples and both the irradiated and non- irradiated samples were placed in the chamber for thermal treatment: the temperature was increased from room temperature to 80 °C and the temperature was maintained at 80 °C for half an hour. The temperature was then increased to 180 °C with incremental temperature of 10 °C. At each temperature step, the temperature was also maintained for half an hour. The samples were monitored during the thermal treatment process so that any trapped air in the samples could be observed as air bubbles, especially at temperatures higher than the glass transition temperatures.

5.2.3 Proton radiation tests and secondary neutrons monitoring

The materials were tested for proton transmission, and secondary neutron generation. The experimental setup is illustrated in Figure 41. The proton transmission properties of the materials were characterized from the water-equivalent thicknesses (WETs) and water-equivalent areal densities (WEADs) of the samples [264]. Based on the concept of WETs and WEADs, the thickness and weight of different materials can be normalized to the thickness and weight of water for comparison. Moreover, the secondary neutrons generated during the proton radiation process were monitored by setting up a neutron detector in the back of the sample under test.

As shown in the Figure 41, the range shifter (Lucite plates), and the sample were placed in between two ion chambers, diagnostic ion chamber (DIC) and backup ion chamber (BIC). The initial beam

energy was 105 MeV with proton intensity of 5 nA (flux = 2×10^8 protons cm^{-2} s^{-1}) and spot size of 19 mm in diameter. Gradually we increased the thickness of the range shifter so that the energy of the protons bombarded on the sample decreased. At certain thickness of the range shifter, there were just no protons that penetrated through the sample. The difference between the water-equivalent thickness of the range shifter and the stopping range of the protons in water corresponding to the initial beam energy was the water-equivalent thickness of the sample. A detailed description about the experimental setup and procedure for measuring water-equivalent thickness can be found elsewhere [265]. Three materials (aluminum, PMMA and PMMA/MWCNT) with four different thicknesses of each material were prepared for the tests. Thickness information of all materials can be found in Table 21.

Table 21: Sample thicknesses (in mm).

Materials	Aluminum	PMMA	PMMA/MWCNT
Sample #1	6.24	9.10	9.08
Sample #2	12.54	24.80	24.82
Sample #3	18.86	34.02	34.30
Sample #4	25.20	43.40	43.44

In order to monitor the secondary neutron generation from the sample during the proton radiation process, a neutron detector (BF_3) was placed behind the sample. During the neutron test, the initial beam energy of the protons was reduced from 105 to 65.95 MeV (energy can be fully stopped by samples) and 101.46 MeV (energy can be partially stopped by the samples) by adjusting the thickness of the range shifter. The secondary neutron production under the two circumstances can be compared. The thicknesses of aluminum, PMMA and PMMA/MWCNT for the neutron test were 25.20, 43.40 and 43.44 mm, respectively. Each sample was irradiated with the two energies and the readouts of the DIC and BF_3 were recorded. Because the setup in front of the sample also produced secondary neutrons, the readouts of the DIC and BF_3 were also recorded when there was no sample placed and these data were noted as background data. When the sample was placed, it both attenuated the secondary neutrons from the setup and generated new secondary neutrons. The higher the secondary neutron attenuation and the lower the secondary neutron production, the lower the BF_3/ DIC ratio. Thus, the BF_3/DIC ratios of the samples gave an overall evaluation on both the neutron attenuation and generation ability. This setup would be conceptually similar to the environment in a real spacecraft: equipment protected by a layer of radiation shielding material.

5.3 Results and discussion

5.3.1 Proton transmission characteristics

Four water-equivalent thicknesses of each material (aluminum, pure PMMA and PMMA/MWCNT) were measured and calculated. According to the measured material densities and the water density, the thickness information was then converted to areal densities. The sample areal densities and the corresponding water-equivalent areal densities are given in Table 22. The maximum energies of protons that can be stopped by the samples are also provided.

Table 22: Areal densities (ADs), water equivalent areal densities (WEADs) and maximum proton energies that can be stopped by the samples.

	Aluminum				**PMMA**				**PMMA/MWCNT**			
Density (g/cm^3)	2.698				1.194				1.204			
	#1	#2	#3	#4	#1	#2	#3	#4	#1	#2	#3	#4
AD (g/cm^2)	1.68	3.38	5.09	6.80	1.09	2.96	4.06	5.18	1.09	2.99	4.13	5.23
WEADs (g/cm^2)	1.30	2.61	3.95	5.27	1.05	2.84	3.89	4.95	1.04	2.82	3.93	4.95
Maximum energies of protons that can be stopped by the samples (MeV)	37.50	55.05	69.31	81.45	33.32	57.69	68.77	78.63	33.15	57.49	69.13	78.66

Material areal densities versus corresponding water-equivalent thickness were found following a linear relationship as shown in Figure 44. When a line fitting was applied to the data points, the slopes of the fitted lines were 0.7744, 0.9564 and 0.9475 with root mean square (RMS) fitting errors of 0.0932, 0.0081 and 0.1207, for aluminum, PMMA and PMMA with 3wt% MWCNT, respectively. The points of PMMA and PMMA/MWCNT presented minor differences with each other and thus, it is considered that adding MWCNTs with 3 wt% would not affect the proton shielding properties of the PMMA matrix. Furthermore, the slope of the fitted line can be used to calculate the weight efficiency of the PMMA and PMMA/MWCNT compared with aluminum. Take PMMA for example, the slope of the PMMA line is $kp = 0.9564$ and the slope of aluminum is $ka = 0.7744$. In order to stop protons with certain energy level E with corresponding water-equivalent areal densities of AD, the required areal density of aluminum will be AD/ka and the one for PMMA will be AD/kp. Such that the weight efficiency of PMMA over aluminum is calculated by: $[(ka - kp)/kp] \times 100\%$. And by doing the same calculation for PMMA/MWCNT, it can be found that

PMMA/MWCNT and PMMA are about 18%–19% lighter than aluminum for providing the equivalent proton shielding effectiveness as that obtained from aluminum.

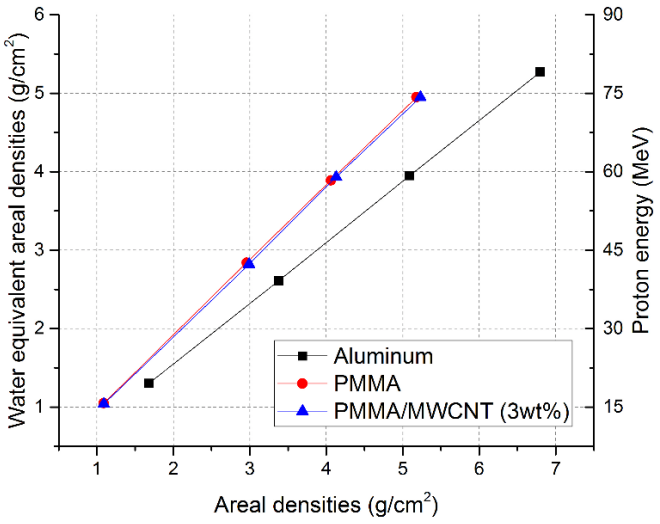

Figure 44: Areal densities of materials were normalized to water equivalent areal densities for comparison

5.3.2 Secondary neutron generation

The average ratio of BF_3/DIC of background, aluminum, PMMA and PMMA/MWCNT were calculated and compared as shown in Figure 45. Both PMMA and PMMA/MWCNT samples clearly show a lower BF_3/DIC ratio than the back-ground and aluminum, which means that by applying PMMA or PMMA nanocomposite as a shielding layer, the delivered secondary neutron to the equipment can be reduced. Furthermore, the BF_3/DIC ratio for PMMA/MWCNT shows a lower value compared to that of pure PMMA.

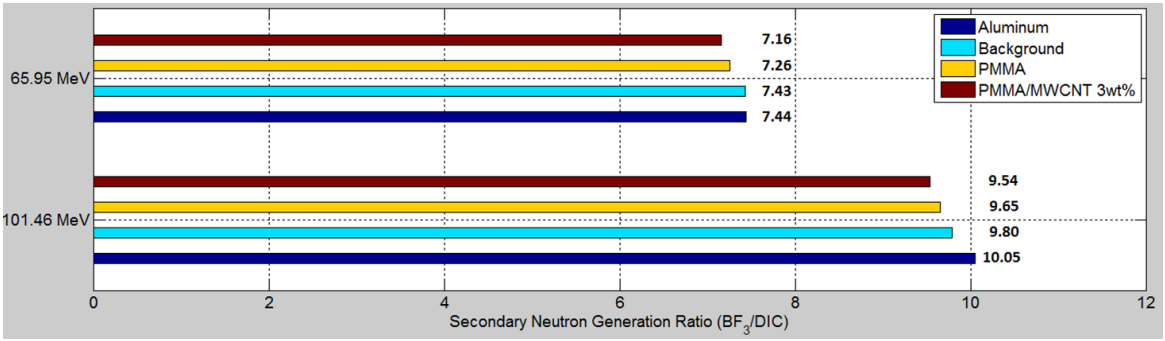

Figure 45: Secondary neutron generation ratios were compared under two incident proton energies of 65.95MeV and 101.46 MeV. Neutrons generated by background were those from the setup in front of the sample.

In principle, a good shielding material should not only be able to attenuate the secondary neutrons generated by the metallic structural materials, but should have minimal generation of the secondary neutrons. This would require a smaller BF_3/DIC ratio and furthermore, the ratio should be less than the ratio of the background at least. According to the neutron test results, one can speculate that the addition of MWCNT in PMMA either improves the neutron absorption ability or reduces the secondary neutron production of the polymer matrix; or enhances the both properties in the nanocomposite material. But in both ways, the addition of MWCNT presented a positive performance with regard to neutron shielding.

5.3.3 Material properties and radiation-induced effects

Figure 46 shows that the measured *Tg* temperatures from the DSC test of the pure PMMA and the PMMA/MWCNT composite are 101.22 °C and 111.20 °C, respectively. The MWCNT network in the PMMA matrix may have decreased the mobility of the PMMA polymer chain, which thus showed a ~10°C increase in the *Tg* in comparison to that of pure PMMA.

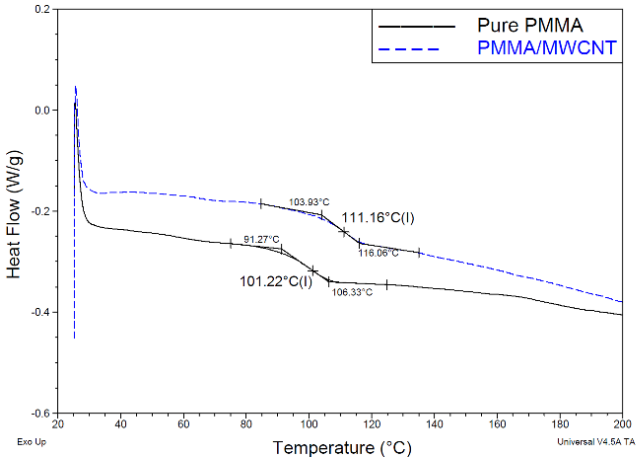

Figure 46: Glass transition temperatures of pure PMMA and PMMA/MWCNT using DSC technique.

The TGA results of the non-irradiated materials, shown in Figure 47 indicate that the PMMA/MWCNT composite has better thermal stability than the pure PMMA. The solid lines present the remaining weight percentage against the chamber temperature; and the dashed lines show that the rate of weight loss corresponds to temperature change. The pure PMMA presented a peak of weight loss rate at 305 °C, indicative of an unstable state of the material, while no such peak can be observed for the PMMA/MWCNT. Considering the remaining weight-to-temperature change curves, the pure PMMA has lost 25% of the original weight at 317 °C, but the PMMA/MWCNT showed a weight loss of only 11% at the same temperature.

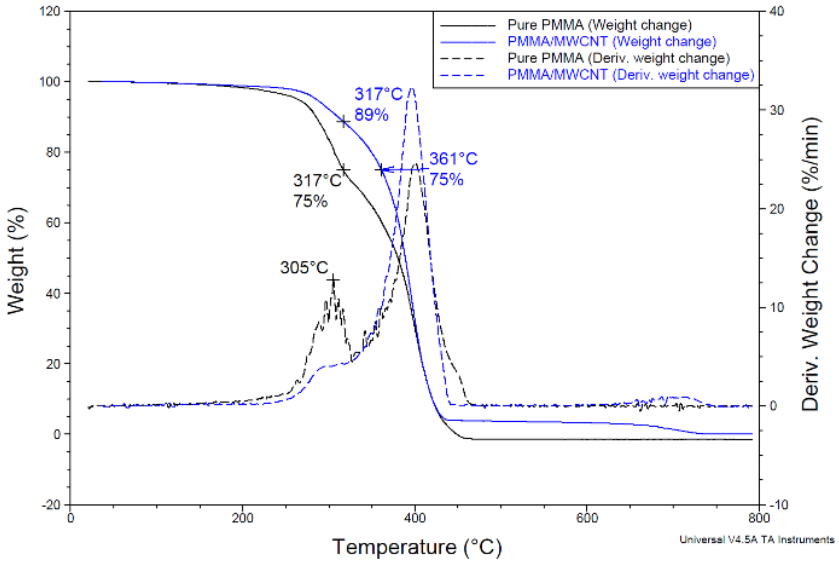

Figure 47: Thermal stability comparison between pure PMMA and PMMA/MWCNT samples.

Furthermore, it is also found that the PMMA/MWCNT presented better radiation resistance with regard to the thermal stability maintenance. Figure 48 shows a comparison between the TGA curves of both the non-irradiated and proton-irradiated samples, which have been irradiated with maximum radiation dose (up to 600 Gy). The TGA curve of irradiated PMMA/ MWCNT has no obvious change when it is compared with the TGA curve of the non-irradiated sample. In contrast, the 25% weight loss temperature of the pure PMMA shows a 15 °C decrease after being irradiated.

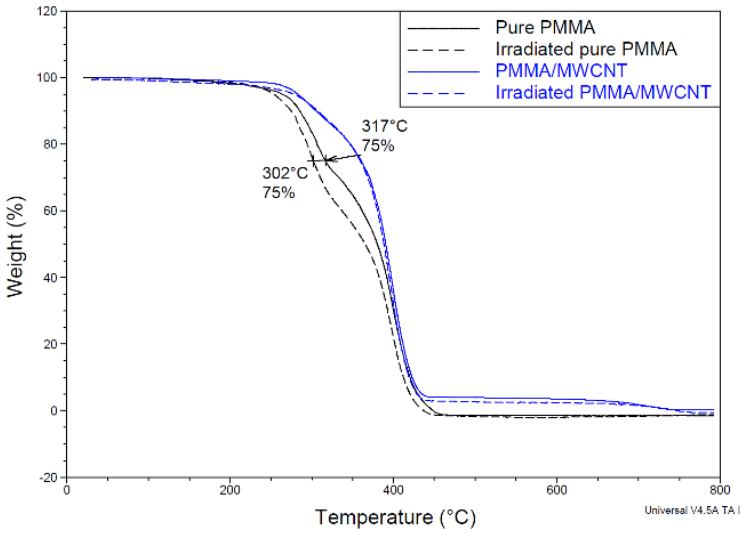

Figure 48: Thermal stability comparison among samples of both irradiated and non-irradiated pure PMMA and PMMA/MWCNT.

The tensile strength test results are given in Table 23. Before being irradiated, PMMA/MWCNT had a relatively lower tensile strength and elongation than those measured from pure PMMA. After irradiation, the tensile strength of pure PMMA maintained the same level with a 22.1% increase in elongation. While both the tensile strength and the elongation of the PMMA/MWCNT increased by 11.4% and 76.7%, respectively, compared with the non-irradiated PMMA/MWCNT.

Table 23: Tensile strength and elongation of both the non-irradiated and irradiated samples

Materials		**Tensile strength (MPa)**	**Elongation (%)**
Pure PMMA	Non-irradiated	19.01	0.68
	Irradiated	19.09	0.83
	Difference	<0.5%	22.1% increased
PMMA/MWCNT	Non-irradiated	17.83	0.43
	Irradiated	19.87	0.76
	Difference	11.4% increased	76.7% increased

Several studies have been reported on radiation-induced chain scission and/or crosslinking effects in polymers, and PMMA degradation was usually dominated by the chain scission effects [260, 266]. However, both these effects should decrease the elongation upon irradiation, in contrast to the elongations measured. Moreover, the delivered dose in the PMMA and PMMA/MWCNT samples during the whole radiation test was estimated to be not more than 600 Gy, while the reported radiation tolerance of PMMA was around 20 to 100 kGy [266]. Thus, the chain scission and crosslinking effects were less likely to have occurred in both the irradiated pure PMMA and PMMA/MWCNT samples.

Based on the assumption that there were no significant crosslinking and chain scission effects in PMMA, the increase in the tensile strength of the PMMA/MWCNT samples was considered to have been contributed by the radiation-induced crosslinking between the MWCNT outer shells; neighboring MWCNT inner shells; and the MWCNTs and polymer chains [267].

The tensile strength test results with regard to the elongation properties showed two phenomena: 1) pure PMMA presented higher elongation than its composite; 2) the proton radiation beam increased the elongation of both the pure PMMA and PMMA/MWCNT. Elongation of polymers can be related to the mobility of the polymer chain. Higher elongation of the polymer implies a higher mobility of the polymer chains. The addition of filler materials could decrease the chain mobility. Thus, the first phenomenon can result from the addition of MWCNTs as filler materials. While the second phenomenon is considered to be the result of entrapped air removal by the transmitted protons.

Air trapping happens very often during the melt-mixing process without vacuuming equipment. The trapped air in the form of microbubbles can be considered as the structural defects that limit the tensile strength. When high-energy protons transmitted the samples, the trapped air was ionized or escaped from the polymer matrix. Moreover, the effective cross-section area of the sample was also increased due to the elimination of the trapped air. As a result, the tensile strength of the samples increased after proton radiation. The increase in the effective cross-section area also increased the tensile strength of the irradiated samples.

In order to inspect for the existence of trapped air and the elimination of the trapped air after the proton test, thermal treatment was performed on both the non-irradiated and irradiated pure PMMA and PMMA/MWCNT samples. The pictures of the samples after thermal treatment are shown in Figure 49. Both the pure PMMA samples before and after proton radiation were transparent and no visible changes were observed under 25 °C before thermal treatment. Both the non- irradiated and irradiated PMMA samples were smooth-surface finished with no shape change. However, all the samples resulted in deformation of the samples along with trapped air in the form of bubbles within the samples: treated at temperatures of 130-160 °C and 170-180 °C.

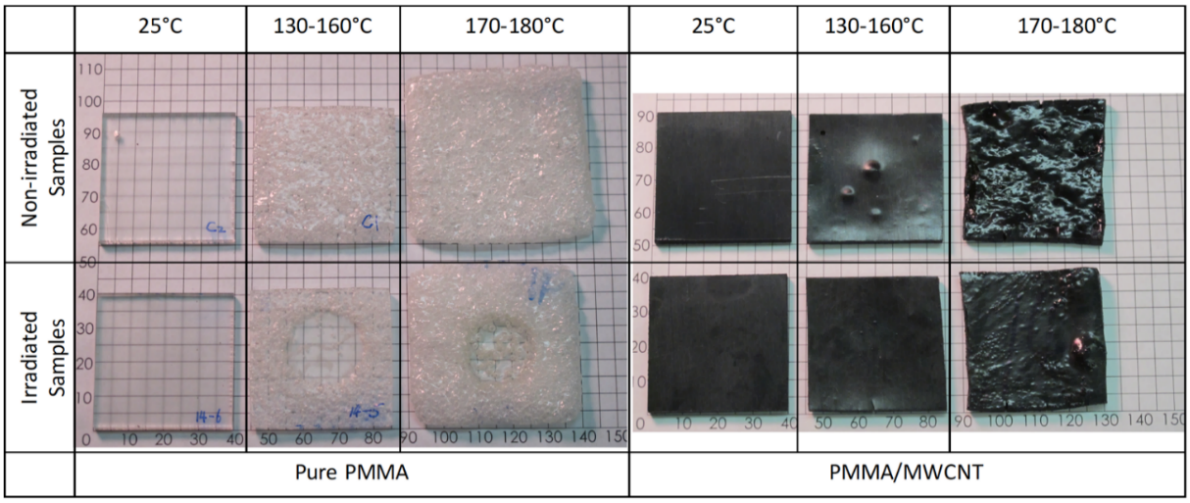

Figure 49: Samples before and after thermal treatment. The background grid has a unit size of 5 x 5 mm. The temperatures denote the temperature range in which the samples appeared.

For the non-irradiated pure PMMA, the samples showed uniformly distributed bubbles at 130 °C and the bubble density increased with time and temperature until 160 °C. When the temperature was increased to 170 °C, the speed of bubble generation became much faster and the samples appeared to expand in size. The size of the sample expanded to about 5.5 × 5.5 cm from its original size of 4 × 4 cm after the thermal treatment. On the other hand, the irradiated pure PMMA also

showed bubbles at 130 °C and an accelerated generation of bubbles at 170 °C. But in the irradiated portion in the center of the sample there appeared far less bubbles (less-bubble zone) compared to the edges of the samples. The final size after thermal expansion after the thermal treatment was also smaller than the non-irradiated pure PMMA, but still expanded to 5 × 5cm from its original size of 4 × 4cm.

In contrast, the PMMA/MWCNT of both irradiated and non-irradiated samples presented less expansion in size and less bubbles appeared. The irradiated PMMA/MWCNT did not show the less-bubble zone as the one presented by the irradiated pure PMMA. The irradiated PMMA/MWCNT showed even smaller deformation, less bubbles and almost no size change compared with the non-irradiated samples. From the results of the thermal treatment, it is firstly considered that this treatment proved the existence of trapped air in the samples as part of the fabrication process. Second, the trapped air ionized or escaped from the polymer matrix during the proton radiation tests. We therefore confirmed that the existence of trapped air generated a large volume of invisible voids and decreased the effective cross-sectional area, which induced low elongation and low tensile strength. Due to the elimination of the trapped air by proton radiation, structural defects were reduced along with an increase in the effective cross-sectional area. Thus, the irradiated samples showed higher tensile strength and larger elongation. However, if one considers the minor tensile strength difference of the pure PMMA before and after being irradiated, the effects of the trapped air mainly affect the elongation of the material.

One may speculate that the trapped air could be ionized by the incident high-energy protons resulting in the formation of oxygen and nitrogen ions within the air pocket trapped within the PMMA or PMMA/MWCNT matrix [268], which could further form nitric oxide upon interaction with the PMMA polymer chains [269]. The process of ionizing trapped air and forming nitric oxide, subsequently reduces the volume of the voids in the irradiated region which were then observed as the reduction in the air bubbles after the thermal cycling tests.

5.4 Conclusion

The radiation test showed that both the pure PMMA and PMMA/MWCNT have about 18%–19% more weight reduction than aluminum for proton shielding, although adding MWCNT showed no obvious effects for enhancing the weight efficiency. The secondary neutron results proved that PMMA generated 2.4%–4% less secondary neutrons than aluminum when exposed to high-energy

proton radiation, and more importantly, the addition of MWCNT to PMMA further reduced the neutron generation, which is 3.8%–5.1% less than aluminum.

According to the TGA and DSC analysis, the MWCNT loading of 3 wt% can enhance the thermal stability compared with the pure polymer. The loaded MWCNT interacted with the PMMA polymer matrix decreasing the mobility of the polymer chain and resulting in an increase in the glass transition temperature. When the PMMA/MWCNT samples were irradiated with protons, crosslinking might have been introduced among the MWCNT outer shells, between neighboring MWCNT inner shells, and between the MWCNT and polymer chains, which increased the tensile strength of the proton-irradiated PMMA/MWCNT samples.

Both the irradiated and non-irradiated pure PMMA and PMMA/MWCNT were thermally treated by heating them to 180 °C. The thermally treated samples became foam-like in appearance and demonstrated that air was trapped during the fabrication process forming invisible micro-voids, but the trapped air was eliminated when they were exposed to high- energy proton radiation. This was considered to be due to the ionization effect of air under high-energy proton radiation. Furthermore, the loading of the 3 wt% MWCNT also showed less visual deformation and material expansion under a high- temperature environment. We, therefore, conclude that MWCNT can be used as an effective filler material for polymer reinforcement, especially for radiation shielding applications in outer space missions.

Chapter 6 Electron Radiation Shielding Test

6.1 Introduction

The radiation environment in space consists of trapped radiation belts, cosmic rays, and solar energetic particles which is extremely hazardous to the health of astronauts and the electronics components in the spacecraft. Currently, most spaceflight missions are still around the Earth, such as the low-Earth-orbit (LEO), and the shielding provided by the Earth's magnetic field is capable of deflecting the major high-energy electron radiation that causes biomedical effects. However, future human space missions will extend to Moon base, a near-Earth object (NEO), habitations on Mars and even outer space. During such missions, electron radiation is one of the hazardous cosmic radiations, with energies up to tens of MeV, and capable of inducing carcinogenic effects in manned missions and/or serious damage to the spacecraft structural material and electronics components [270-274].

In order to maintain the normal operation of spacecraft electronics and to protect the health of astronauts in manned missions, relatively high atomic-number (Z) material, such as aluminum (Al), is typically used for radiation shielding owing to its high mechanical strength, low-cost and reliable fabrication process [275, 276]. However, its shielding effectiveness against high-energy electron radiation is limited by the lack in adequate shielding of the secondary bremsstrahlung photons that are produced by inelastic collisions of the electron radiation with the atomic nucleus of Al [277, 278]. Thus, to ensure the safety of personnel, more heavy material will be required for shielding, resulting in heavier payload and increasing mission cost and adversely affecting the mission duration due to more fuel consumption.

Alternatively, polymers which are usually composed of low-Z elements (such as hydrogen) with a weight advantage compared to metallic materials but capable of attenuating cosmic radiations without the massive production of secondary radiations, are potential materials for space radiation shielding applications [239]. Pure polymers may not be effective shielding materials against high energy electron radiation due to their low atomic number compounds when compared to the metal counterparts. However, the reinforcement of polymers with nanomaterials can result in improvements in the electron shielding properties of the nanocomposite materials compared to Al [238, 241, 265].

The utilization of nanomaterials is one of the current trends in the aerospace industry. In recent studies, some groups have reported advantages of carbon-based nanomaterials (such as carbon nanotubes) as shielding materials against ionizing radiations [279-284]. For example, the thermal conductivity of multi-walled carbon nanotubes (MWCNT) can be retained even after electron beam irradiation (energy of 1.25 MeV and flux of 2.3×10^{23} e/cm^2) at temperature of 373 K [281]. Other studies have reported negligible deformations of MWCNT including radiation induced formation of interstitial clusters and marginal shrinkage of inner carbon walls [281, 283]. By adding MWCNT into polymer matrix, compared to pure polymer, tensile strength of nanocomposite is able to be enhanced along with thermal stability due to formation of crosslinking sites and hindering effect under electron irradiation [285]. It indicates that MWCNT is able to stabilize thermal and mechanical properties of nanocomposite under electron beam irradiation. In addition, studies investigating the potential of polymer composites for photon radiation shielding has shown that bismuth oxide (Bi_2O_3) has promising ability as nanomaterial reinforcement of polymers [286-288] and has also been demonstrated as safe alternative to lead (Pb) which is extremely toxic [286, 287]. Regarding shielding gamma radiation with energies lower than 2 MeV, Bi_2O_3 provides predominate function in polyester resin composites with uniform distribution [288]. However, as of yet, it has not been reported to use Bi_2O_3 as high energy radiation absorption and/or shielding material for space applications.

Our group had previously reported that poly (methyl methacrylate) (PMMA) with three weight percentage (wt%) MWCNT nanocomposite (PMMA/MWCNT), compared to Al, was lighter, cost-effective, and a promising material to shield high energy proton radiations in outer space [284]. In this study, we hypothesize that a hybrid nanocomposite including MWCNTs and high-Z nanoparticles dispersed in PMMA (PMMA/MWCNT/Bi_2O_3) can effectively attenuate electron beams with energies of 9 to 20 MeV similar to those reported for outer space [274, 289]. The PMMA/MWCNT/Bi_2O_3 nanocomposite has been characterized using thermogravimetric Analysis (TGA), differential scanning calorimetry (DSC) and scanning electron microscope (SEM) and the attenuation properties under electron beams have been investigated. Advantages of PMMA/MWCNT/Bi_2O_3 nanocomposite have been discussed and compared with Al, pure PMMA and our previously developed PMMA/MWCNT nanocomposite.

6.2 Methods

PMMA with 2.1 wt% MWCNT and 30 wt% Bi_2O_3 nanocomposites (PMMA/MWCNT/Bi_2O_3) were fabricated, and its material properties such as thermal decomposition, glass transition temperature and dispersion were characterized. Pure PMMA, PMMA/MWCNT and aluminum were used as reference materials.

6.2.1 Fabrication

Research grade PMMA powders (Sigma-Aldrich, #182230), MWCNT (Nanostructured & Amorphous Materials, -COOH, 95+%, OD 10-20 nm) and Bi_2O_3 nanoparticles (Sigma-Aldrich, #202827) were used for the fabrication and tests. Melt mixer (Haake Rheocord 90) and hot press instrument were used for fabrication of pure PMMA, PMMA/MWCNT, and PMMA/MWCNT/Bi_2O_3 nanocomposite. PMMA powder (micron-sized particles) were heated and melted at 200°C in the mixer followed by addition of 3 wt% of MWCNT. Subsequently, 30 wt% of Bi_2O_3 nanoparticles was added to the molten mixture. PMMA samples were then loaded into the hot press at 180 °C and pressure of 1.6 MPa; the press is used for molding thermoplastics into solid squares 30 × 30 cm^2. As shown in Figure 50, pure PMMA, PMMA/MWCNT and PMMA/MWCNT/Bi_2O_3 were cut into 3.5 × 3.5 cm plates by laser cutter (VLS 2.30, Universal laser systems).

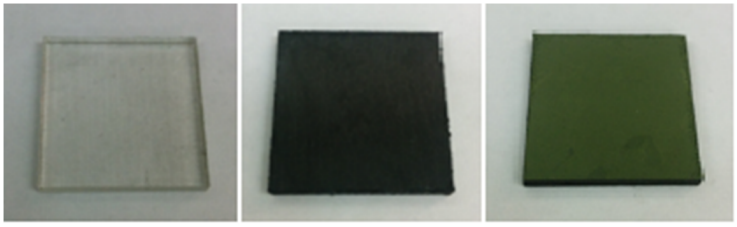

(a) (b) (c)

Figure 50: (a) Pure PMMA, (b) PMMA/MWCNT, (c) PMMA/MWCNT/Bi_2O_3

6.2.2 Characterization Studies

Pure PMMA, PMMA/MWCNT and PMMA/MWCNT/Bi_2O_3 samples were characterized with TGA, DSC and SEM. All those samples were measured before and after electron beam irradiation in order to determine radiation effects on the thermal properties and/or any visible morphological changes in the materials.

TGA apparatus was used to identify components and thermal degradation process of materials with programmed temperature. The test temperature was set as increasing from room temperature to 800 °C with ramp of 20 °C/min under nitrogen environment in TA instrument Q500. Weight of materials were monitored in real time to compare the thermal degradation as a function of increase in temperature.

DSC is an important method to measure the glass transition temperatures (Tg) of polymer materials. Samples were tested in a sealed chamber in TA Q2000 under 25 °C to 180 °C at ramp rate of 10 °C/minute followed by decreasing rate of 20 °C/minute from 180 °C to room temperature. Heat transition through samples over raising temperature can be plotted to analyze modified Tg in composite compared to pure polymer.

Moreover, SEM images were acquired using Zeiss Ultra plus SEM. Samples were coated with a thin layer of gold (20 nm) to improve image quality. Surface microstructure of nanocomposites were evaluated at a magnitude of 12kX.

6.2.3 Electron Beam Attenuation Test

Figure 51 shows the setup of the electron beam irradiation of the sample materials. All measurements were done using a Clinac® 21EX System machine at the Grand River Regional Cancer Centre (Kitchener, ON, Canada). 100 monitor unit (MU) at a dose rate of 1000 MU/min was delivered for this work. A 6×6 cm^2 electron cone applicator with 3 cm diameter lead cut-out insert was used for the electron beam irradiation. Pure PMMA (reference material), PMMA/MWCNT (nanocomposite), PMMA/MWCNT/Bi_2O_3 (nanocomposite) and Al (reference material) were used to study the electron beam attenuation characteristics for electron beam energies of 9, 12, 16 and 20 MeV. The samples were placed at a distance of 110 cm from the electron radiation source. An ionization chamber (Farmer chamber), positioned underneath the sample, was used to measure the transmitted electrons through the sample. An ion chamber reading without the sample in place was first taken as a baseline reading. For purposes of this study, the ion chamber reading can be denoted as C_t when a sample is placed between the source and the chamber reading, C_0 when there is no sample in place. Then the relative electron attenuation (%) of the samples can be calculated as: $\eta = ((C_0-C_t)/C_0) \times 100$. The attenuation results are plotted as a function of areal density (A) derived from the product of mass density (ρ) and thickness (t) of the material ($A = \rho \times t$). Comparison between nanocomposites and reference materials were made to determine the radiation shielding advantages in nanocomposites.

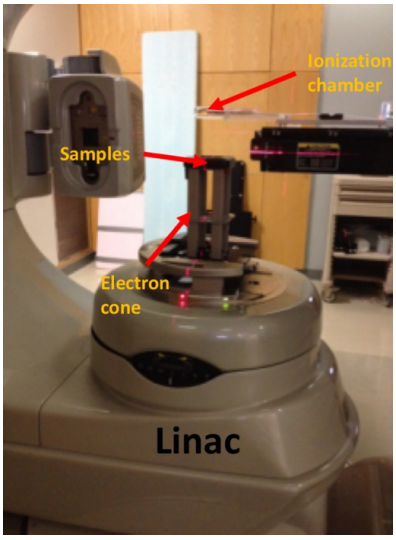

Figure 51: Electron irradiation test setup

6.3 Results and discussion

Characterization results of materials are analyzed in this section. Electron beam test results show the potential capability of electron shielding and thermal enhancement of PMMA/MWCNT/Bi_2O_3 nanocomposite compared to reference materials.

6.3.1 Material characterization

The TGA results is shown in Figure 52. The first 2% weight loss of all materials can be considered as removal of contaminants during the degassing process followed by a plateau and subsequently starts to drop around 210 °C with increasing temperature. Based on the TGA data, 98% of total weight of PMMA/MWCNT is left at 237 °C, the starting temperature for material decomposition (initial decomposition temperature) which is 27 °C higher than that of pure PMMA (210°C). Moreover, the nanocomposite with Bi_2O_3 nanoparticles showed significant thermal stability improvement such that the initial decomposition temperature (278 °C) is about 68 °C (about 32.4%) higher than that of the pure PMMA. This is caused by the homogenously distributed MWCNT in polymer matrix restrained the degradation of PMMA chains during pyrolysis [290-292]. Compared to the non-irradiated samples, the initial decomposition temperature of electron beam irradiated samples (PMMA: 211°C, PMMA/MWCNT: 235°C, PMMA/MWCNT/Bi_2O_3: 276°C) differed by only less than 1%, which suggests that irradiated samples (PMMA: 210 °C, PMMA/MWCNT: 237 °C, PMMA/MWCNT/Bi_2O_3: 278 °C) maintain their thermal properties.

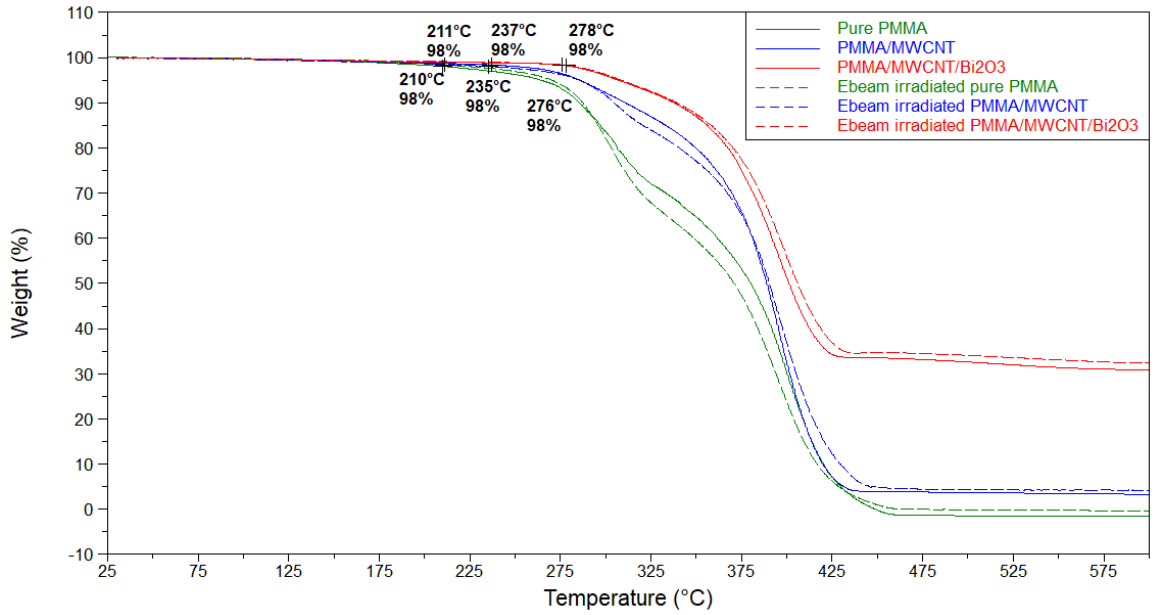

Figure 52: TGA data of samples before and after electron radiation

On the other hand, about 33 wt% and 3 wt% of residual material of PMMA/MWCNT/Bi_2O_3 and PMMA/MWCNT, respectively, remained when temperature increased above 425°C. For pure PMMA, almost no residual was found at temperatures >425°C; the polymer was totally decomposed. Since the nanomaterials (Bi_2O_3 and MWCNT) are highly heat resistant, the residual weight percentages (33 wt% and 3 wt%) precisely indicate the original weight percentages of MWCNT and Bi_2O_3 in PMMA/MWCNT/Bi_2O_3 and MWCNTs in PMMA/MWCNT.

DSC data of both electron-beam irradiated and non-irradiated materials are shown in Figure 53. Both nanomaterials, MWCNT and Bi_2O_3, largely improve the *Tg* of pure PMMA. PMMA/MWCNT/Bi_2O_3 nanocomposite has considerably higher *Tg*: 13.3% and 3.5% than pure PMMA and PMMA/MWCNT, respectively. It is evident that the nano-fillers can potentially enhance the working temperature range of the nanocomposites making them ideal candidates for space applications. For example, the radiation shielding components, used in space missions in the low earth orbit, require a wide range of working temperatures (up to 100 °C) in order to avoid potential risks of thermal degradation due to the harsh environment [293]. Post radiation, *Tg* of PMMA and nanocomposites dropped less than 1 °C. This minor change may be caused by minimal/low interaction of the high-energy electrons with the samples such that the thermal properties remained unaltered [294]. In conclusion, these results indicate that the polymer nanocomposite with Bi_2O_3 nanoparticles is a promising shielding material for space applications.

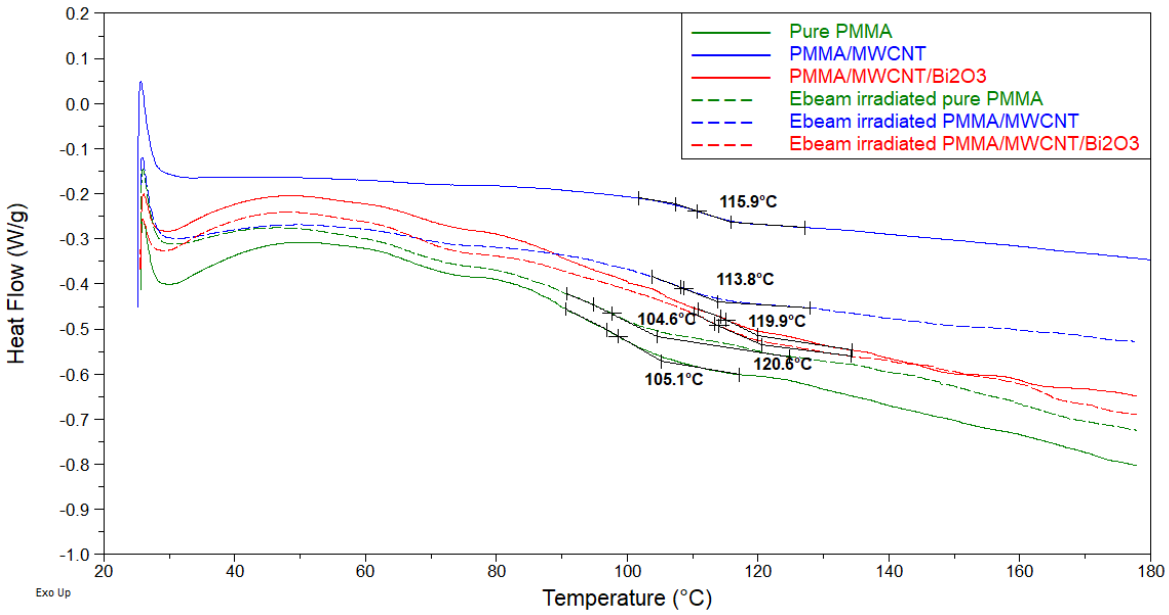

Figure 53: DSC data of samples before and after electron radiation

SEM images of PMMA/MWCNT/Bi_2O_3 before and after electron beam irradiation are shown in Fig 5. The uniformly distributed spherical particles, in Figure 54, represent Bi_2O_3 nanoparticles surrounded by bright web-like structure of the MWCNTs. No sign of aggregation of MWCNT is observed in all images, demonstrating uniform dispersion of nanomaterials in the PMMA matrix. The SEM images of PMMA/MWCNT/Bi_2O_3 cross-sections before and after electron beam irradiation show no obvious deformations including radiation induced polymer matrix degradation that can lead to exposure and aggregation of MWCNT [225, 295].

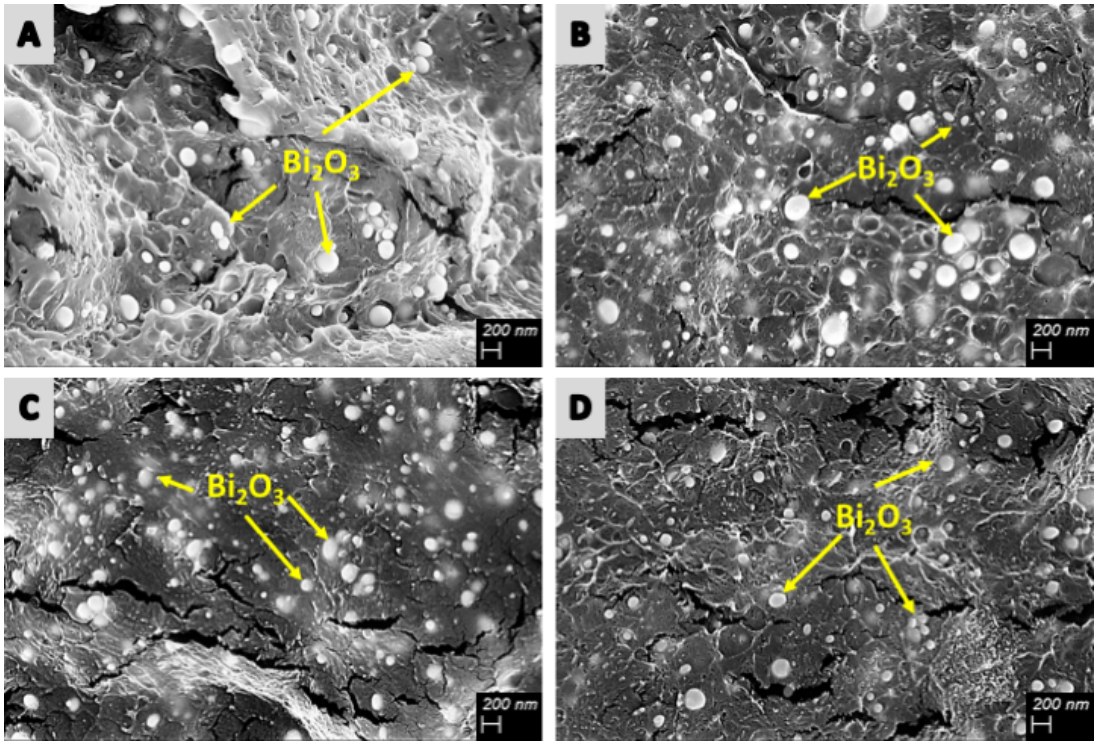

Figure 54: SEM images of PMMA/MWCNT/Bi_2O_3 nanocomposites before (A and C) and after (B and D) e-beam irradiation test.

6.3.2 Electron Beam Attenuation Test

Transmission characteristics for five different areal densities (0.58 g/cm^2, 1.00 g/cm^2, 1.44 g/cm^2, 3.60 g/cm^2, and 6.43 g/cm^2) of each sample irradiated at four different electron beam energies (9, 12, 16 and 20 MeV) were measured. The percentage attenuation characteristics for each of the four energies are shown in Figure 55. As the electron beam energy increases from 9 to 20 MeV, more materials (higher areal density) for each sample were required to attenuate the electron beam. The overall trend of materials was found to be similar for all energies. However, the PMMA/MWCNT/Bi_2O_3 nanocomposite shows better shielding properties than the other materials for any given areal density. That is for a given amount of material, the nanocomposite shielded better than Al, and require less material comparison to the Al to achieve equivalent electron shielding performance.

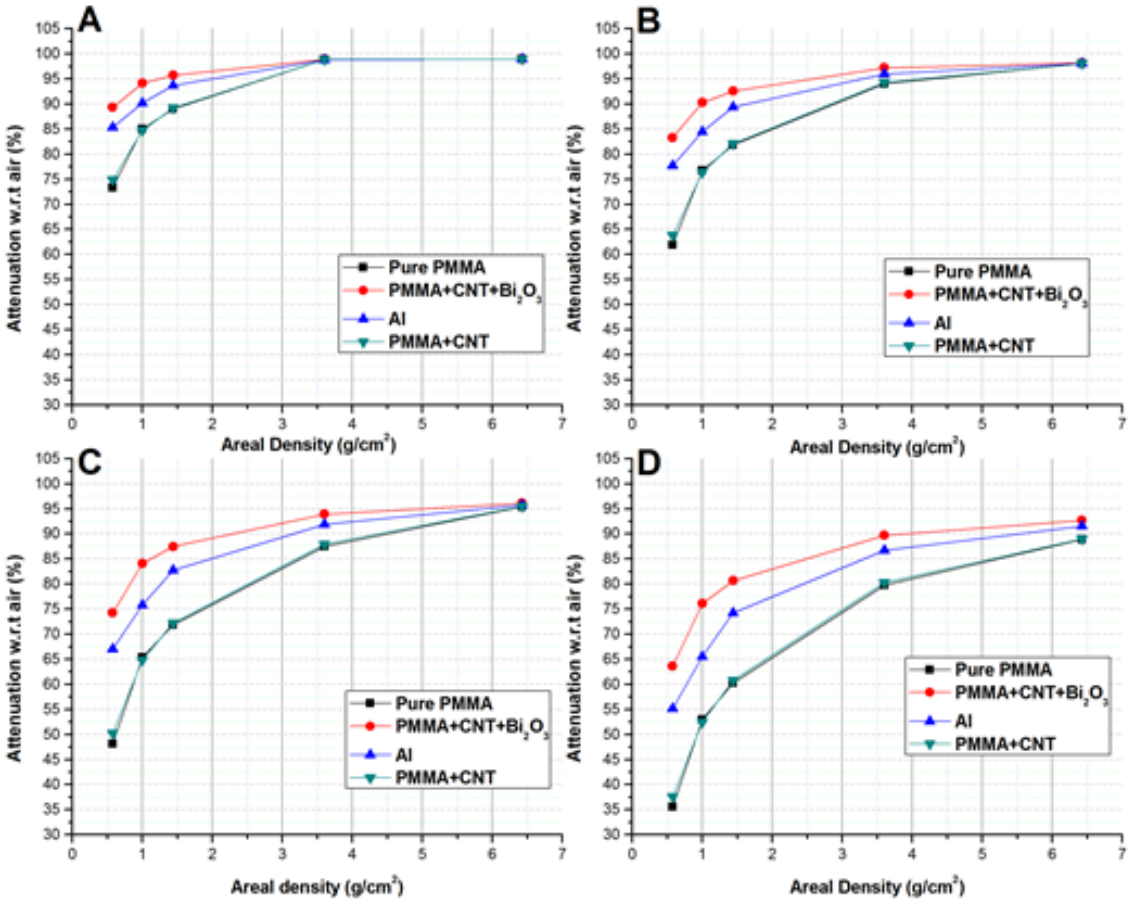

Figure 55: Percentage attenuation of all materials at (A) 9 MeV, (B) 12 MeV, (C) 16 MeV, and (D) 20 MeV

For each of the areal densities, the percentage attenuation behavior was plotted as a function of increasing energy (Figure 56). For all areal densities, the PMMA/MWCNT/Bi_2O_3 nanocomposite showed advantages over Al. At areal densities <3.6 g/cm^2 (Figure 56 A, B and C), compared to areal density of 3.6 and 6.43 g/cm^2, PMMA/MWCNT/Bi_2O_3 showed higher attenuation advantage (>= 5%) over Al at all the energies used in this study. Regarding areal density of 6.43 g/cm^2, PMMA/MWCNT/Bi_2O_3 nanocomposite shows attenuation advantages at higher electron beam energies (16 and 20 MeV). At lower energies (9 and 12 MeV), all materials reach the same attenuation characteristics.

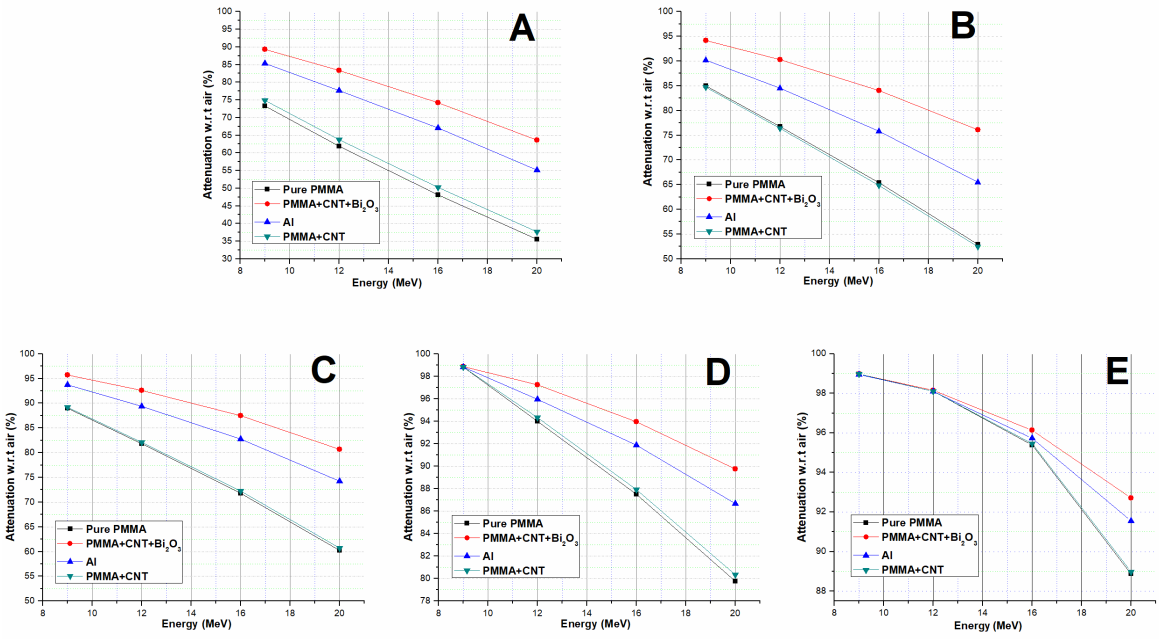

Figure 56: Percentage Attenuation as a function of energy at areal density of (A) 0.58 g/cm^2, (B) 1.00 g/cm^2, (C) 1.44 g/cm^2, (D) 3.60 g/cm^2 and (E) 6.43 g/cm^2

Higher resolution of electron attenuation of all materials at 9 MeV electron beam has been carried out to precisely investigate electron shielding mechanism. The percentage attenuation characteristics of all the materials using 9 MeV electron beam irradiation are shown in Figure 57 as a function of the material areal density. The areal density is indicative of the weight required for each of the materials. The percentage attenuation characteristic of PMMA/MWCNT nanocomposite is similar to the control sample (PMMA). However, at areal densities less than 1 g/cm^2, there seem to be relatively slight weight-advantage compared to the control samples. Apparently, the PMMA/MWCNT/Bi_2O_3 nanocomposite shows higher attenuation of electron beam compared to Al at lower areal densities. In other words, for the same percentage attenuation, a lighter PMMA/MWCNT/Bi_2O_3 nanocomposite will be required compared to Al for electron beam exposures of 9 MeV. For example, at 94% attenuation under 9 MeV electron beam, the PMMA/MWCNT/Bi_2O_3 nanocomposite was about 33.33% lighter than Al. Of all the materials, the PMMA/MWCNT/Bi_2O_3 nanocomposite was found to be the lightest for given exposure.

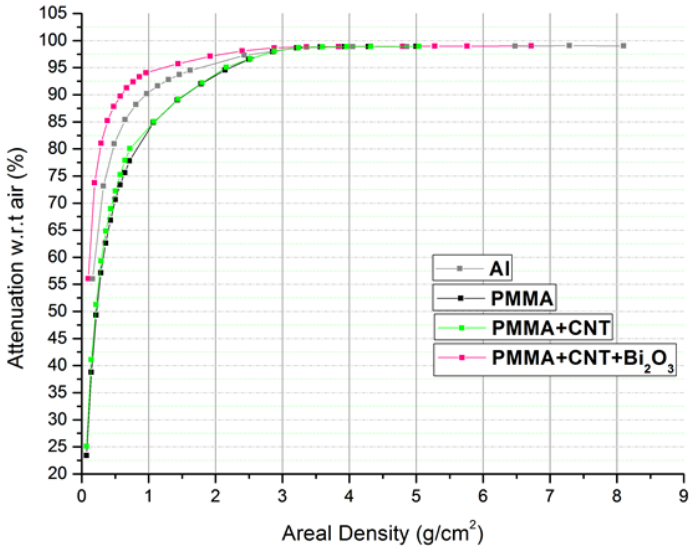

Figure 57: Percentage attenuation of all materials at 9 MeV

However, clearly, electron radiation cannot be 100% attenuated due to secondary radiations, such as bremsstrahlung photons and Auger electrons, generated by the interactions between instant electron beam and shielding materials and other components in setup [241]. For instance, under electron radiation with energy of 9 MeV, maximum electron attenuation of 98% for all shielding materials was approached at areal density of ~3.3 g/cm^2 which is denoted as saturated point of areal density (as shown in Figure 57). As a result, adding thickness of shielding materials after saturated point will not improve attenuation percentage. Besides, continuous slowing down approximation (CSDA) range of Al and PMMA (5.33 and 4.67 g/cm^2 at 9 MeV electron beam respectively) suggests, after 3.6 g/cm^2, few existing instant electrons may contribute the transmitted radiations [132].

The attenuation characteristics of all the materials as a function of different areal densities and energies shows that the PMMA/MWCNT/Bi_2O_3 nanocomposite would be much lighter material than Al for electron radiation shielding (as illustrated in Table 24 and Table 25). At electron beam attenuation of 90%, the nanocomposite was found to have at least 27% or higher weight advantage in comparison to that of Al for all energies (see Table 24). The shielding characteristics (in percentage attenuation w.r.t air) of the nanocomposite (PMMA/MWCNT/Bi_2O_3) was found to be better than Al for all energies, especially at lower areal densities.

Table 24: Weight advantage with respect to Al for beam attenuation of 90% for all energies

Energy (MeV)	Weight advantage w.r.t Al at 90% e-beam attenuation	
	Areal density advantages of nanocomposite compared to Al (g/cm^2)	Percentage weight reduction (%)
9	0.38	38.30
12	0.66	40.00
16	0.87	27.62
20	1.66	30.02

Table 25: Percentage attenuation calculated at different areal densities for each electron beam energy.

Areal Density (g/cm^2)	Material	9 MeV (%)	12 MeV (%)	16 MeV (%)	20 MeV (%)
0.57	Nanocomposite	89.33	83.31	74.25	63.62
	Al	85.35	77.69	67.04	55.18
1.00	Nanocomposite	94.13	90.29	84.08	76.08
	Al	90.15	84.47	75.84	65.52
1.44	Nanocomposite	95.75	92.58	87.47	80.66
	Al	93.71	89.36	82.75	74.22
3.60	Nanocomposite	98.88	97.22	93.94	89.73
	Al	98.81	95.94	91.88	86.67
6.43	Nanocomposite	98.99	98.14	96.14	92.70
	Al	98.96	98.09	95.73	91.55

As the result of this work has shown and discussed, for all electron energies (9 to 20 MeV), the attenuation characteristics as a function of areal density for all materials reaches a saturated point at higher areal densities, such as 3.3 g/cm^2 for 9 MeV electron beam.

6.4 Conclusion

In space applications, Al constructed units used for protecting radiation-sensitive components from charged space radiations, such as electrons, will open the way for innovative material with light-weight advantage. The present research has demonstrated that Bi_2O_3 added nanocomposite possesses greater than 27% weight advantage compared to Al under electron beam radiation energies ranging from 9 to 20 MeV at 90% electron attenuation. The weight advantage of nanocomposite is showing higher value (38.3% and 40%) at lower electron beam energies (9 and 12 MeV); however, it is found that nanocomposite has no weight advantage if areal density of shielding materials reaches saturated point. For instance, all materials with areal density greater than 3.3 g/cm^2 can achieve the same 98% electron attenuation under 9 MeV electron beam energy. Besides that, for all electron beam energies, PMMA/MWCNT/Bi_2O_3 nanocomposite contributes electron attenuation advantage over Al and higher advantage is observed while less material mass is required for attenuation by electron beam. Based on characterization results, thermal stability

(TGA and DSC) of PMMA is considerably improved by addition of uniformly dispersed MWCNT and Bi_2O_3 nanoparticles. This work has indicated that PMMA/MWCNT/Bi_2O_3 nanocomposite is promising in aerospace applications. Associating with our previous study, a multilayer design with the two nanocomposites (PMMA/MWCNT and PMMA/MWCNT/Bi_2O_3) can potentially be developed to shield both high energy proton and electron radiations in future research.

Chapter 7 Multifunctional Structure for Space Radiation Shielding

7.1 Introduction

Space radiation shielding technology has been developed for several decades in human history and opened great opportunities to explore our extensive universe. In recent year, numerous space applications vastly sprout out around the world, especially for long term journey to Mars. Obviously, the long journey will require more astronauts, payloads and space radiation shield on spacecraft in the future. Conventional space radiation shielding materials, such as aluminum, HDPE and water, can barely support future missions due to low ratio of shielding effectiveness and cost. One efficient method to reduce the cost is applying light-weight materials to replace heavily equipped radiation shield.

Distinct researches have been conducted to investigate applicable light-weight structures in space mission [296]. Xindi Li's group has reported that polyethylene associated with Al can accomplish 6% weight reduction compared to pure Al when shielding GCR [23]. Based on a research from NASA, hydrogen (5wt%) crafted boron nitride nanotube itself has about 33% weight reduction over Al under simulated GCR environment [297]. However, the unstable hydrogen in nanotube and affected mechanical strength of nanostructure will limit its application [298]. Other elements such as carbon have been investigated when exposed to GCR [299]. Even though, it is still a challenge to form a structural radiation shielding part to replace conventional Al structure on spacecraft.

As discussed in some studies, multilayer design for space radiation shielding shows a popular trend in modern space missions [299-301]. This is the result of complex and extreme hazardous space radiation environment that can hardly be shielded by a single material. In the multilayer design, each part of multilayers contributes specific function to protect payloads on spacecraft. Meanwhile, each layer should be able to associate with other components. As a result, this is concluded as an approach to a multifunctional structure with excellent radiation shielding, thermal and mechanical properties for space application.

CFRP honeycomb panel is commonly used structural components in space applications due to its high mechanical strength and thermal properties. However, its physical properties are highly dependent on the carbon fiber and epoxy embedded in. Under harmful high energy space radiations, carbon fibre in the structure can merely survive, which will result in significant failure in space missions. Based on our previous study on proton radiation shielding test, hydrogen rich polymer PMMA based nanocomposite PMMA/3wt%MWCNT has achieved about 18% weight reduction

(radiation shielding effectiveness) and 3-5% less secondary neutrons over reference material (Al) under the same proton radiation setup. In addition of 30 wt% Bi_2O_3 nanoparticles, compared to Al, the results indicate that PMMA/MWCNT/Bi_2O_3 nanocomposite possesses 27%-40% weight advantage at 90% electron beam attenuation. The advantage of nanocomposite varies from different electron energies. Besides, the saturated attenuation points were introduced, which can be reached when areal densities increase until minor electron beam attenuation advantage achieved for all materials.

Adopting radiation shielding advantages of the nanocomposite onto CFRP honeycomb structure will largely improve overall properties of the structure. Therefore, a polymer-based multifunctional nanocomposite coated CFRP honeycomb structure has been developed in this research. In this chapter, bulk fabrication processes were tested and evaluated followed by optimization process of nanocomposite based on previous studies and simulation results. At the end, a well-designed final prototype has been illustrated.

7.2 Improved Fabrication Process

PMMA is a well-developed polymeric material and it has been used extensively for space applications melt mixing method which has been elaborately described in studies [175]. Two of the efficient methods using twin screw extruder and double armed planetary mixer have been illustrated in section 3.1.2 and 3.1.3. In our previous studies, melt mixing process was used to produce PMMA, PMMA/MWCNT and PMMA/MWCNT/Bi_2O_3 nanocomposites. To fabricate adequate amount of nanocomposite as radiation shielding layer on CFRP structure, the scaled-up industrial methods are analyzed in this section. Characterization were carried out to evaluate samples quality produced by the methods, and the outstanding equipment was selected for further bulk fabrication.

7.2.1 Fabrication Methods

(i) Twin-screw Extruder

As introduced in section 3.1.2, extruder is an efficient way for bulk fabrication of polymer-based nanocomposites. The set up parameters on the twin screw extruder for our samples are shown in Table 11 [307]. In Figure 58, zone 1 is closest to feeding area, and zone 5 is the end of the mixing zones. To avoid any accidental blocking polymers at the beginning, the temperature of zone 1 (170 °C) should be close to the melting point of our polymer. On the other hand, according to the thermogravimetric analysis of PMMA (Figure 37), serious degradation would happen when the

temperature reaches over 225 °C, thus the maximum mixing temperature was set as 200 °C to obtain fluid viscosity in zone 2-4.

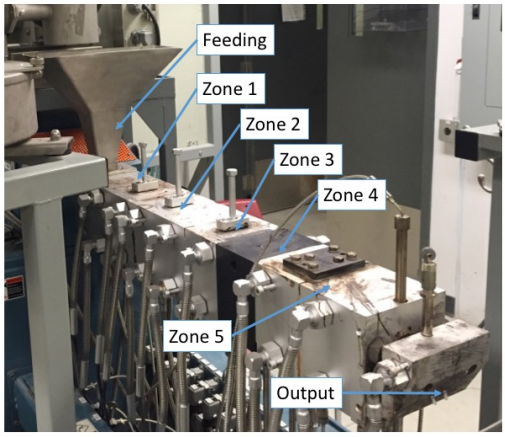

Figure 58: Coperion ZSK 25mm Extruder

(ii) Double Planetary Mixer

PMMA is a thermoplastic polymer which can be melted to fluid above 160 ºC in the double planetary mixer. Interacted with nanomaterial, MWCNT, polymer chains can be open to form nanocomposite with sufficient mixing time and speed. A vacuum system will effectively erase the entrapped air or contaminant in the melted nanocomposite during mixing process. The mixing speed and time for nanocomposite are variable, and the ideal recipe was tested and finalized [308, 309]:

Step 1 Feed a quantity of PMMA powders with certain percentage of MWCNT into the tank
Step 2 Heat up the tank to 220 ºC
Step 3 Start up the agitators with sufficient rotation speeds (8 Hz)
Step 4 Apply vacuum during mixing
Step 5 Keep mixing process for 2 hours
Step 6 Unload the well mixed nanocomposite

7.2.2 Characterization and Results

To evaluate dispersion quality of nanofillers in nanocomposites, tensile strength test was applied to measure tensile modulus followed by thermal conductivity test and other characterization. Testing results of pure PMMA and PMMA with 3wt% MWCNT fabricated by the two different methods have been analyzed, and the method produces higher quality samples is selected for bulk fabrication.

(i) Tensile Strength Test

Tensile strength test was applied on nanocomposite made by both fabrication methods. As shown in Figure 59, compared to extruded samples, tensile modulus of melt mixer samples, PMMA and PMMA/3wt%WMCNT is showing about 100% and 134% advantage respectively, which indicates better resistance to stress deformation. The lower modulus of materials fabricated by twin-screw extruder may be caused by high shear force in extruder during fabrication process. The high shear force method is helpful to efficiently disperse nanofillers into polymers; however, it induces crosslink breakage and chain scission among polymer chains [310-312]. On the other hand, less uniformity of nanocomposite may be ascribed to aggregation of nanofillers [313]. Moreover, while increasing shear rate in twin-screw extruder, entrapped air and thermal degradation, which results in decrease in mechanical strength, may form and occur in composites [314].

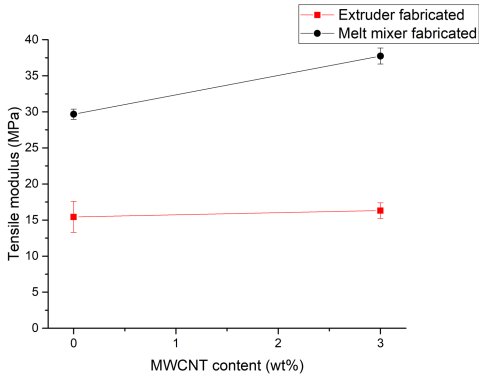

Figure 59: Tensile modulus of PMMA and PMMA/3wt%MWCNT fabricated by two methods

(ii) Thermal Conductivity

The apparatus for thermal conductivity measurement was assembled by Microelectronics Heat Transfer Laboratory from University of Waterloo followed by ASTM D5470-95 standard (section 3.2.6). The results of extruded PMMA and PMMA with 3wt% MWCNTs nanocomposite have been listed in Table 26. Compared to melt mixer fabricated samples, thermal conductivity of extruded nanocomposite has around 40% decrease, but thermal conductivity of pure PMMA has about 30% improvement. Jinho Hong et al. reported that higher thermal conductivity in nanocomposite indicates better dispersion quality of MWCNT [315]. Using melt mixer has achieved 357.8% improvement compared to PMMA, but only 104.5% for extruded nanocomposite.

Table 26: Thermal Conductivity Results

	Extruder fabricated		Melt mixer fabricated	
Materials	**PMMA**	**PMMA/MWCNT (3wt%)**	**PMMA**	**PMMA/MWCNT (3wt%)**
Thermal conductivity (W/K-m)	0.178	0.364	0.137	0.627
Improvement compared to PMMA	--	104.5%	--	357.8%

(iii) TGA

Figure 60 shows weight percentage changes of the extruder fabricated PMMA (blue) and PMMA with 3wt% MWCNTs (blue dash). Complete thermal degradation of pure PMMA occurred at 460 °C and with the incorporation of 3wt% MWCNT, the complete degradation temperature was found to be almost the same as pure PMMA. Moreover, the degradation beginning point is 225 °C for pure PMMA, but it is about 250 °C for nanocomposites, which achieved about 11% improvement. Besides, the weight reduction of pure PMMA progress faster than PMMA/MWCNT at temperature below 375 °C. Compared to melt mixer fabricated PMMA with 3wt% MWCNT (green dash), extruded nanocomposite (blue dash) is slightly more stable below 250 °C. However, it degrades dramatically above 280 °C. Extruded PMMA/MWCNT completes degradation at 460 °C, which is about 20 °C higher than melt mixer fabricated nanocomposite. Samples produced from both fabrication methods have not shown significant diversity.

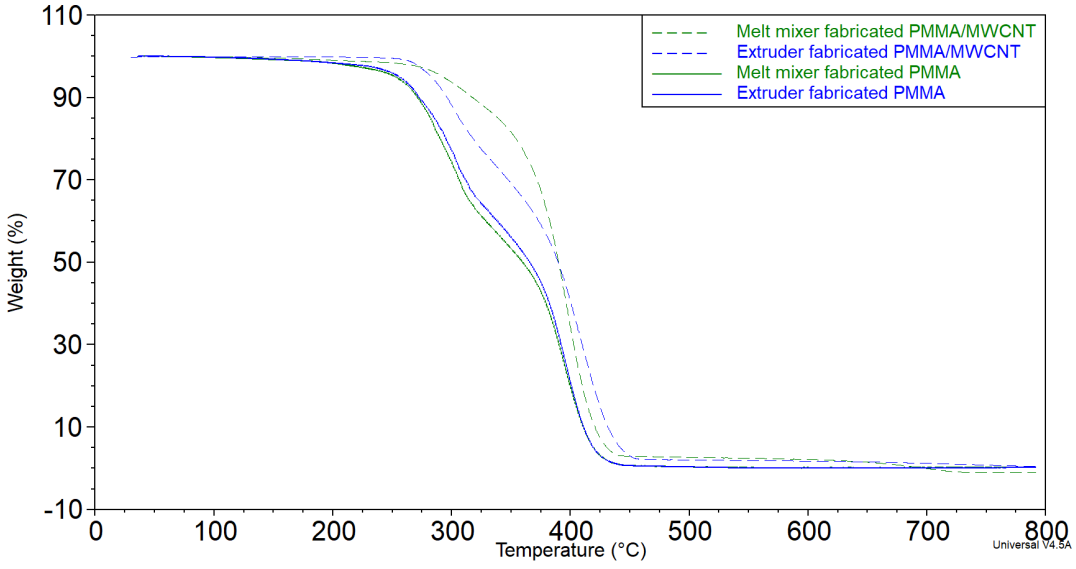

Figure 60: Weight loss rate in TGA between extruded PMMA and nanocomposite

(iv) FTIR

FTIR was used to investigate interactions between MWCNT and PMMA polymer chain in nanocomposites made by the two fabrication processes. As shown in Figure 61 left, both nanocomposites have shown intensity changes in the range of 500 to 1500 cm^{-1} results in the formation the linkages between carbon and PMMA. Around 987 and 750 cm^{-1}, increased density with respect to both nanocomposites has shown additional C atoms in PMMA polymer chain [167, 316]. To further evaluate the bonds in PMMA/MWCNT nanocomposites, samples were repeatedly washed by dichloromethane in ultracentrifuge (150,000 RPM). The precipitation was extracted for FTIR test. Plotted in Figure 61, rather than extruder fabricated samples, melt mixer made nanocomposite still possesses peaks of PMMA, such as 1730 cm^{-1} [317-319]. This indicates stronger interactions between PMMA and MWCNT functional groups detected in the samples.

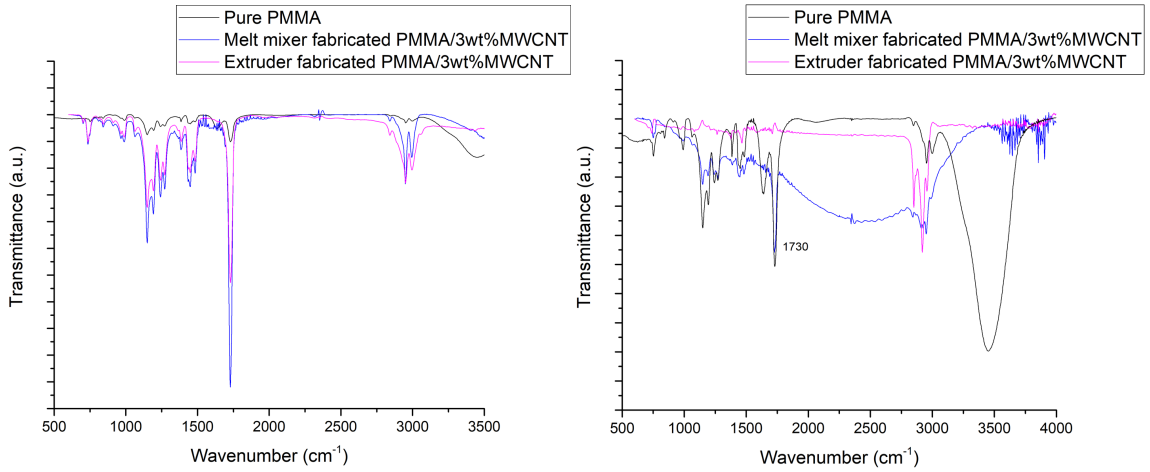

Figure 61: FTIR of samples from the two fabrication processes (left) and repeatedly washed samples and pure PMMA (right)

7.2.3 Summary

PMMA, and its nanocomposite were fabricated, characterized and analyzed to compare the two fabrication methods (twin-screw extruder and double planetary mixer). The conclusions have been pointed below:

- Tensile modulus of the planetary mixer made PMMA/MWCNT showed ~134% advantages compared to the samples fabricated using extruder which implies some inter polymer chain and cross-linking broken after high sheer force extrusion.

- Thermal conductivity of melt mixer fabricated PMMA/MWCNT was found to be almost twice of extruded nanocomposite.
- Regarding the TGA results, PMMA/MWCNT nanocomposite has the same degradation starting at 250 °C as the that obtained from melt mixed sample, which means samples from both methods possess close upper limit of decomposition temperature.
- FTIR spectra of both fabricated nanocomposites have shown the same but more intense peaks representing to the specific function groups of pure PMMA. In addition, Samples from melt mixer illustrates residual PMMA after washed by solvent. In another word, a stronger interfacial bonding was found in PMMA/MWCNT nanocomposites fabricated from the melt mixer.

Therefore, because of the better performance on mechanical property, thermal conductivity and interaction between MWCNT and PMMA, double planetary mixer with vacuum system is ideal for bulk fabrication to produce multifunctional nanocomposite as radiation shielding layer in the further study.

7.3 Optimization of Multifunctional Nanocomposite

7.3.1 Thermal Expansion

Thermal properties of materials used in space applications matter drastically. Besides thermal conductivity and stability, thermal expansion of materials is another concern in space mission. The majority of solids with positive thermal expansion expands when heated due to the anharmonic nature of chemical bond potential [320]. Changes in shape or volume of materials occur in response to a change in temperature. This is the common phenomenon of thermal expansion [321]. In space applications, low thermal expansion materials are expected when they are exposed to a wide range of working temperature such as -100 to 130 °C since large-scale change on structure materials will cause significant deformation for jointing multilayer materials. De-bonding at interface occurs when large difference in coefficient of thermal expansion (CTE) of layered materials involved. This is caused by high thermal stress generated by the layered structures [322].

As listed in Table 27, aluminum, which is the mostly used material in space, has a linear coefficients of thermal expansion (CTE, α) around 2.2×10^{-5} cm/cm/°C at 20 °C [323]. In CFRP honeycomb panel, Al honeycomb can be well-bonded with CFRP sheets due to the similar CTE of the two materials. Regarding PMMA and CFRP, after cooling down of the bonding process, breaks and

cracks may spread all over the CFRP layer. This phenomenon was considered caused by the coefficients of thermal expansion (CTE, α) difference between polymer and CFRP, which brought about a bonding difficulty of the two layers.

Table 27: CTE of different materials [324]

CTE (10^{-5} cm-cm/°C)	
PMMA	6.0
MWCNT	-0.5
CFRP	0.3-3.6
Al	2.3

As listed in Table 27, compared to Al, PMMA has almost three times CTE of Al. Due to the current MWCNT loading is relatively low in PMMA/MWCNT nanocomposite, which has only 3wt% MWCNT, CTE of nanocomposite is relatively high compared to CFRP. While in carbon fiber dominated CFRP, it shows fiber direction linear CTE of 0.3 to 3.6 with different fibers and resins [325]. Directly adoption of our previously developed nanocomposites as radiation shielding layer bonding on CFRP surface has been conducted. Volume change of PMMA/MWCNT panel was predicted to occur after the temperature goes up and down during thermal cycling. Significant deformations of CFRP layers including extensive cracks/delamination was observed (Figure 62). As a result, CTE of nanocomposite needs to be reduced so that it is close to that of CFRP.

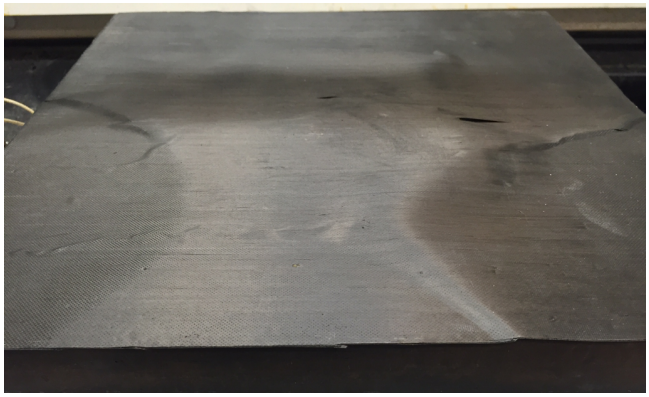

Figure 62: Delaminated CFRP surface caused by thermal stress between CFRP and PMMA after thermal cycling.

Without altering current material types, one practical way is increasing MWCNT weight percentage up to around 30% in PMMA/MWCNT nanocomposite to pull down the average CTE [26]. Wang et al. experimentally demonstrated that graphene oxide-filled composites could be tuned to low thermal expansion coefficient and improved thermal conductivity by adding graphene oxide weight

percentage [326]. Liu further proved that the CTE of SWCNT/PMMA composite would be even reduced below 1×10^{-5} cm-cm/°C if SWCNT content was increased over 15 wt% [26]. Moreover, it is reported PMMA with 15wt% MWCNT can reach CTE of 3.0×10^{-5} cm-cm/°C which is close to that of aluminum ($2.3\ 10^{-5}$ cm-cm/°C) and CFRP ($0.3\text{-}3.6\ 10^{-5}$ cm-cm/°C) [26]. K.P. Pramoda et al. have shown 23% reduction of CTE in PMMA nanocomposite by adding only 5wt% graphite nanocomposites due to large part of temperature dependent movement of polymer chain has been controlled by CNT [327]. To reduce CTE of nanocomposite and improve bonding properties, optimization was implemented to increase weight percentages of MWCNT from 5 to 20 wt% in nanocomposites.

7.3.2 Characterization and Results

(i) Radiation Shielding

Undoubtedly, radiation shielding effectiveness of nanocomposite will be affected by altering concentrations of MWCNT. According to the simulation results by SRIM, areal densities of Al, PMMA and PMMA/3wt%MWCNT were calculated to fully stop the proton energies between 30 and 90 MeV (Figure 63). Compared to our previous proton radiation shielding experiment, minor difference (about 2-3%) was found in SRIM for PMMA and PMMA/3wt%MWCNT. As a result, SRIM was applied to simulate areal densities of PMMA/MWCNT nanocomposites with various MWCNT weight percentages at relatively lower proton stopping energies (≤80MeV). As shown in Figure 64 and Table 28, relationship of areal density and proton stopping energy of all materials were simulated by SRIM. Compared to PMMA/3wt%MWCNT, PMMA with higher weight percentages of MWCNT is showing slightly less weight advantage over Al. Regarding PMMA/20wt%MWCNT, it is 20.9% less in weight compared to Al at proton energy of 100 MeV. The results indicate that PMMA/MWCNT nanocomposite is still a promising material for proton radiation shielding even loaded with higher percentages (increased to 20wt%) of MWCNT.

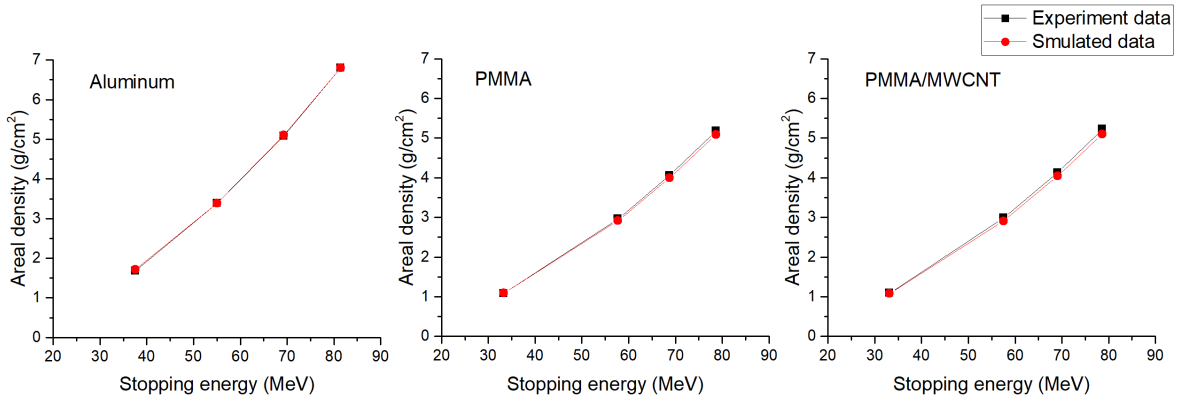

Figure 63: Comparison of SRIM and TRIUMF experimental results.

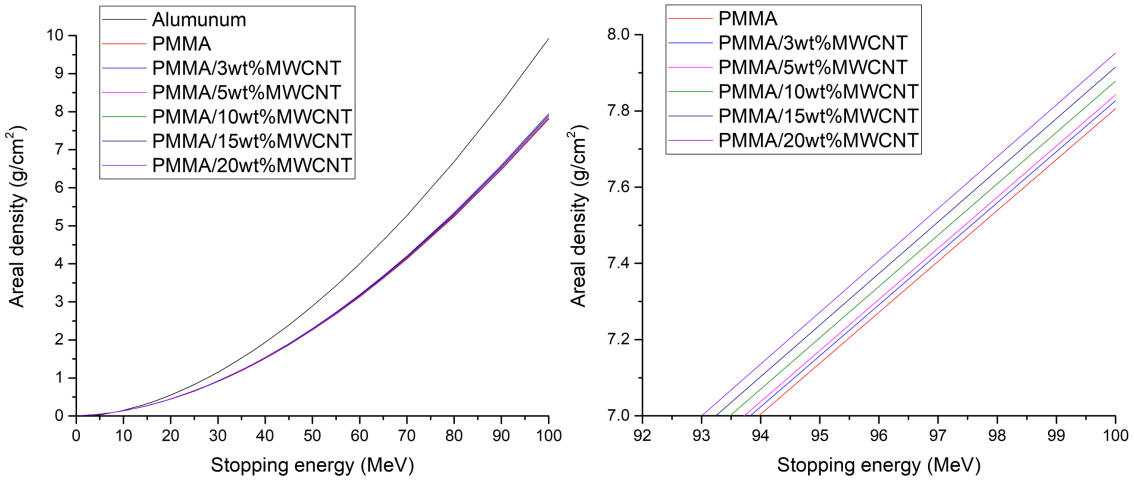

Figure 64: Relationship between areal densities of materials and proton stropping energy.

Table 28: Weight reduction of different percentages loaded PMMA/MWCNT nanocomposites compared to aluminum at proton energy of 100 MeV.

wt% of MWCNT	0	3	5	10	15	20
Density (g/cm^3)	1.194	1.204	1.216	1.244	1.273	1.303
Weight reduction compared to Al	22.4%	22.2%	22.0%	21.7%	21.3%	20.9%

(ii) DSC

Besides radiation shielding effectiveness, working temperature of nanocomposite is another crucial factor for coating layer design. Thermal expansion of materials will ascend dramatically when temperature goes above *Tg* of nanocomposite and increase linearly when below it. Therefore, *Tg* of nanocomposite is a critical point (working temperature). DSC is an important method to investigate

the glass transition temperatures of nanocomposites with increased MWCNT weight percentages (5-20wt%).

Figure 65 shows the results of all tested samples. All nanocomposites have achieved different improvement of glass transition temperature compared to pure PMMA (111 °C). PMMA/20wt%MWCNT has highest *Tg* of 117 °C similar to PMMA/15wt%MWCNT, which has shown 5.4% improvement. As shown in Figure 66, which plots the relationship between *Tg* and weight percentage of MWCNT in nanocomposite, no significant enhancement after increasing MWCNT content above 10wt% is observed. Some other studies illustrate the similar results may be caused by uneven distribution of MWCNT in nanocomposite [328, 329]. As discussed by Sophie Barrau, *Tg* of polymer composites increases linearly with wt% of fillers which follows Fox equation [330]. However, PMMA/20wt%MWCNT shows a threshold; therefore, PMMA/15wt%MWCNT is a proper nanocomposite with enhanced *Tg* and CTE.

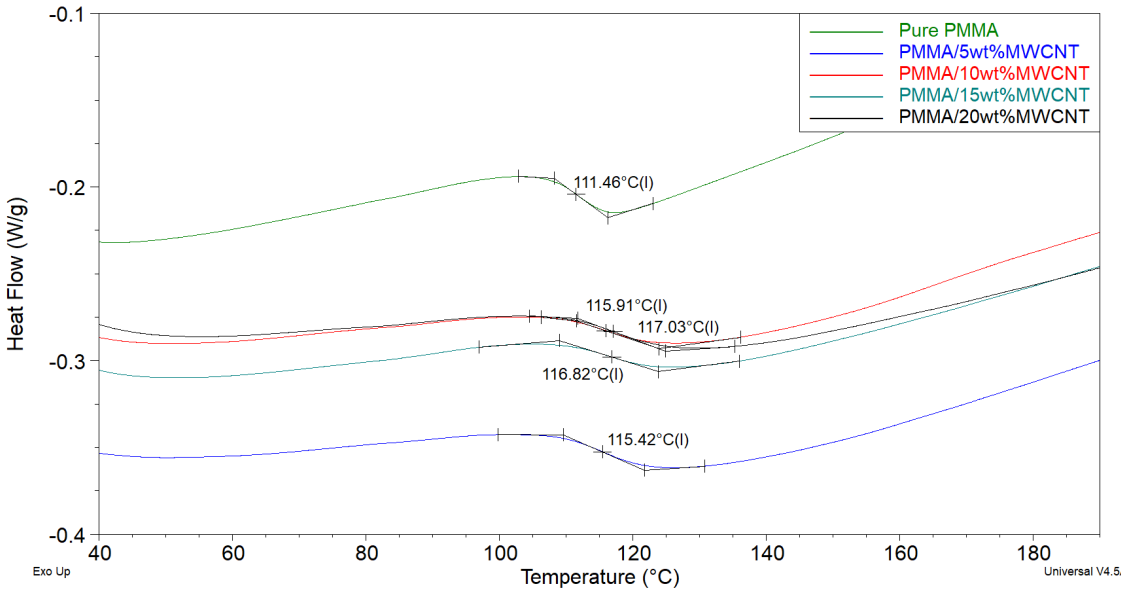

Figure 65: DSC Test on Nanocomposites.

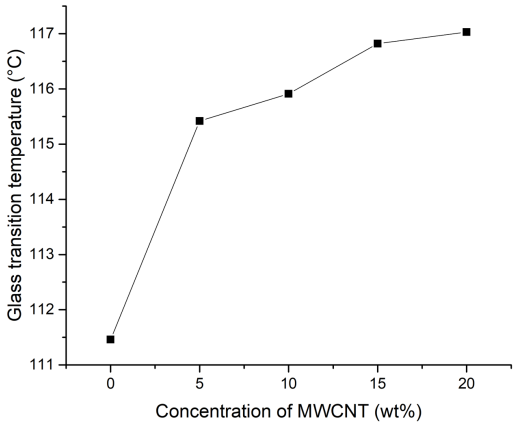

Figure 66: Increased *Tg* with various MWCNT weight percentages in PMMA matrix.

7.3.3 Summary

Increasing MWCNT weight percentage is an effective way to reduce coefficient of thermal expansion of PMMA based nanocomposite. According to the paper from Liu et al., thermal expansion rate can be reduced by increasing weight percentage of CNT in polymers [26]. The dimension change rate has been decreased to 0.5% at 130 ºC with 15wt% of CNT loaded nanocomposite which is similar to samples with 20 wt% CNT added sample. Regarding proton radiation shielding effectiveness and working temperature of nanocomposites, increasing weight percentages of MWCNT induces linearly descending shielding property and ascending *Tg* within PMMA nanocomposites. On the other hand, by increasing percentage of MWCNT in polymer matrix, thermal properties including thermal conductivity and stability of nanocomposites will be improved correspondingly. In conclusion, 15wt% is an optimal concentration for MWCNT in nanocomposite to contribute enhanced physical properties and radiation shielding effectiveness.

7.4 Radiation Shielding Layer Design

Based on the previous results, PMMA/15wt%MWCNT with reduced CTE, enhanced *Tg*, thermal conductivity and stability was carried out as multifunctional radiation shielding layer. CTE mismatches and other factors must be considered carefully to ensure steady multilayer structure. In this section, the nanocomposite was fabricated to be bonded on the surface of CFRP honeycomb penal followed by a thermal cycling test to evaluate the modified CTE of nanocomposite and the bonding strength. In Figure 67, one of SEM images of PMMA/15wt%MWCNT is illustrated. Due to the high concentration of MWCNT, it is showing conductive carbon more than PMMA polymers.

Based on the results, a prototype was designed and the final product, multifunctional nanocomposite coated CFRP honeycomb structure, was produced and displaced.

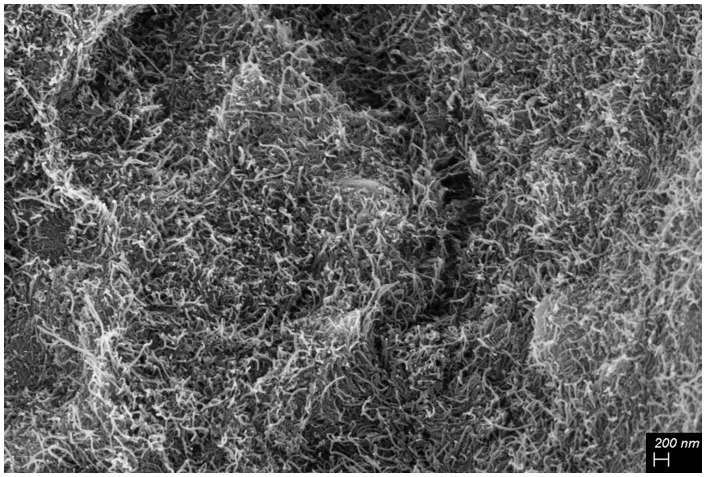

Figure 67: SEM image of PMMA/15wt%MWCNT

7.4.1 Bonding Method

Several methods of bonding CFRP with nanocomposites, such as epoxy bonded system, near-surface mounted system and plasma improved adhesive bonding, have been studied [331-333]. Due to the large scale in this research, epoxy bonding method was considered. Couple of epoxy bonding methods were tested to bond PMMA and PMMA/MWCNT onto CFRP. Details have been listed in Table 29.

Table 29: Bonding Methods

Bonding Methods	Summary
Using RS-3 as adhesive to bond CFRP and polymers	The degassing of RS-3 makes the bonding strength extremely weak, and some bubbles observed in cured adhesive
Using FM300-2 as adhesive to bond CFRP and polymers	It shows high bonding strength and durability after thermal cycling test.
Bonding polymers with CFRP by hot melting	The bonding is too weak, and CFRP can fall off without peel off force
Curing CFRP with polymers	The bonding is too weak, and CFRP can fall off without peel off force

The related properties of FM 300-2 are listed in Table 30. Based on the tests, FM 300-2 film adhesive with CTE of 1-2 $\times$ 10^{-5} cm-cm/°C from Cytec performed best for bonding between nanocomposite and CFRP honeycomb after thermal cycling. Similar thermal conductivity of the multifunctional nanocomposite (0.627 W/K-m) indicates that FM300-2 is functional to transfer heat to CFRP. Besides, high working temperature and low outgassing properties have proven to be

suitable for this project [122]. Bonding with FM 300-2 involves (i) heating the samples up to 121 °C within 30 mins; and (ii) maintain at 121 °C for another 90 mins with pressure of 0.1 MPa. To evaluate bonding property between nanocomposite, adhesive and CFRP, pull-off bonding test (section 3.2.8) associated with thermal cycling (section 3.2.4) were implemented in the subsequent sections.

Table 30: Basic Properties of FM 300-2 film adhesive

Outgassing properties	Total mass loss	0.77%
	Collected volatile condensable materials	0.02%
Curing temperature		121 °C
Glass transition temperature		143 °C
Thermal conductivity		0.381 W/K-m
Coefficient of thermal expansion		1-2 × 10^{-5} cm-cm/°C

Regarding nanocomposite, melt mixer made PMMA/15wt%MWCNT were molded into 6 cm x 6 cm shape with different patterns on the bottom where was then used to bond with CFRP honeycomb surface. Regarding the patterns, first of all, it was designed to allow adhesive film (FM300-2U) has enough space to flow during curing process. Secondly, due to thermal stress between different materials, this process will lead us to determine the optimal size of nanocomposite that can maintain the bonding strength at extreme temperatures (-170 °C and 130 °C). Figure 68 shows 1 cm x 1 cm and 1.5 cm x 1.5 cm patterns on each 6 cm x 6 cm nanocomposite. The Figure 69 shows four 6 cm x 6 cm nanocomposites with two 1 cm x 1 cm patterned at the bottom accompanied by two 1.5 cm x 1.5 cm patterned samples on the top and are ready for thermal cycling test. Adhesive film, FM300-2U, with thickness of 0.13 mm was used to bond samples onto surface of CFRP honeycomb panel.

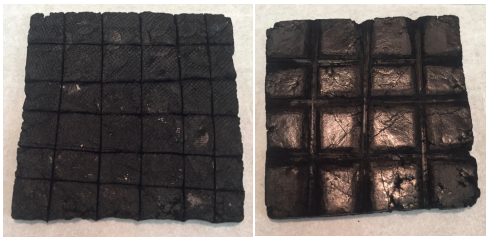

Figure 68: Patterns Made on the Bonding Surface of Nanocomposite

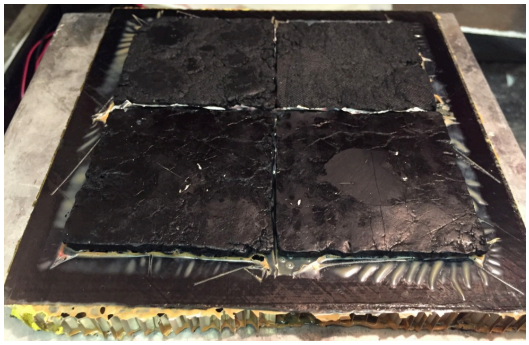

Figure 69: Bonded Nanocomposite on CFRP Honeycomb Panel

7.4.2 Characterization and Results

Thermal cycling test was applied on the previously bonded panel to investigate the mechanism between different bonded materials followed by bonding strength test on the nanocomposite before and after thermal cycling.

(i) Thermal Cycling

As shown in Figure 70, thermal stress induced deformation occurred due to greater CTE of nanocomposite than CFRP. However, ordered cracks (mostly square and rectangular shapes) on two 1 cm x 1 cm patterned nanocomposite after one thermal cycle was clearly observed. Bonding of two pieces at the bottom survived after 10 thermal cycles (Figure 70). However, the two samples on the top lost bonding strength after 3 thermal cycles. Based on the cracks on the two survived samples during thermal cycling test, edge length of each small piece was measured. In Figure 71, distribution of edges with various lengths is shown. It is found that edges with length around 2 cm predominates on the bonded nanocomposite after thermal cycling. This size provides enough space for adhesive film to breathe during curing and reduced thermal stress during vastly temperature change that greatly reduces degree of deformation during thermal cycles. As a result, 2 cm × 2 cm squared contact surface of nanocomposite was produced for further pull-off bonding strength test.

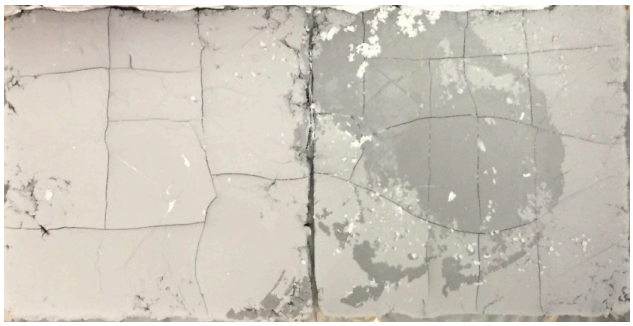

Figure 70: Frosted sample after 10 thermal cycles

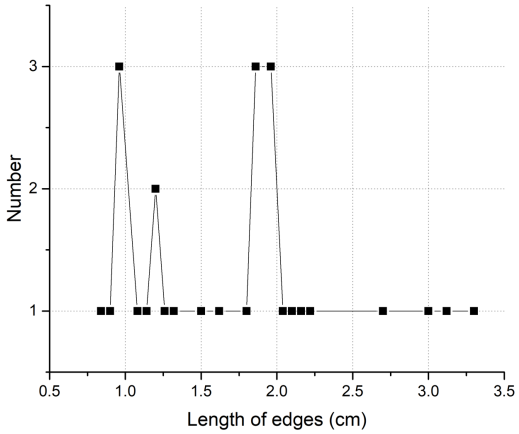

Figure 71: Area Distribution of Cracking Pieces

(ii) Bonding Strength

Based on the thermal cycling test, pull-off bonding strength test was applied on 2 cm × 2 cm PMMA/15wt%MWCNT nanocomposite samples before and after thermal cycling test. The results have been shown in Table 31. It was observed that, after pulling off, the failure layer happened on adhesive film before thermal cycling, which indicates that bonding strength of adhesive is weaker than interior mechanical strength of nanocomposite and CFRP. After thermal cycling, noticeably, bonding strength decreases about 26% and the failure part took place between CFRP and adhesive. Invisible channeling and substrate damage may occur, which is caused by the thermal stress between adhesive film and CFRP during thermal cycling [334].

Table 31: Bonding strength test

	Before thermal cycling	Failure part	After thermal cycling	Failure part
Averaged bonding strength between nanocomposite and CFRP (MPa)	2.27	Between adhesive and nanocomposite	1.68	Between adhesive and CFRP
Averaged bonding strength between CFRP and Al honeycomb (MPa)	2.45	FM 300-2 Adhesive film and CFRP	2.25	FM 300-2 Adhesive film and CFRP

Bonding strength on CFRP honeycomb is shown in Table 31. Compared to bonding strength between CFRP and honeycomb (2.45 MPa) before 10 thermal cycles, CFRP honeycomb has shown lower bonding strength of 2.25 MPa after that. Both test illustrates failure layer happened on FM 300-2 Adhesive film and CFRP lamination. In other words, bonding strength between CFRP and nanocomposite is similar to the strength between CFRP and Al honeycomb.

The results suggest that (i) nanocomposite can maintain mechanical strength before and after thermal cycling; (ii) distinct CTE between layers can cause more deformations such as delamination on CFRP than nanocomposite; (iii) Epoxy adhesive has achieved proper bonding so that the multilayered structure will not suffer severe mechanical failure before and after thermal cycling. Herein, method of adhering multifunctional nanocomposite (2 cm × 2 cm) onto CFRP honeycomb structure with FM 300-2 was adopted to produce a prototype in our lab.

7.4.3 Prototype Design

Aluminum is a conventional structural material widely used in space industry, and aluminum-equivalent areal density is often used to scale radiation shielding capability on spacecraft such as ISS [335]. According to NASA's report, for radiation shielding, the minimum aluminum-equivalent areal densities range from 2 to 5 g/cm^2 on the ISS [336]. Thus, as shown in Figure 64, relationship between areal density of material and stopping energy for proton radiation has been presented and applied in this section. A prototype based on our experiment data was designed to compare with Al used in space applications.

First of all, in our previous study on electron radiation shielding, under the same electron beam energy, the same radiation shielding effectiveness was found when areal densities of all materials increase to a certain point (saturated point). In order to further investigate saturated points and weight advantages of our nanocomposite under various electron beam energies, the fitted curves are plotted in Figure 72, based on the experimental results shown in Figure 55 for all materials. The fitted curves for 9 MeV electron beam in Figure 72 are compared with experimental data plotted in

Figure 57 to identify the accuracy of the nonlinear fitting method. First order differential of the fitted curves of nanocomposite (PMMA/MWCNT) and Al are calculated to find the saturated points due to the largest difference between the nanocomposite and Al.

$$\Delta D = f'_{Al}(x) - f'_{nanocomposite}(x)$$

When the difference (ΔD) merges to 0.2, saturated points are then determined for each energy, and that of 3.36 g/cm^2 is found for the 9MeV fitted curves. Compared to experimental data (3.3 g/cm^2), minor difference of 1.8% indicates calculation of the fit curve is reliable. Thus, fit curves of the other three electron energies are implemented with the same method. A noticeable phenomenon was found that the maximum attenuation percentages at saturated points (Figure 72) decreases accordingly when primary electron beam energy increases from 9 to 20 MeV. In other words, greater quantity of transmitted instant electrons and secondary radiations can be detected when shielding higher energies of electron radiation. Moreover, saturated points as a function of electron energies are illustrated in Figure 73. The linear relationship between them is presented, but electron energy of 9 MeV is showing slightly drifting from the other points. Potentially, this plot is able to be applied to predict saturated areal densities for electron radiation shielding at other electron energies than the four measured in this study.

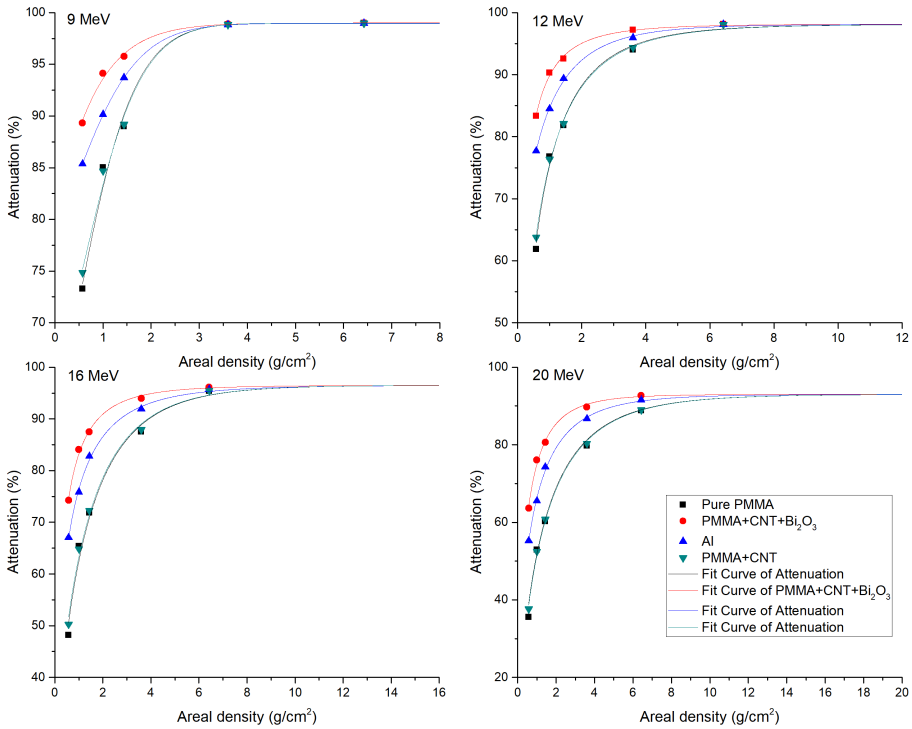

Figure 72: Fit curves for electron energies of 9, 12, 16 and 20 MeV vs. areal density of all materials

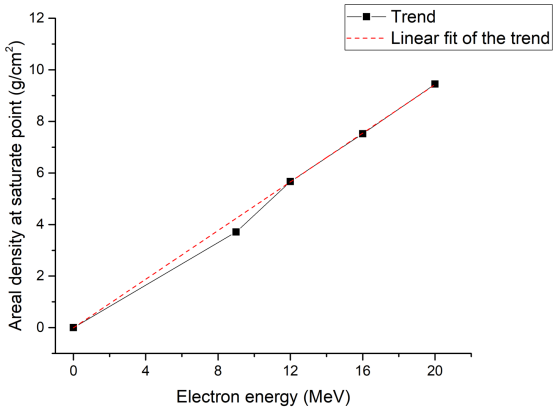

Figure 73: Saturated areal density vs. electron energy

According to the relationship of electron attenuation and areal densities plotted in Figure 72, the maximum weight advantages of PMMA/MWCNT/Bi_2O_3 are found and listed in Table 32. The attenuation characteristics of all the materials as a function of different areal densities and energies shows that the PMMA/MWCNT/Bi_2O_3 nanocomposite would be much lighter (about 37% lighter regardless of electron energy) material than Al for electron radiation shielding. For example, at electron energy of 9 MeV, the nanocomposite is found to have maximum 37.49% weight advantage in comparison with Al at electron beam attenuation of 90%, which is found to be the best shielding characteristics of the nanocomposite (PMMA/MWCNT/Bi_2O_3) for all measured energies. Moreover, it is adverted that attenuation percentages at the greatest weight advantages of nanocomposite decrease accordingly when the primary electron beam energy goes up, which has a similar trend as the maximum attenuation percentages at the saturated points. The results and analysis of this work can be a design criterion for electron radiation shielding.

Table 32: Weight advantage with respect to Al for all energies

Electron energy (MeV)	**Maximum percentage weight reduction (%)**	**Areal density of nanocomposite at the max weight reduction (g/cm^2)**	**Attenuation at the greatest weight advantage**
9	37.49	0.61776	90%
12	36.34	0.76769	87%
16	36.16	0.58903	75%
20	36.30	0.76862	70%

After that, a prototype was developed in our lab based on the results discussed above. Depending on the experiment and simulation results, a range of areal densities of materials and corresponding proton stopping energy are presented in Figure 74. As simulated, aluminum-equivalent areal

densities range from 2 to 5 g/cm^2 is able to fully stop proton energy of 40.7 to 68 MeV. To provide sufficient protection for carbon fibres in CFRP, CFRP honeycomb is considered to contribute zero radiation shielding effectiveness. Accordingly, areal densities (1.65-4.21 g/cm^2) of nanocomposite with CFRP honeycomb (0.223 g/cm^2), which is considered not to contribute any radiation shielding effectiveness, have been calculated (0.223 g/cm^2 has been added on areal density of PMMA/15wt%MWCNT) as blue line in Figure 74 based the plots in Figure 64. Therefore, the weight reduction of nanocomposite protected CFRP honeycomb structure over Al increases from 9.12% to 16.32% when proton radiation energy raised from 40.7 to 68 MeV. In literature review, as shown in Figure 5, 40.7 MeV proton has the similar flux as that of 4 MeV electron in LEO. Consequently, as plotted in Figure 73, maximum electron attenuation has been reached (saturated point) with areal density of 1.65 g/cm^2 when shielding 4 MeV electron. As indicated in Figure 74, nanocomposite with areal density of 1.65 g/cm^2 is equivalent to Al areal density of 2.08 g/cm^2, which exceeds the minimum radiation shielding requirement on ISS [336]. Thus, to protect potential payloads on spacecraft from those hazardous proton and electron radiations, multifunctional PMMA/15wt%MWCNT nanocomposite with areal density of 1.65 g/cm^2 was designed to be coated on 100 cm × 60 cm CFRP honeycomb structure. Compared to Al, weight reduction of 9.12% has been achieved in the multifunctional structure (multifunctional nanocomposite + CFRP honeycomb).

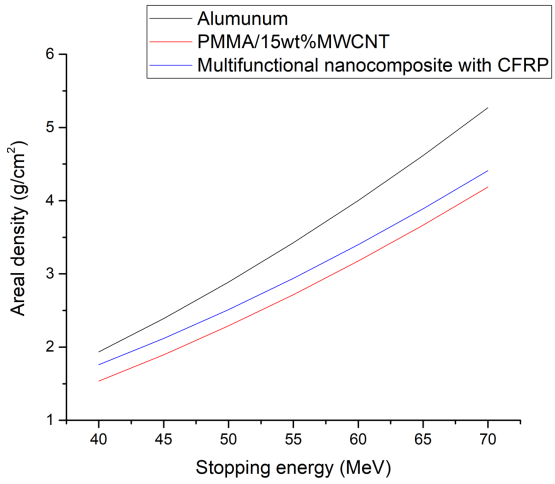

Figure 74: Areal density vs. proton stopping energy.

According to thermal cycling and bonding strength tests results, nanocomposites were molded into 2 cm × 2 cm square shaped coupons by following the molding process described in section 3.1.5. After that, those nanocomposites were tiled onto CFRP honeycomb panel with FM300-2U adhesive

film between. About 1 mm gap between each piece of nanocomposite (2 cm × 2 cm square) and rounded corner were designed to decrease thermal stress and increase the lifetime of the multifunctional structure. To minimize ionizing particle penetration from those gaps, squared nanocomposites with about 0.34 cm thickness were layered up to 1.37 cm (areal density 1.65 g/cm^2) with 1 cm dislocation between each layer. The basic idea is showing in Figure 75. Eventually, the final prototype is shown in Figure 76.

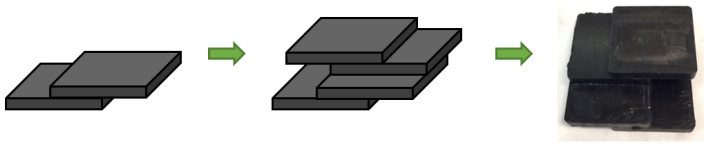

Figure 75: Design of tiled up nanocomposite with thickness of 1.2 cm

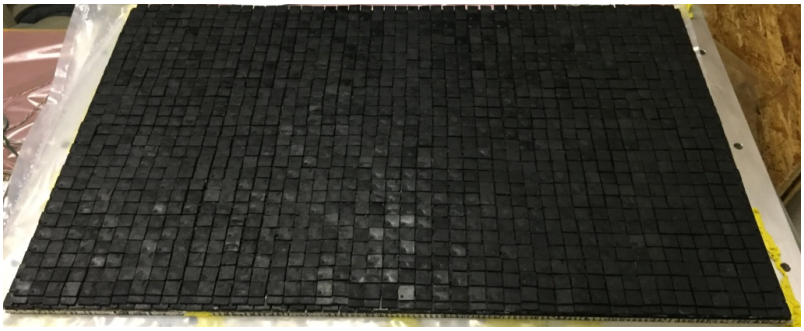

Figure 76: 100 cm × 60 cm multifunctional nanocomposite protected CFRP honeycomb structure

Chapter 8 Conclusions and Recommendation for Future Studies

8.1 Conclusion

Currently applied materials in space applications are still limited by the insufficient shielding effectiveness, low functions to weight ratio, high-cost, and difficulties of manufacturing and handling. Till date, several composites, most common one being the CFRP, have been used in space missions to reduce the overall weight without reducing mechanical properties compared to metallic materials such as Al. Through reviewing varies of nanotechnologies for novel material designs, the concept of polymer-based nanocomposites is found suitable for developing required space radiation shielding due to the ease of tuning material properties by applying nanofillers. Carbon nanotubes and bismuth oxide nanoparticles were finally targeted to be the candidate nanomaterials to be used as the nanofillers providing multifunctional reinforcement in polymer matrix due to their superior comprehensive material properties. Developed nanocomposites were evaluated by radiation shielding tests and characterization to clarify their properties and potentials. The optimization of multifunctional nanocomposite was carried out to cohere and work simultaneously with CFRP honeycomb structure. The major contributions of this thesis are summarized here:

According to literature review, PMMA, MWCNT and Bi_2O_3 were found to be a suitable polymer matrix and nanofillers for bulk fabrication of nanocomposite as proton and electron radiation shielding. First of all, PMMA/MWCNT nanocomposites with three different MWCNT loadings (1, 3 and 5 wt%) were fabricated for characterization. Tensile strength was measured for all the samples and the strength order was found: PMMA/MWCNT(3wt%)-31.65MPa > PMMA/MWCNT(5wt%)-26.41MPa > PMMA/MWCNT(1wt%)-21.58MPa. Furthermore, thermal stability was extensively studied using TGA apparatus for a wide range of temperatures (20 to 800 °C). It is found that the temperature of thermal decomposition was observed about 25% higher for nanocomposites with 3 and 5 wt% MWCNT compared to PMMA and PMMA/1wt% MWCNT. According to the measured properties, PMMA with 3wt% of MWCNT loading was prepared for proton radiation shielding test (TRIUMF) and further characterization.

Regarding proton radiation shielding test, four different thicknesses of nanocomposite, control sample (PMMA) and Al were irradiated under four proton energies within the range of 0 to 105 MeV. The corresponding water equivalent areal densities of each sample were measured and calculated for comparison of proton stopping efficiency. The results show that the nanocomposite and the control sample are 18.89% to 19.89% and 17.86% to 18.71% lighter than Al in weight

respectively to fully stop incident protons at the same energy. Besides that, secondary neutron generation of all materials with four different thicknesses was measured during the proton shielding tests. The ratio of the neutron generated around irradiated samples and the proton fluence were recorded. These data were then used to compare the secondary neutron generation of each material. PMMA/MWCNT (3wt%) demonstrates 3.76 to 5.07% less secondary neutron generation when compared to that of Al at proton energies from 65 to 101 MeV. However, pure PMMA just shows 2.42% to 3.98% less secondary neutron generation when compared to Al at the same proton energy range. It is proved that MWCNT in polymer matrix is able to reduce secondary neutron generation or absorb more neutrons than PMMA matrix.

For electron shielding, 30wt% of Bi_2O_3 nanoparticles were added into 3wt% MWCNT loaded PMMA nanocomposite, which is formerly tested as proton radiation shield, to form a nanocomposite of PMMA/MWCNT/Bi_2O_3. The percentage attenuation characteristics at each of the four electron beam energies (9, 12, 16 and 20 MeV) for five areal densities (0.576, 1, 1.44, 3.6, and 6.426) of the nanocomposite were found to be higher than those of the Al. It is interesting to note that all materials (pure polymer, nanocomposites and Al) showed similar attenuation characteristics at very high areal densities (saturated points). The phenomenon indicates that the same weight advantage represented for every material over another at high areal densities due to few transmitted primary and secondary radiations. At electron attenuation of 90%, overall weight reduction of at least 27% have been achieved for the PMMA/MWCNT/Bi_2O_3 nanocomposite compared to Al.

Regarding scaled-up fabrication of the multifunctional nanocomposites, material properties of nanocomposites fabricated by two commonly used industrial fabrication processes, twin-screw extruder and double planetary mixer, was investigated. It is obvious that twin-screw extruder can decrease mechanical strength and thermal conductivity of polymer matrix and its nanocomposite since the exceedingly high shear force during mixing process. Therefore, double planetary mixer with less shear force and vacuum system had been used to produce the multifunctional radiation shielding layer.

Previous work and current problem had been reviewed, and a guideline for further optimization, fabrication and characterization was presented. Due to the high thermal expansion coefficient of PMMA (6×10^{-5} cm-cm/°C), PMMA nanocomposites loaded with various weight percentages of MWCNT (5wt% to 20wt%) were designed to optimize the thermal properties. Based on the data from NASA's report, radiation shielding experiment results from TRIUMF were used to compare

with SRIM software simulation results to reveal the reliable capability of simulation. According to the DSC results, PMMA/15wt%MWCNT is an ideal candidate due to its high glass transition temperature and relatively low thermal expansion.

Characterization including thermal cycling tests and bonding strength tests have been implemented on the nanocomposites coated CFRP honeycomb structure. Bonding strength test results show about 26% reduced strength for samples after thermal cycling since the thermal stress between different layers, nanocomposite, adhesive and CFRP. However, the bonding strength remained between nanocomposite and CFRP surface. Based on the results, nanocomposites with 2 cm x 2 cm square shape were fabricated by designed mixing and molding process. Moreover, according to our proton and electron radiation shielding test results and the simulated results were adopted and evaluated to design areal density of the units of multifunctional nanocomposite for space radiation shielding applications. Eventually, adequate nanocomposite was fabricated to assemble a prototype, a 100 cm × 60 cm multifunctional CFRP honeycomb panel.

8.2 Future Work

The work conducted in this thesis has concluded an approach to fabricate and evaluate scaled-up light-weight radiation shielding structure. It is highly promising to transfer it into industrial or commercial product. Herein, some unfinished research and unexplored possibilities are listed here:

- Reduced secondary neutron radiation: Boron (^{10}B) rich materials have been proven the ideal fillers for thermal neutron absorption with secondary radiation of gamma rays. With high thermal conductivity and negative CTE, boron nitride (BN) nanosheet is a promising candidate for the future research. It is believed that, by adding certain wt% of BN nanosheet, dispersion quality of 15wt%MWCNT in PMMA matrix will be further improved [149]. The new nanocomposite has to associate with another outer layer of nanocomposite with high-Z material, such as Bi_2O_3, which is able to slow fast neutron down to thermal neutron.
- Bonding with CFRP: By adding extra nanomaterial with negative CTE into nanocomposite will largely benefit reduction of overall CTE of radiation shielding layer. Therefore, the bonding strength between nanocomposite and CFRP honeycomb is expected to be improved before and after thermal cycling.
- Massive radiation shielding simulation: Based on the results of our experiment data, simulations such as FLUKA can be carried out to evaluate shielding properties in various

radiation environment. Improved radiation shielding layers design may be induced accordingly.

- CFRP honeycomb structure enhancement: Nowadays, space applications have attracted more attentions to develop innovative CFRP involved structures. CFRP honeycomb structure modified with radiation shielding nanocomposite can considerably enhance its overall properties for space missions.

References

1. Cucinotta, F.A., M.-H.Y. Kim, and L. Ren, *Evaluating shielding effectiveness for reducing space radiation cancer risks*. Radiation measurements, 2006. **41**(9): p. 1173-1185.
2. Board, S.S., *Radiation Hazards to Crews of Interplanetary Missions.* Natl. Acad. Press, Washington, DC, 1996.
3. Wilson, J., et al., *2006-01-2110 Spacesuit Radiation Shield Design Methods.* SAE TRANSACTIONS, 2007. **115**(1): p. 277.
4. Nambiar, S. and J.T.W. Yeow, *Polymer-Composite Materials for Radiation Protection.* ACS Applied Materials & Interfaces, 2012. **4**(11): p. 5717-5726.
5. Chancellor, J.C., G.B. Scott, and J.P. Sutton, *Space radiation: the number one risk to astronaut health beyond low earth orbit.* Life, 2014. **4**(3): p. 491-510.
6. Benton, E. and E. Benton, *Space radiation dosimetry in low-Earth orbit and beyond.* Nuclear Instruments and Methods in Physics Research Section B: Beam Interactions with Materials and Atoms, 2001. **184**(1): p. 255-294.
7. Heilbronn, L., et al., *Overview of secondary neutron production relevant to shielding in space.* Radiation protection dosimetry, 2005. **116**(1-4): p. 140-143.
8. Horstmann, M., et al., *Space radiation does not induce a significant increase of intrachromosomal exchanges in astronauts' lymphocytes*. Radiation and environmental biophysics, 2005. **44**(3): p. 219-224.
9. Sprawls, P., *Physical principles of medical imaging*. 1995: Medical Physics Pub.
10. *Chapter 17 Interaction of Radiation with Matter*. Available from: http://oregonstate.edu/instruct/ch374/ch418518/Chapter%2017%20Interaction%20of%20Radiation%20with%20Matter-rev.pdf.
11. Turner, J.E., *Atoms, radiation, and radiation protection.* Willey, New York, 2007.
12. Carron, N.J., *An introduction to the passage of energetic particles through matter*. 2006: CRC Press.
13. Durante, M., *Space radiation protection: destination Mars.* Life sciences in space research, 2014. **1**: p. 2-9.
14. Cucinotta, F.A., M.-H.Y. Kim, and L.J. Chappell, *Evaluating shielding approaches to reduce space radiation cancer risks.* NASA Technical Memorandum, 2012. **217361**.
15. Rapp, D., *Radiation effects and shielding requirements in human missions to the Moon and Mars*. Vol. 2. 2006. 46-71.
16. Piekutowski, A., et al., *Performance of Whipple shields at impact velocities above 9km/s*. International Journal of Impact Engineering, 2011. **38**(6): p. 495-503.
17. Adams Jr, J., et al., *Revolutionary concepts of radiation shielding for human exploration of space.* NASA TM, 2005. **213688**.
18. Bell, J., et al., *Radiation Shielding for a Lunar Base*. 2011, NASA report.
19. De Groh, K.K., et al. *NASA Glenn Research Center's materials international space station experiments (MISSE 1-7)*. in *Proceedings of the International Symposium on "SM/MPAC&SEED Experiment*. 2008.
20. Clayton, L.N., Gerasimov, T. G., Cinke, M., Meyyappan, M., Harmon, J. P. , *Dispersion of Single-walled Carbon Nanotubes in a Non-polar Polymer, Poly(4-methyl-1-pentene)*. Journal of Nanoscience and Nanotechnology, 2006. **6**: p. 2520-2524.
21. Kaul, R.K., et al., *Multi-functional layered structure having structural and radiation shielding attributes*. 2010, Google Patents.
22. Effects, R., *Shielding Requirements in Human Missions to the Moon and Mars, D. Rapp.* Mars, 2006. **2**: p. 46-71.
23. Li, X., D. Warden, and Y. Bayazitoglu, *Analysis to Evaluate Multilayer Shielding of Galactic Cosmic Rays*. Journal of Thermophysics and Heat Transfer, 2017: p. 1-7.

24. Gaier, J.R., et al., *Effect of intercalation in graphite epoxy composites on the shielding of high energy radiation.* Journal of materials research, 1998. **13**(08): p. 2297-2301.
25. Muisener, P., et al., *Effects of gamma radiation on poly (methyl methacrylate)/single-wall nanotube composites.* Journal of materials research, 2002. **17**(10): p. 2507-2513.
26. Liu, J., et al., *Processing and properties of carbon nanotube/poly (methyl methacrylate) composite films.* Journal of applied polymer science, 2009. **112**(1): p. 142-156.
27. Li, Z., et al., *PDMS/single-walled carbon nanotube composite for proton radiation shielding in space applications.* Materials Letters, 2013. **108**: p. 79-83.
28. Najafi, E. and K. Shin, *Radiation resistant polymer-carbon nanotube nanocomposite thin films.* Colloids and Surfaces A: Physicochemical and Engineering Aspects, 2005. **257**: p. 333-337.
29. Mathew, S., et al., *The effect of layer number and substrate on the stability of graphene under MeV proton beam irradiation.* Carbon, 2011. **49**(5): p. 1720-1726.
30. Telling, R.H., et al., *Wigner defects bridge the graphite gap.* Nature Materials, 2003. **2**(5): p. 333.
31. Krasheninnikov, A. and F. Banhart, *Engineering of nanostructured carbon materials with electron or ion beams.* Nature materials, 2007. **6**(10): p. 723.
32. Ho, C.-H., et al., *The study of optical band edge property of bismuth oxide nanowires α-Bi 2 O 3.* Optics express, 2013. **21**(10): p. 11965-11972.
33. Leontie, L., et al., *Structural and optical characteristics of bismuth oxide thin films.* Surface Science, 2002. **507**: p. 480-485.
34. Singh, V.P., et al., *Evaluation of gamma-ray exposure buildup factors and neutron shielding for bismuth borosilicate glasses.* Radiation Physics and Chemistry, 2014. **98**: p. 14-21.
35. *Properites of Al 6061*. Available from: http://asm.matweb.com/search/SpecificMaterial.asp?bassnum=MA6061t6.
36. Rolfes, R. and U. Hammerschmidt, *Transverse thermal conductivity of CFRP laminates: a numerical and experimental validation of approximation formulae.* Composites Science and Technology, 1995. **54**(1): p. 45-54.
37. Battaglia, J.-L., et al., *Carbon epoxy composites thermal conductivity at 77 K and 300 K.* Journal of Applied Physics, 2014. **115**(22): p. 223516.
38. *Types of Carbon Fiber*. Available from: https://www.toraycma.com/page.php?id=661.
39. Stöcker, J., P. Parigger, and M. Thiel. *Structural development of Equator-S*. in *Spacecraft Structures, Materials and Mechanical Engineering*. 1996.
40. Townsend, L.W., *Implications of the space radiation environment for human exploration in deep space.* Radiation protection dosimetry, 2005. **115**(1-4): p. 44-50.
41. Reitz, G., *Characteristic of the radiation field in low earth orbit and in deep space.* Zeitschrift für Medizinische Physik, 2008. **18**(4): p. 233-243.
42. Barth, J.L., *Space and atmospheric environments: from low earth orbits to deep space*, in *Protection of Materials and Structures from Space Environment*. 2004, Springer. p. 7-29.
43. Badhwar, G.D., *The radiation environment in low-Earth orbit.* Radiation research, 1997. **148**(5s): p. S3-S10.
44. Hochedez, J.F., et al. *Solar weather monitoring*. in *Annales Geophysicae*. 2005. Copernicus GmbH.
45. LaBel, K.A., M. Gates, and P. Marshal, *SEECA: Single Event Effect Criticality Analysis.* Radiation Effects and Analysis Group, Goddard Space Flight Centre, http://flick.gsfc.nasa.gov/radhome/papers/seecai.htm, 1996.
46. Schwenn, R., *Space weather: the solar perspective.* Living Reviews in Solar Physics, 2006. **3**(2): p. 1-72.
47. Rojdev, K., et al. *Comparison and Validation of FLUKA and HZETRN as Tools for Investigating the Secondary Neutron Production in Large Space Vehicles*. in *AIAA SPACE 2015 Conference and Exposition*. 2015.

48. Booyabazooka. *Van Allen radiation belt*. 2006; Available from: http://en.wikipedia.org/wiki/Van_Allen_radiation_belt.
49. Walters, R.J., et al. *Modeling of radiation induced defects in space solar cells*. in *Physics and Simulation of Optoelectronic Devices XIX*. 2011. International Society for Optics and Photonics.
50. *Orbital inclination*. Available from: https://en.wikipedia.org/wiki/Orbital_inclination.
51. Petkov, M.P., *The effects of space environments on electronic components.* 2003.
52. Henini, M., *Handbook of self assembled semiconductor nanostructures for novel devices in photonics and electronics*. 2011: Elsevier.
53. Inguimbert, C. and S. Messenger, *Equivalent displacement damage dose for on-orbit space applications.* IEEE Transactions on Nuclear Science, 2012. **59**(6): p. 3117-3125.
54. Gerald J. Dittberner, A.J.G., jr., David M. Tralli, and Shyam N. Bajpai, *MEDIUM EARTH ORBIT (MEO) AS A VENUE FOR FUTURE NOAA SATELLITE SYSTEMS.* 2005.
55. Center, L.B.J.S., *Understanding Space Radiation*, NASA, Editor. 2002, NASA FACTS.
56. Mewaldt, R., et al. *The Cosmic Ray Radiation Dose in Interplanetary Space Present Day and Worst-Case Evaluations*. in *International Cosmic Ray Conference*. 2005.
57. Rapp, D., *MARS MARS.* 2006.
58. Hassler, D.M., et al., *Mars' Surface Radiation Environment Measured with the Mars Science Laboratory's Curiosity Rover.* Science, 2014. **343**(6169): p. 1244797.
59. Simonsen, L.C. *Analysis of lunar and Mars habitation modules for the space exploration initiative (SEI)*. in *Shielding Strategies for Human Space Exploration," Edited by JW Wilson, J. Miller, A. Konradi, and FA Cucinotta. NASA Conference Publication*. 1997.
60. Drake, B.G., S.J. Hoffman, and D.W. Beaty. *Human Exploration of Mars, Design Reference Architecture 5.0*. in *Aerospace Conference, 2010 IEEE*. 2010. IEEE.
61. Wilson, J., et al., *Issues in deep space radiation protection.* Acta Astronautica, 2001. **49**(3): p. 289-312.
62. Wilson, J., et al., *Shielding strategies for human space exploration*. 1997: NASA Washington DC.
63. Durante, M., et al., *Chromosome aberration dosimetry in cosmonauts after single or multiple space flights.* Cytogenetic and genome research, 2003. **103**(1-2): p. 40-46.
64. George, K., et al., *Chromosome aberrations in the blood lymphocytes of astronauts after space flight.* Radiation research, 2001. **156**(6): p. 731-738.
65. George, K., et al., *Chromosome aberrations of clonal origin are present in astronauts' blood lymphocytes.* Cytogenetic and genome research, 2004. **104**(1-4): p. 245-251.
66. Wilson, J., et al., *Optimized shielding for space radiation protection.* Physica Medica, 2001. **17**: p. 67-71.
67. Barth, J.L., C. Dyer, and E. Stassinopoulos, *Space, atmospheric, and terrestrial radiation environments.* Nuclear Science, IEEE Transactions on, 2003. **50**(3): p. 466-482.
68. Cucinotta, F.A. and M. Durante, *Cancer risk from exposure to galactic cosmic rays: implications for space exploration by human beings.* The lancet oncology, 2006. **7**(5): p. 431-435.
69. Cucinotta, F.A., et al., *Physical and biological organ dosimetry analysis for International Space Station astronauts.* Radiation research, 2008. **170**(1): p. 127-138.
70. Vazquez, M., *Neurobiological problems in long-term deep space flights*. Advances in Space Research, 1998. **22**(2): p. 171-183.
71. Rabin, B.M., K.L. Carrihill-Knoll, and B. Shukitt-Hale, *Operant responding following exposure to HZE particles and its relationship to particle energy and linear energy transfer.* Advances in Space Research, 2011. **48**(2): p. 370-377.
72. Newhauser, W.D. and R. Zhang, *The physics of proton therapy.* Physics in Medicine & Biology, 2015. **60**(8): p. R155.

73. *Interactions of Radiation with Matter* Available from: http://courses.chem.indiana.edu/c460/documents/SEC5-InteractionsofRadiationwithMatter_000.pdf.
74. Wikipedia. *Stopping power (particle radiation)*. Available from: https://en.wikipedia.org/wiki/Stopping_power_(particle_radiation).
75. Benton, E. and E. Benton, *Space radiation dosimetry in low-Earth orbit and beyond.* Nuclear Instruments and Methods in Physics Research Section B: Beam Interactions with Materials and Atoms, 2001. **184**(1-2): p. 255-294.
76. Saxena, A., et al., *Stopping power of electrons and positrons for c, al, cu, ag, au, pb, fe, u, ge, si and mo.* Applied Physics Research, 2010. **2**(2): p. 176.
77. Sharif, J., et al., *Preparation and properties of radiation crosslinked natural rubber/clay nanocomposites.* Polymer Testing, 2005. **24**(2): p. 211-217.
78. Varier, K.M., *Nuclear Radiation Detection, Measurements and Analysis*. 2009: Alpha Science Intl Ltd.
79. ; Available from: http://www.astronautix.com/craft/mir.htm.
80. Rawal, S.P., *Metal-matrix composites for space applications.* JOM, 2001. **53**(4): p. 14-17.
81. Pater, R.H. and P.A. Curto, *Advanced materials for space applications.* Acta Astronautica, 2007. **61**(11): p. 1121-1129.
82. *3M Nextel Ceramic Fabric Offers Space Age Protection*. 1997.
83. Williams, J.C. and E.A. Starke Jr, *Progress in structural materials for aerospace systems.* Acta Materialia, 2003. **51**(19): p. 5775-5799.
84. *Heat dissipation In Space*. 2010; Available from: http://www.physicsforums.com/showthread.php?t=399450.
85. Gilmore, D.G. and M. Donabedian, *Spacecraft Thermal Control Handbook: Cryogenics*. Vol. 2. 2003: AIAA.
86. Majumdar, A., *Microscale transport phenomena.* Handbook of Heat Transfer, 1998.
87. Fourspring, K., et al., *Proton radiation testing of digital micromirror devices for space applications.* Optical Engineering, 2013. **52**(9): p. 091807-091807.
88. *Payload*. Available from: http://en.wikipedia.org/wiki/Payload.
89. *FAA Semi-Annual Launch Report: Second Half of 2009*. 2011, Federal Aviation Administration - Office of Commercial Space Transportation. p. end of document.
90. Wikipedia. *SpaceX reusable launch system development program.* Available from: https://en.wikipedia.org/wiki/SpaceX_reusable_launch_system_development_program.
91. Tripathi, R.K., J.W. Wilson, and R.C. Youngquist, *Electrostatic space radiation shielding.* Advances in Space Research, 2008. **42**(6): p. 1043-1049.
92. Wikipedia. *Polysulfone*. Available from: https://en.wikipedia.org/wiki/Polysulfone.
93. Borggräfe, A., M. Quatmann, and D. Nölke, *Radiation protective structures on the base of a case study for a manned Mars mission.* Acta Astronautica, 2009. **65**(9-10): p. 1292-1305.
94. *Material Property Database-Polyimide*. Available from: http://www.mit.edu/~6.777/matprops/polyimide.htm.
95. Malpass, D.B., *Introduction to industrial polyethylene: properties, catalysts, and processes*. Vol. 45. 2010: Wiley. com.
96. Ulrich, H., *Introduction to industrial polymers*. 1982: Hanser Munich.
97. Guetersloh, S., et al., *Polyethylene as a radiation shielding standard in simulated cosmic-ray environments.* Nuclear Instruments and Methods in Physics Research Section B: Beam Interactions with Materials and Atoms, 2006. **252**(2): p. 319-332.
98. Shavers, M., et al., *Implementation of ALARA radiation protection on the ISS through polyethylene shielding augmentation of the Service Module Crew Quarters.* Advances in Space Research, 2004. **34**(6): p. 1333-1337.
99. Cucinotta, F.A., M.-H.Y. Kim, and L. Ren, *Evaluating shielding effectiveness for reducing space radiation cancer risks.* Radiation Measurements, 2006. **41**(9-10): p. 1173-1185.

100. Dini, V., et al., *Influence of PMMA shielding on DNA fragmentation induced in human fibroblasts by iron and titanium ions.* Radiation research, 2005. **164**(4): p. 577-581.
101. Durante, M., et al., *Influence of the shielding on the induction of chromosomal aberrations in human lymphocytes exposed to high-energy iron ions.* Journal of radiation research, 2002. **43**(S): p. S107-S111.
102. Durante, M., et al., *Cytogenetic effects of high-energy iron ions: dependence on shielding thickness and material.* Radiation research, 2005. **164**(4): p. 571-576.
103. Mancusi, D., et al., *Comparison of aluminum and lucite for shielding against 1 GeV protons.* Advances in Space Research, 2007. **40**(4): p. 581-585.
104. Zeitlin, C., et al., *Measurements of materials shielding properties with 1GeV/nuc< sup> 56</sup> Fe.* Nuclear Instruments and Methods in Physics Research Section B: Beam Interactions with Materials and Atoms, 2006. **252**(2): p. 308-318.
105. *Material Properties of Polystyrene*

and Poly(methyl methacrylate)

(PMMA) Microspheres. Available from: https://www.bangslabs.com/sites/default/files/imce/docs/TSD%200021%20Material%20Properties%20Web.pdf.
106. Yang, C., et al., *Thermal conductivity enhancement of recycled high density polyethylene as a storage media for latent heat thermal energy storage.* Solar Energy Materials and Solar Cells, 2016. **152**: p. 103-110.
107. Wikipedia. *Polyethylene*. Available from: https://en.wikipedia.org/wiki/Polyethylene.
108. Bhattacharya, A., *Radiation and industrial polymers.* Progress in Polymer Science, 2000. **25**(3): p. 371-401.
109. Harrison, C., et al., *Polyethylene/boron nitride composites for space radiation shielding.* Journal of Applied Polymer Science, 2008. **109**(4): p. 2529-2538.
110. Ajayan, P.M., L.S. Schadler, and P. Braun, *Nanocomposite Science and Technology. 2003*. 2005, Wiley-VCH Verlag, Weinheim.
111. Samaras, M., et al., *Radiation damage near grain boundaries.* Philosophical Magazine, 2003. **83**(31-34): p. 3599-3607.
112. Chimi, Y., et al., *Accumulation and recovery of defects in ion-irradiated nanocrystalline gold.* Journal of nuclear materials, 2001. **297**(3): p. 355-357.
113. Chimi, Y., et al., *Swift heavy ion irradiation effects in nanocrystalline gold.* Nuclear Instruments and Methods in Physics Research Section B: Beam Interactions with Materials and Atoms, 2006. **245**(1): p. 171-175.
114. Nita, N., et al., *Effects of irradiation on the microstructure and mechanical properties of nanostructured materials.* Philosophical Magazine, 2005. **85**(4-7): p. 723-735.
115. Bai, X.M., et al., *Efficient annealing of radiation damage near grain boundaries via interstitial emission.* Science, 2010. **327**(5973): p. 1631-1634.
116. *Introduction to Crystallography*. Available from: https://ocw.mit.edu/courses/materials-science-and-engineering/3-091sc-introduction-to-solid-state-chemistry-fall-2010/crystalline-materials/15-introduction-to-crystallography/.
117. Zhong, W.H., et al., *Cosmic radiation shielding tests for UHMWPE fiber/nano-epoxy composites.* Composites Science and Technology, 2009. **69**(13): p. 2093-2097.
118. Okamoto, M., T. Fujigaya, and N. Nakashima, *Individual Dissolution of Single-Walled Carbon Nanotubes by Using Polybenzimidazole, and Highly Effective Reinforcement of Their Composite Films.* Advanced Functional Materials, 2008. **18**(12): p. 1776-1782.
119. Choi, E., et al., *Enhancement of thermal and electrical properties of carbon nanotube polymer composites by magnetic field processing.* Journal of Applied Physics, 2003. **94**(9): p. 6034-6039.

120. Marconnet, A.M., et al., *Thermal conduction in aligned carbon nanotube-polymer nanocomposites with high packing density.* ACS nano, 2011. **5**(6): p. 4818-4825.
121. Boul, P.J., et al., *Single wall carbon nanotube response to proton radiation.* The Journal of Physical Chemistry C, 2009. **113**(32): p. 14467-14473.
122. Neupane, P., et al., *Proton irradiation effect on single-wall carbon nanotubes in a poly (3-octylthiophene) matrix.* Applied Physics Letters, 2005. **86**(22): p. 221908-221908-3.
123. Basiuk, V.A., et al., *Irradiation of single-walled carbon nanotubes with high-energy protons.* Nano Letters, 2002. **2**(7): p. 789-791.
124. Adhikari, A., et al., *Effects of proton irradiation on thermal stability of single-walled carbon nanotubes mat.* Nuclear Instruments and Methods in Physics Research Section B: Beam Interactions with Materials and Atoms, 2006. **245**(2): p. 431-434.
125. Ghosh, S., et al., *Dimensional crossover of thermal transport in few-layer graphene.* Nature materials, 2010. **9**(7): p. 555.
126. Mathew, S., et al., *The effects of 2 MeV Ag ion irradiation on multiwalled carbon nanotubes.* Carbon, 2007. **45**(13): p. 2659-2664.
127. Mathew, S., et al., *X-ray photoelectron and Raman spectroscopic studies of MeV proton irradiated graphite.* Nuclear Instruments and Methods in Physics Research Section B: Beam Interactions with Materials and Atoms, 2008. **266**(14): p. 3241-3246.
128. Cai, W., et al., *Synthesis of bulk-size transparent gadolinium oxide–polymer nanocomposites for gamma ray spectroscopy.* Journal of Materials Chemistry C, 2013. **1**(10): p. 1970-1976.
129. İrim, Ş.G., et al., *Physical, mechanical and neutron shielding properties of h-BN/Gd2O3/HDPE ternary nanocomposites.* Radiation Physics and Chemistry, 2018. **144**: p. 434-443.
130. Alddrich. *Gadolinium(III) oxide*. Available from: https://www.sigmaaldrich.com/catalog/product/aldrich/637335?lang=en&region=CA.
131. Alddrich. *Bismuth(III) oxide*. Available from: https://www.sigmaaldrich.com/catalog/product/aldrich/637017?lang=en&region=CA.
132. *ESTAR*. Available from: https://physics.nist.gov/PhysRefData/Star/Text/ESTAR.html.
133. Ferreira da Silva, A., et al., *Optical determination of the direct bandgap energy of lead iodide crystals.* Applied physics letters, 1996. **69**(13): p. 1930-1932.
134. Hutter, E.M., et al., *Direct–indirect character of the bandgap in methylammonium lead iodide perovskite.* Nature materials, 2017. **16**(1): p. 115.
135. Intaniwet, A., et al., *Heavy metallic oxide nanoparticles for enhanced sensitivity in semiconducting polymer x-ray detectors.* Nanotechnology, 2012. **23**(23): p. 235502.
136. Wikipedia. *List of semiconductor materials*. Available from: https://en.wikipedia.org/wiki/List_of_semiconductor_materials.
137. Kuan, C.-F., et al., *Mechanical and electrical properties of multi-wall carbon nanotube/poly (lactic acid) composites.* Journal of Physics and Chemistry of Solids, 2008. **69**(5-6): p. 1395-1398.
138. Spitalsky, Z., et al., *Carbon nanotube–polymer composites: chemistry, processing, mechanical and electrical properties.* Progress in polymer science, 2010. **35**(3): p. 357-401.
139. Yang, S.-Y., et al., *Synergetic effects of graphene platelets and carbon nanotubes on the mechanical and thermal properties of epoxy composites.* Carbon, 2011. **49**(3): p. 793-803.
140. Bhowmik, S. and R. Benedictus. *Performance of space durable polymeric nano composite under electromagnetic radiation at Low Earth Orbit*. in *Applied Electromagnetics Conference, 2007. AEMC 2007. IEEE*. 2007. IEEE.
141. S. Iqbal, H., et al., *Processing and Characterization of Space-Durable High-Performance Polymeric Nanocomposite.* Journal of Thermophysics and Heat Transfer, 2011. **25**(1): p. 87-95.

142. Ruan, S., et al., *Toughening high performance ultrahigh molecular weight polyethylene using multiwalled carbon nanotubes.* Polymer, 2003. **44**(19): p. 5643-5654.
143. Williams, G., R. Trask, and I. Bond, *A self-healing carbon fibre reinforced polymer for aerospace applications.* Composites Part A: Applied Science and Manufacturing, 2007. **38**(6): p. 1525-1532.
144. Hu, H., et al., *Study on Composite Material for Shielding Mixed Neutron and< formula formulatype=.* Nuclear Science, IEEE Transactions on, 2008. **55**(4): p. 2376-2384.
145. Park, C., et al. *Polymer-single wall carbon nanotube composites for potential spacecraft applications*. in *Materials Research Society Symposium Proceedings*. 2001. Cambridge Univ Press.
146. Fujii, M., et al., *Measuring the thermal conductivity of a single carbon nanotube.* Physical review letters, 2005. **95**(6): p. 065502.
147. Berber, S., Y.K. Kwon, and D. Tomanek, *Unusually high thermal conductivity of carbon nanotubes.* Physical Review Letters, 2000. **84**(20): p. 4613.
148. Balandin, A.A., et al., *Superior thermal conductivity of single-layer graphene.* Nano letters, 2008. **8**(3): p. 902-907.
149. Yu, A., et al., *Enhanced thermal conductivity in a hybrid graphite nanoplatelet-carbon nanotube filler for epoxy composites*. Advanced Materials, 2008. **20**(24): p. 4740-4744.
150. Huang, H., et al., *Aligned carbon nanotube composite films for thermal management.* Advanced materials, 2005. **17**(13): p. 1652-1656.
151. Haggenmueller, R., et al., *Single wall carbon nanotube/polyethylene nanocomposites: thermal and electrical conductivity.* Macromolecules, 2007. **40**(7): p. 2417-2421.
152. Shenogin, S., et al., *Role of thermal boundary resistance on the heat flow in carbon-nanotube composites*. Journal of Applied Physics, 2004. **95**(12): p. 8136-8144.
153. Zhong, H. and J.R. Lukes, *Interfacial thermal resistance between carbon nanotubes: molecular dynamics simulations and analytical thermal modeling.* Physical Review B, 2006. **74**(12): p. 125403.
154. Sihn, S., et al., *Enhancement of through-thickness thermal conductivity in adhesively bonded joints using aligned carbon nanotubes*. Composites Science and Technology, 2008. **68**(3): p. 658-665.
155. Liao, S.H., et al., *Preparation and properties of carbon nanotube/polypropylene nanocomposite bipolar plates for polymer electrolyte membrane fuel cells*. Journal of Power Sources, 2008. **185**(2): p. 1225-1232.
156. Song, Y.S. and J.R. Youn, *Influence of dispersion states of carbon nanotubes on physical properties of epoxy nanocomposites.* Carbon, 2005. **43**(7): p. 1378-1385.
157. *Chemical bonds*. Available from: http://hyperphysics.phy-astr.gsu.edu/hbase/chemical/bond.html.
158. Carraher Jr, C.E., *Seymour/Carraher's polymer chemistry*. Vol. 16. 2003: CRC Press.
159. *Carbon-fiber-reinforced polymer*. 2014; Available from: http://en.wikipedia.org/wiki/Carbon-fiber-reinforced_polymer.
160. John, R.B., S. ; Gohler, W. ; Willich, G. ; Newerla, A. ; European Space Agency, *Electronic enclosure for SAR antennas made of CFRP*. 2005: ESA Publications, , Noordwijk, The Netherlands:.
161. Brander, T.G., K. ; Katajisto, H. ; Wallin, M. ; European Space Agency, *CFRP electronics housing for a satellite*. 2005, ESA Publications, , Noordwijk, The Netherlands:. p. 95.
162. Castelli, C., et al., *The carbon fibre structure for the extreme ultraviolet imaging spectrometer on the Solar-B satellite.* Proceedings of the Institution of Mechanical Engineers, Part L: Journal of Materials Design and Applications, 2005. **219**(3): p. 177-186.
163. Sickinger, C. and L. Herbeck. *Deployment strategies, analyses and tests for the CFRP booms of a solar sail*.

164. Mazanek, D.D., et al., *Aerothermal analysis and design of the gravity recovery and climate experiment (GRACE) spacecraft*. 2000: Citeseer.
165. Tanahashi, M., *Development of fabrication methods of filler/polymer nanocomposites: With focus on simple melt-compounding-based approach without surface modification of nanofillers.* Materials, 2010. **3**(3): p. 1593-1619.
166. Raman, N., S. Sudharsan, and K. Pothiraj, *Synthesis and structural reactivity of inorganic–organic hybrid nanocomposites–A review.* Journal of Saudi Chemical Society, 2012. **16**(4): p. 339-352.
167. Velasco-Santos, C., et al., *Improvement of thermal and mechanical properties of carbon nanotube composites through chemical functionalization.* Chemistry of materials, 2003. **15**(23): p. 4470-4475.
168. Park, S., et al., *Electrical properties of multi-walled carbon nanotube/poly (methyl methacrylate) nanocomposite.* Current Applied Physics, 2005. **5**(4): p. 302-304.
169. Andrews, R., et al., *Fabrication of carbon multiwall nanotube/polymer composites by shear mixing.* Macromolecular Materials and Engineering, 2002. **287**(6): p. 395-403.
170. Co., S.-A.; Available from: http://www.sigmaaldrich.com/catalog/product/aldrich/182230?lang=en&region=CA.
171. Nanostructured & Amorphous Materials, I.; Available from: http://www.nanoamor.com/inc/sdetail/9928.
172. Cheng, B., et al., *Evaluation of rheological parameters of polymer melts in torque rheometers.* Polymer Testing, 2001. **20**(7): p. 811-818.
173. Freire, E., et al., *Processability of PVDF/PMMA blends studied by torque rheometry.* Materials Science and Engineering: C, 2009. **29**(2): p. 657-661.
174. Farrar, D. and J. Rose, *Rheological properties of PMMA bone cements during curing.* Biomaterials, 2001. **22**(22): p. 3005-3013.
175. Lee, J.K. and C.D. Han, *Evolution of polymer blend morphology during compounding in a twin-screw extruder.* Polymer, 2000. **41**(5): p. 1799-1815.
176. Patil, R., et al. *Physical characteristics of food extrudates-a review*. in *2005 ASAE Annual Meeting*. 2005. American Society of Agricultural and Biological Engineers.
177. Altuglas. *PMMA Altuglas granules*. Available from: http://www.advancedpolymers.co.za/processing-guides/Altuglas/Altuglas%20extrusion%20guidelines.pdf.
178. CMSC. *United McGill MiniBonder Autoclave*. Available from: http://www.egr.msu.edu/cmsc/equipment/united-mcgill-minibonder-autoclave.
179. Andersen, P.G. and F. Lechner, *Co-Rotating Fully Intermeshing Twin-Screw Compounding: Advancement for Improved Performance and Productivity.* Plastics Engineering, 2013. **69**(4): p. 32-38.
180. Methenni, A., et al., *Fluorescence quenching of fluoranthene by maleic anhydride in solution and during nonreactive and reactive twin-screw extrusion.* Polymer Engineering & Science, 2013. **53**(2): p. 295-300.
181. ROSS. *How the Double Planetary Mixer Works*. Available from: http://www.mixers.com/proddetails.asp?ProdID=58#production-tab.
182. Tanguy, P., et al., *Mixing hydrodynamics in a double planetary mixer.* Chemical Engineering Research and Design, 1999. **77**(4): p. 318-324.
183. Liu, D., et al., *An effective mixing for lithium ion battery slurries.* Advances in Chemical Engineering and Science, 2014. **4**(04): p. 515.
184. Qi, C., K. Guo, and Y. Liu, *Preparation and properties of cotton stalk bundles and high-density polyethylene composites using hot-press molding.* Journal of Reinforced Plastics and Composites, 2012. **31**(15): p. 1017-1024.

185. Nam, T.H., et al., *Mechanical and thermal properties and water absorption of jute fiber reinforced poly (butylene succinate) biodegradable composites.* Advanced composite materials, 2012. **21**(3): p. 241-258.
186. Penjumras, P., et al. *Effect of silanecoupling agent on properties of biocomposites based on poly (lactic acid) and durian rind cellulose*. in *IOP Conference Series: Materials Science and Engineering*. 2016. IOP Publishing.
187. Azuddin, M., I. Choudhury, and Z. Taha, *Development and performance evaluation of a low-cost custom-made vertical injection molding machine.* Journal of the Brazilian Society of Mechanical Sciences and Engineering, 2015. **37**(1): p. 79-86.
188. Heckele, M. and W. Schomburg, *Review on micro molding of thermoplastic polymers.* Journal of Micromechanics and Microengineering, 2003. **14**(3): p. R1.
189. Wikipedia. *Raman spectroscopy*. Available from: https://en.wikipedia.org/wiki/Raman_spectroscopy.
190. Takalo, J., et al., *Separating counterfeit and genuine euro banknotes using time-resolved Raman spectroscopy*. 2015.
191. Bokobza, L., *Spectroscopic Techniques for the Characterization of Polymer Nanocomposites: A Review.* Polymers, 2017. **10**(1): p. 7.
192. Rahmat, M. and P. Hubert, *Carbon nanotube–polymer interactions in nanocomposites: a review.* Composites Science and Technology, 2011. **72**(1): p. 72-84.
193. Sundar, L.S., et al., *Enhanced thermal conductivity and viscosity of nanodiamond-nickel nanocomposite nanofluids*. Scientific reports, 2014. **4**: p. 4039.
194. Jalvandi, J., *Novel chemical and physical approaches for sustainable drug release from biodegradable electrospun nanofibres*. 2016.
195. Mansour, S.A., *Study of thermal stabilization for polystyrene/carbon nanocomposites via TG/DSC techniques.* Journal of thermal analysis and calorimetry, 2013. **112**(2): p. 579-583.
196. Kuila, T., et al., *Characterization and properties of in situ emulsion polymerized poly (methyl methacrylate)/graphene nanocomposites.* Composites Part A: Applied Science and Manufacturing, 2011. **42**(11): p. 1856-1861.
197. Zhao, L., et al., *Multifunctional role of an ionic liquid in melt-blended poly (methyl methacrylate)/multi-walled carbon nanotube nanocomposites.* Nanotechnology, 2012. **23**(25): p. 255702.
198. Godge, G.R. 2016; Available from: https://www.researchgate.net/post/How_to_interpret_the_TGA_and_DSC_analysis2.
199. CSZ. *Advanced Test Equipment Rentals*. Available from: https://www.atecorp.com/ATECorp/media/pdfs/data-sheets/Cincinnati-Z-Plus_Brochure.pdf.
200. Han, J.-H. and C.-G. Kim, *Low earth orbit space environment simulation and its effects on graphite/epoxy composites.* Composite structures, 2006. **72**(2): p. 218-226.
201. Russell-Stevens, M., R. Todd, and M. Papakyriacou, *The effect of thermal cycling on the properties of a carbon fibre reinforced magnesium composite.* Materials Science and Engineering: A, 2005. **397**(1-2): p. 249-256.
202. Gao, Y., et al., *Effect of vacuum thermo-cycling on physical properties of unidirectional M40J/AG-80 composites.* Composites Part B: Engineering, 2005. **36**(4): p. 351-358.
203. Pashayi, K., et al., *High thermal conductivity epoxy-silver composites based on self-constructed nanostructured metallic networks.* Journal of Applied Physics, 2012. **111**(10): p. 104310.
204. McNamara, A.J., Y. Joshi, and Z.M. Zhang, *Characterization of nanostructured thermal interface materials–a review.* International Journal of Thermal Sciences, 2012. **62**: p. 2-11.
205. ASTM. *ASTM D5470-95* Available from: https://compass.astm.org/EDIT/html_annot.cgi?D5470+17.

206. Ozcelik, B., A. Ozbay, and E. Demirbas, *Influence of injection parameters and mold materials on mechanical properties of ABS in plastic injection molding.* International Communications in Heat and Mass Transfer, 2010. **37**(9): p. 1359-1365.
207. Ning, F., et al., *Additive manufacturing of carbon fiber reinforced thermoplastic composites using fused deposition modeling.* Composites Part B: Engineering, 2015. **80**: p. 369-378.
208. ASTM. Available from: https://compass.astm.org/EDIT/html_annot.cgi?D638+14.
209. Ozturk, H. and D. Tannant, *Thin spray-on liner adhesive strength test method and effect of liner thickness on adhesion.* International Journal of Rock Mechanics and Mining Sciences, 2010. **47**(5): p. 808-815.
210. Böer, P., L. Holliday, and T.H.-K. Kang, *Interaction of environmental factors on fiber-reinforced polymer composites and their inspection and maintenance: A review.* Construction and Building Materials, 2014. **50**: p. 209-218.
211. DeFelsko. 2015; Available from: http://www.defelsko.com/adhesion-tester/features.htm.
212. Taylor, E.W., et al. *Space radiation resistant hybrid and polymer materials for solar cells*. in *Photovoltaic Specialists Conference (PVSC), 2010 35th IEEE*. 2010. IEEE.
213. Fayazbakhsh, K. and A. Abedian, *Materials selection for applications in space environment considering outgassing phenomenon.* Advances in space research, 2010. **45**(6): p. 741-749.
214. Bokobza, L. and J. Zhang, *Raman spectroscopic characterization of multiwall carbon nanotubes and of composites.* Express Polymer Letters, 2012. **6**(7).
215. Hodkiewicz, J., *Characterizing Carbon Materials with Raman Spectroscopy*. Thermo Fisher Scientific, Madison, WI, USA.
216. Bastwros, M., et al., *Effect of ball milling on graphene reinforced Al6061 composite fabricated by semi-solid sintering.* Composites Part B: Engineering, 2014. **60**: p. 111-118.
217. Song, P., et al., *Fabrication of exfoliated graphene-based polypropylene nanocomposites with enhanced mechanical and thermal properties.* Polymer, 2011. **52**(18): p. 4001-4010.
218. Wu, X.C., et al., *Non-functionalized carbon nanotube binding with hemoglobin.* Colloids and Surfaces B: Biointerfaces, 2008. **65**(1): p. 146-149.
219. Tahermansouri, H., Y. Aryanfar, and E. Biazar, *Synthesis, characterization, and the influence of functionalized multi-walled carbon nanotubes with creatinine and 2-aminobenzophenone on the gastric cancer cells.* Bulletin of the Korean Chemical Society, 2013. **34**(1): p. 149-153.
220. Azizian, J., et al., *Microwave-induced chemical functionalization of carboxylated multi-walled nanotubes with 2, 3-diaminopyridine.* Fullerenes, Nanotubes and Carbon Nanostructures, 2012. **20**(2): p. 183-190.
221. Jin, Z., et al., *Dynamic mechanical behavior of melt-processed multi-walled carbon nanotube/poly (methyl methacrylate) composites.* Chemical Physics Letters, 2001. **337**(1-3): p. 43-47.
222. Plastics, L.; Available from: http://llamasplastics.com.
223. TRIUMF. *About TRIUMF*. Available from: http://www.triumf.ca/home/about-triumf.
224. Garnett, R.W. and R.L. Sheffield, *Overview of Accelerator Applications in Energy.* Reviews of Accelerator Science and Technology, 2015. **8**: p. 1-25.
225. Singh, D., et al., *Radiation induced modification of dielectric and structural properties of Cu/PMMA polymer composites.* Journal of Non-Crystalline Solids, 2010. **356**(18-19): p. 856-863.
226. Zhang, R. and W.D. Newhauser, *Calculation of water equivalent thickness of materials of arbitrary density, elemental composition and thickness in proton beam irradiation.* Physics in Medicine & Biology, 2009. **54**(6): p. 1383.
227. *SRIM*. Available from: http://srim.org/.
228. Wikipedia. *Linear particle accelerator*. Available from: https://en.wikipedia.org/wiki/Linear_particle_accelerator.

229. Purdy, J.A., et al., *Physics of Radiotherapy Planning and Delivery*, in *Technical Basis of Radiation Therapy*. 2011, Springer. p. 85-132.
230. Miller, J., et al., *Benchmark studies of the effectiveness of structural and internal materials as radiation shielding for the international space station.* Radiation research, 2003. **159**(3): p. 381-390.
231. Cucinotta, F.A., M.-H.Y. Kim, and L.J. Chappell, *Evaluating shielding approaches to reduce space radiation cancer risks.* NASA Center for AeroSpace Information, 2012: p. 1-35.
232. Barth, J.L., *Space and atmospheric environments: from low earth orbits to deep space*, in *Protection of Materials and Structures from Space Environment*. 2003, Springer. p. 7-29.
233. Wilson, J., et al., *Shielding strategies for human space exploration*. Vol. 6. 1997: NASA Washington DC.
234. Schimmerling, W., F. Cucinotta, and J. Wilson, *Radiation risk and human space exploration*, in *Advances in Space Research*. 2003. p. 27-34.
235. Cucinotta, F.A., *Space radiation organ doses for astronauts on past and future missions*. 2007.
236. Cucinotta, F.A., H. Wang, and J.L. Huff, *Risk of acute or late central nervous system effects from radiation exposure.* NASA Human Research Program Roadmap, 2012.
237. Cucinotta, F.A., et al., *Space radiation risks to the central nervous system.* Life Sciences in Space Research, 2014. **2**: p. 54-69.
238. Thibeault, S.A., et al., *Nanomaterials for radiation shielding.* MRS Bulletin, 2015. **40**(10): p. 836-841.
239. Adams Jr, J., et al., *Revolutionary concepts of radiation shielding for human exploration of space.* 2005.
240. Kodaira, S., et al., *Verification of shielding effect by the water-filled materials for space radiation in the International Space Station using passive dosimeters*. Advances in Space Research, 2014. **53**(1): p. 1-7.
241. Nambiar, S. and J.T. Yeow, *Polymer-composite materials for radiation protection.* ACS applied materials & interfaces, 2012. **4**(11): p. 5717-5726.
242. Atwell, W., et al., *Metal Hydrides, MOFs, and Carbon Composites as Space Radiation Shielding Mitigators.* 2014.
243. Yuan, B., et al., *Electrical conductive and graphitizable polymer nanofibers grafted on graphene nanosheets: improving electrical conductivity and flame retardancy of polypropylene.* Composites Part A: Applied Science and Manufacturing, 2016.
244. Yu, J.W., et al., *Enhancement of the crosslink density, glass transition temperature, and strength of epoxy resin by using functionalized graphene oxide co-curing agents.* Polymer Chemistry, 2016. **7**(1): p. 36-43.
245. Özdemir, T., et al., *Neutron shielding of EPDM rubber with boric acid: Mechanical, thermal properties and neutron absorption tests.* Progress in Nuclear Energy, 2016. **89**: p. 102-109.
246. El Miri, N., et al., *Synergistic effect of cellulose nanocrystals/graphene oxide nanosheets as functional hybrid nanofiller for enhancing properties of PVA nanocomposites.* Carbohydrate polymers, 2016. **137**: p. 239-248.
247. Li, B., C. Cai, and X. Chen, *Discontinuous conductive filler polymer-matrix composites for electromagnetic shielding*. 2015, Google Patents.
248. Chai, H., et al., *Preparation and properties of flexible flame-retardant neutron shielding material based on methyl vinyl silicone rubber.* Journal of Nuclear Materials, 2015. **464**: p. 210-215.
249. Ayyıldız, S., et al., *A Nanocomposite Shield Constructed for Protection Against the Harmful Effects of Dental X-Rays.* Journal of Dentistry of Tehran University of Medical Sciences, 2015. **12**(5): p. 364-373.

250. Kim, J., et al., *Nano - W Dispersed Gamma Radiation Shielding Materials.* Advanced Engineering Materials, 2014. **16**(9): p. 1083-1089.
251. Nelson, A., et al., *Effect of Proton Irradiation on the Electrical Resistivity of Carbon Nanotube-Epoxy Composites*. Nanoscience and Nanotechnology Letters, 2015. **7**(2): p. 157-161.
252. Jackson, E.M., et al., *Development and thermal properties of carbon nanotube-polymer composites*. Composites Part B: Engineering, 2016.
253. Gupta, P., et al., *Electric field and current assisted alignment of CNT inside polymer matrix and its effects on electrical and mechanical properties.* Polymer, 2016. **89**: p. 119-127.
254. Huseynov, E., A. Garibov, and R. Mehdiyeva, *Influence of neutron irradiation and temperature on the electric conductivity of SiO_2 nanoparticles*. Journal of Electrostatics, 2015. **74**: p. 73-78.
255. Almajid, A., et al., *Effects of graphene and CNT on mechanical, thermal, electrical and corrosion properties of vinylester based nanocomposites.* Plastics, Rubber and Composites, 2015. **44**(2): p. 50-62.
256. Banhart, F., *Irradiation effects in carbon nanostructures.* Reports on progress in physics, 1999. **62**(8): p. 1181.
257. Pircheraghi, G., et al., *Effect of carbon nanotube dispersion and network formation on thermal conductivity of thermoplastic polyurethane/carbon nanotube nanocomposites.* Polymer Engineering & Science, 2016.
258. Khare, K.S., F. Khabaz, and R. Khare, *Effect of carbon nanotube functionalization on mechanical and thermal properties of cross-linked epoxy–carbon nanotube nanocomposites: role of strengthening the interfacial interactions*. ACS applied materials & interfaces, 2014. **6**(9): p. 6098-6110.
259. Zeitlin, C., et al., *Measurements of materials shielding properties with 1GeV/nuc 56 Fe.* Nuclear Instruments and Methods in Physics Research Section B: Beam Interactions with Materials and Atoms, 2006. **252**(2): p. 308-318.
260. Suarez, J.C.M., et al., *Influence of γ-irradiation on poly (methyl methacrylate)*. Journal of applied polymer science, 2002. **85**(4): p. 886-895.
261. deGroh, K.K., et al., *NASA Glenn Research Center's Materials International Space Station Experiments (MISSE 1-7)*. 2008.
262. Mancusi, D., et al., *Comparison of aluminum and lucite for shielding against 1GeV protons.* Advances in Space Research, 2007. **40**(4): p. 581-585.
263. Durante, M., *Influence of the shielding on the space radiation biological effectiveness.* Physica Medica, 2001. **17**: p. 269-271.
264. Zhang, R. and W.D. Newhauser, *Calculation of water equivalent thickness of materials of arbitrary density, elemental composition and thickness in proton beam irradiation.* Physics in medicine and biology, 2009. **54**(6): p. 1383.
265. Li, Z., et al., *PDMS/single-walled carbon nanotube composite for proton radiation shielding in space applications.* Materials Letters, 2013. **108**: p. 79-83.
266. Arshak, K. and O. Korostynska, *Advanced materials and techniques for radiation dosimetry*. 2006: Artech House Boston.
267. Filleter, T. and H. Espinosa, *Multi-scale mechanical improvement produced in carbon nanotube fibers by irradiation cross-linking.* Carbon, 2013. **56**: p. 1-11.
268. Porter, H., C. Jackman, and A. Green, *Efficiencies for production of atomic nitrogen and oxygen by relativistic proton impact in air.* The Journal of Chemical Physics, 1976. **65**(1): p. 154-167.
269. Peterson, J.D., S. Vyazovkin, and C.A. Wight, *Stabilizing effect of oxygen on thermal degradation of poly (methyl methacrylate)*. Macromolecular rapid communications, 1999. **20**(9): p. 480-483.

270. Grossman, E. and I. Gouzman, *Space environment effects on polymers in low earth orbit.* Nuclear Instruments and Methods in Physics Research Section B: Beam Interactions with Materials and Atoms, 2003. **208**: p. 48-57.
271. Lin, R. *Energetic electrons accelerated in solar particle events*. in *AIP Conference Proceedings*. 2000. AIP.
272. Webber, W. and T. Villa, *The Galactic Cosmic Ray Electron Spectrum from 3 to 70 MeV Measured by Voyager 1 Beyond the Heliopause, What This Tells Us About the Propagation of Electrons and Nuclei In and Out of the Galaxy at Low Energies.* arXiv preprint arXiv:1703.10688, 2017.
273. Charlesby, A., *Atomic Radiation and Polymers: International Series of Monographs on Radiation Effects in Materials*. Vol. 1. 2013: Elsevier.
274. Bolton, S., et al., *Ultra-relativistic electrons in Jupiter's radiation belts*. Nature, 2002. **415**(6875): p. 987.
275. Smith, D.M., et al., *The RHESSI spectrometer.* Solar Physics, 2002. **210**(1-2): p. 33-60.
276. Cucinotta, F.A., *Review of NASA approach to space radiation risk assessments for Mars exploration.* Health physics, 2015. **108**(2): p. 131-142.
277. Units, I.C.o.R. and Measurements, *Radiation Dosimetry: Electron Beams with Energies Between 1 and 50 MeV; 2nd Reprint*. 1984: International Commission on Radiation Units and Measurements.
278. Dapor, M., *Electron-Beam Interactions with Solids: Application of the Monte Carlo Method to Electron Scattering Problems*. Vol. 7. 2003: Springer Science & Business Media.
279. Najafi, E. and K. Shin, *Radiation resistant polymer–carbon nanotube nanocomposite thin films.* Colloids and Surfaces A: Physicochemical and Engineering Aspects, 2005. **257**: p. 333-337.
280. Bhowmik, S., et al., *High-performance nanoadhesive bonding of space-durable polymer and its performance under space environments.* Journal of Spacecraft and Rockets, 2009. **46**(1): p. 218-224.
281. Hashimoto, N., et al., *In-Situ Observations of Microstructure Evolution in Electron-Irradiated Multi-Wall Carbon Nanotubes.* Materials Transactions, 2014. **55**(3): p. 458-460.
282. Chen, S., et al. *Polymer nanocomposite for space applications*. in *Nanotechnology (IEEE-NANO), 2014 IEEE 14th International Conference on*. 2014. IEEE.
283. Li, L., J. Su, and X. Zhu, *Non-uniform shrinkage of multiple-walled carbon nanotubes under in situ electron beam irradiation.* Applied Physics A, 2016. **122**(10): p. 912.
284. Li, Z., et al., *PMMA/MWCNT nanocomposite for proton radiation shielding applications.* Nanotechnology, 2016. **27**(23): p. 234001.
285. Yang, J., et al., *Effects of electron irradiation on LDPE/MWCNT composites.* Nuclear Instruments and Methods in Physics Research Section B: Beam Interactions with Materials and Atoms, 2015. **365**: p. 55-60.
286. McCaffrey, J., F. Tessier, and H. Shen, *Radiation shielding materials and radiation scatter effects for interventional radiology (IR) physicians.* Medical physics, 2012. **39**(7): p. 4537-4546.
287. Cho, J., M. Kim, and J. Rhim, *Comparison of radiation shielding ratios of nano-sized bismuth trioxide and molybdenum.* Radiation Effects and Defects in Solids, 2015. **170**(7-8): p. 651-658.
288. Ambika, M., N. Nagaiah, and S. Suman, *Role of bismuth oxide as a reinforcer on gamma shielding ability of unsaturated polyester based polymer composites.* Journal of Applied Polymer Science, 2017. **134**(13).
289. Cengel, K.A., et al., *Using electron beam radiation to simulate the dose distribution for whole body solar particle event proton exposure.* Radiation and environmental biophysics, 2010. **49**(4): p. 715-721.

290. Fan, Z., et al., *Advanced multifunctional graphene aerogel–Poly (methyl methacrylate) composites: Experiments and modeling.* Carbon, 2015. **81**: p. 396-404.
291. nan Shen, J., et al., *Preparation and characterization of thin-film nanocomposite membranes embedded with poly (methyl methacrylate) hydrophobic modified multiwalled carbon nanotubes by interfacial polymerization.* Journal of membrane science, 2013. **442**: p. 18-26.
292. Weng, B., et al., *Mass production of carbon nanotube reinforced poly (methyl methacrylate) nonwoven nanofiber mats.* Carbon, 2014. **75**: p. 217-226.
293. Thirsk, R., et al., *The space-flight environment: the International Space Station and beyond.* Canadian Medical Association Journal, 2009. **180**(12): p. 1216-1220.
294. Martel-Estrada, S., et al. *The effect of radiation on the thermal properties of chitosan/mimosa tenuiflora and chitosan/mimosa tenuiflora/multiwalled carbon nanotubes (MWCNT) composites for bone tissue engineering*. in *AIP Conference Proceedings*. 2014. AIP.
295. Petersen, E.J., et al., *Methods to assess the impact of UV irradiation on the surface chemistry and structure of multiwall carbon nanotube epoxy nanocomposites*. Carbon, 2014. **69**: p. 194-205.
296. Savinov, R., *EVALUATION OF EFFICIENCY OF VARIOUS MATERIALS TO SHIELD FROM RADIATION IN SPACE USING THE MONTE CARLO TRANSPORT CODE CALLED FLUKA*. 2016.
297. Thibeault, S.A., et al., *Radiation Shielding Materials Containing Hydrogen, Boron, and Nitrogen: Systematic Computational and Experimental Study. Phase I.* 2012.
298. Estevez, J.E., et al., *Simulation of hydrogenated boron nitride nanotube's mechanical properties for radiation shielding applications.* Int. J. Chem. Sci. Eng, 2014. **8**: p. 63-67.
299. Emmanuel, A., *Design and development of a multifunctional composite radiation shield for space applications*. 2016.
300. Galehdari, N.A., V. Mani, and A.D. Kelkar, *Fabrication of Nanoengineered Radiation Shielding Multifunctional Polymeric Sandwich Composites.* Int. J. Chem. Mol. Nucl. Mater. Metall. Eng, 2016. **10**: p. 257-260.
301. Mani, V., N.S. Prasad, and A. Kelkar. *Ultra high molecular weight polyethylene (UHMWPE) fiber epoxy composite hybridized with Gadolinium and Boron nanoparticles for radiation shielding*. in *Planetary Defense and Space Environment Applications*. 2016. International Society for Optics and Photonics.
302. kiehl, c., et al., *on-line ultrasonic measurements of methyl methacrylate polymerization for application to reactive extrusion.* polymer engineering & science, 2001. **41**(6): p. 1078–1086.
303. Marc Dr. Husemann, S.D.Z., *Processing of acrylate hot melt adhesives via reactive extrusion*. 2003.
304. Industries, M.; Available from: http://mauco-ind.com/en/products/sheets/acrylic-sheet-pmma/acrylic-extruded/.
305. Nationwide Plasitcs, I.
306. International, L.; Available from: http://www.luciteinternational.com/products-and-brands/eame/perspex-general-purpose-sheet
307. Zhang, A., et al., *Study on mechanical and flow properties of acrylonitrile - butadiene - styrene/poly (methyl methacrylate)/nano - calcium carbonate composites.* Polymer Composites, 2010. **31**(9): p. 1593-1602.
308. Camenzind, A., et al., *Structure & strength of silica-PDMS nanocomposites.* Polymer, 2010. **51**(8): p. 1796-1804.
309. Matayabas Jr, J.C. and P.A. Koning, *Phase change thermal interface materials including polyester resin*. 2008, Google Patents.

310. Lertwimolnun, W. and B. Vergnes, *Effect of processing conditions on the formation of polypropylene/organoclay nanocomposites in a twin screw extruder.* Polymer Engineering & Science, 2006. **46**(3): p. 314-323.
311. Zheng, W., X. Lu, and S.C. Wong, *Electrical and mechanical properties of expanded graphite-reinforced high-density polyethylene.* Journal of Applied Polymer Science, 2004. **91**(5): p. 2781-2788.
312. Müller, M.T., et al., *Influence of feeding conditions in twin-screw extrusion of PP/MWCNT composites on electrical and mechanical properties.* Composites Science and Technology, 2011. **71**(13): p. 1535-1542.
313. Liu, S.-P., et al., *Mechanical properties of polyamide-6/montmorillonite nanocomposites—Prepared by the twin-screw extruder mixed technique.* International Communications in Heat and Mass Transfer, 2011. **38**(1): p. 37-43.
314. Chen, R.S., et al., *Influence of Screw Speed on the Mechanical Properties of Twin-Screw Extruded Rice Husk Flour Recycled Thermoplastic Composites* in *International Conference on Agricultural, Ecological and Medical Sciences (AEMS-2015)* 2015: Penang (Malaysia).
315. Hong, J., et al., *Effect of dispersion state of carbon nanotube on the thermal conductivity of poly (dimethyl siloxane) composites.* Current Applied Physics, 2010. **10**(1): p. 359-363.
316. Varela-Rizo, H., et al., *Processing and functionalization effect in CNF/PMMA nanocomposites.* Composites Part A: Applied Science and Manufacturing, 2012. **43**(4): p. 711-721.
317. Pradhan, A.K. and S.K. Swain, *Oxygen barrier of multiwalled carbon nanotube/polymethyl methacrylate nanocomposites prepared by in situ method.* Journal of Materials Science & Technology, 2012. **28**(5): p. 391-395.
318. Li, M., et al., *Preparation, solubility, and electrorheological properties of carbon nanotubes/poly (methyl methacrylate) nanocomposites by in situ functionalization.* Composites Part A: Applied Science and Manufacturing, 2009. **40**(4): p. 413-417.
319. Liu, X.-Q., et al., *Reinforcement and plasticization of PMMA grafted MWCNTs for PVDF composites.* Composites Part B: Engineering, 2013. **53**: p. 9-16.
320. Lock, N., et al., *Elucidating negative thermal expansion in MOF-5.* The Journal of Physical Chemistry C, 2010. **114**(39): p. 16181-16186.
321. Tipler, P.A. and G. Mosca, *Physics for scientists and engineers*. 2007: Macmillan.
322. Kumar, S., et al., *Development and characterization of polymer–ceramic continuous fiber reinforced functionally graded composites for aerospace application.* Aerospace Science and Technology, 2013. **26**(1): p. 185-191.
323. *Thermal expansion*. 2015; Available from: https://en.wikipedia.org/wiki/Thermal_expansion#cite_note-12.
324. Ahmed, A., et al. *STUDY OF THERMAL EXPANSION IN CARBON FIBER-REINFORCED POLYMER COMPOSITES*. in *SAMPE International Symposium Proceedings*. 2012.
325. Ahmed, A., et al., *STUDY OF THERMAL EXPANSION IN CARBON FIBER-REINFORCED POLYMER COMPOSITES.*
326. Wang, S., et al., *Thermal expansion of graphene composites.* Macromolecules, 2009. **42**(14): p. 5251-5255.
327. Pramoda, K., et al., *Thermo-mechanical properties of poly (vinylidene fluoride) modified graphite/poly (methyl methacrylate) nano composites.* Composites Science and Technology, 2010. **70**(4): p. 578-583.
328. Logakis, E., et al., *Highly conducting poly (methyl methacrylate)/carbon nanotubes composites: Investigation on their thermal, dynamic-mechanical, electrical and dielectric properties.* Composites Science and Technology, 2011. **71**(6): p. 854-862.
329. Kalakonda, P. and S. Banne, *Thermomechanical properties of PMMA and modified SWCNT composites.* Nanotechnology, science and applications, 2017. **10**: p. 45.

330. Barrau, S., et al., *Glass transition temperature depression at the percolation threshold in carbon nanotube–epoxy resin and polypyrrole–epoxy resin composites.* Macromolecular rapid communications, 2005. **26**(5): p. 390-394.
331. Davies, P., et al., *Influence of adhesive bond line thickness on joint strength.* International Journal of Adhesion and Adhesives, 2009. **29**(7): p. 724-736.
332. Jumaat, M., M. Rahman, and M. Rahman, *Review on bonding techniques of CFRP in strengthening concrete structures.* International Journal of Physical Sciences, 2011. **6**(15): p. 3567-3575.
333. Mandolfino, C., E. Lertora, and C. Gambaro, *Cold Plasma Pretreatment of Carbon Fibre Composite Substrates to Improve Adhesive Bonding Performance.* Advances in Aerospace Engineering, 2014. **2014**.
334. Hutchinson, J.W., *Stresses and failure modes in thin films and multilayers.* Notes for a Dcamm Course. Technical University of Denmark, Lyngby, 1996: p. 1-45.
335. Badavi, F., D. Adams, and J. Wilson. *Validity of the aluminum equivalent approximation in space radiation shielding*. in *40th International Conference on Environmental Systems*. 2009.
336. Cucinotta, F., M. Kim, and L. Ren, *Managing lunar and Mars mission radiation risks*. 2005, Center for Aerospace Information Hanover, MD.

Appendix Outgassing Test

(i) Preparation and Process of Outgassing Test

Outgassing test of our samples was finished in an outgassing facility at Integrity Testing Laboratory, which is capable to achieve reliable data based on ASTM E595. PMMA and PMMA with 3wt% MWCNT nanocomposite were dried in vacuum oven and prepared with diameters of 1.5 to 3.0 mm (shown in Figure 77). Each material was split into 4 groups, which were loaded into different specimen boats (shown in Figure 78).

Figure 77: PMMA and Nanocomposite

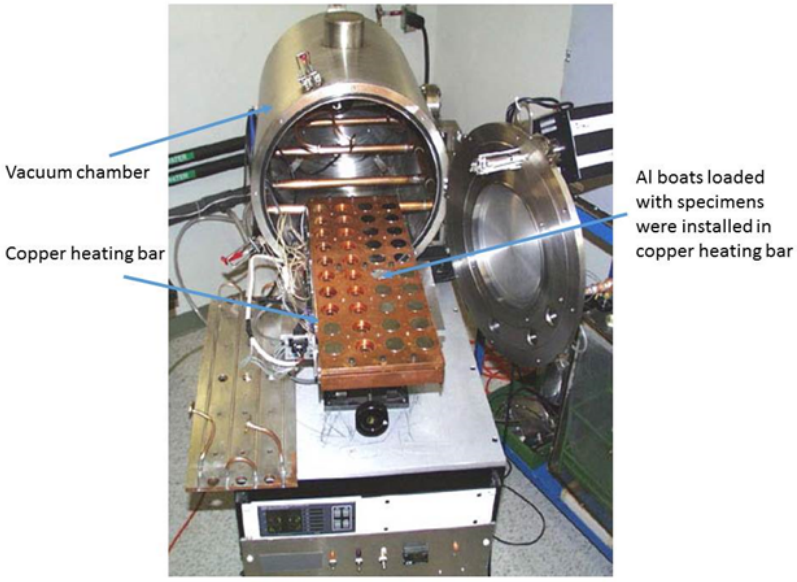

Figure 78: Outgassing Test Setup

The testing process took about 4 days and the details have been listed below:

1. The samples were small enough to place into the Al boats that, in turn, must fit into the specimen compartments of the copper heating bar.
2. The specimens were placed into the Al boats prepared for outgassing according to the ASTM E 595. The boats with specimens were conditioned at 23°C and 50% relative humidity for 24 hours.
3. After weighting, the boats were placed in the specimen compartments of the copper heating bar of the outgassing system.
4. The rows and the lines of cells in the copper heating bar were marked with figures and letters providing a unique identification number for each cell. Similar markings were used for all sites on the collector side.
5. The temperature of the chromium-plated collector plates was held at 25°C ± 0.5°C.
6. The temperature of the copper heating bar was held at 125°C.
7. The vacuum pressure in the outgassing chamber was maintained at ~10^{-6} Torr during the outgassing process.
8. The duration of the outgassing test was 24 hours.
9. The heating was turned off after 24 hours and the samples were removed from the chamber after the samples were cool enough to handle.
10. All specimens and the chromium-plated collector plates were weighted again.
11. All specimens were weighted again after conditioning for 24 hours at 23°C and 50% relative humidity.

(ii) Results of Outgassing Test

The averages of results from 4 groups were calculated for each material. The detailed results of PMMA and PMMA/MWCNT (3wt%) nanocomposite have been listed in Table 33 and Table 34.

Table 33: Total Mass Loss of PMMA and PMMA/MWCNT (3wt%)

Cups empty (g)	Cups + sample before test	Sample mass before test	Cups + sample just after test	Sample mass after test	Mass loss (g)	TML %	**TML % average**
Pure PMMA							
0.070124	0.251383	0.181259	0.250685	0.180561	0.000698	0.39	**0.40**
0.070843	0.247736	0.176893	0.247084	0.176241	0.000652	0.37	
0.069487	0.252299	0.182812	0.251494	0.182007	0.000805	0.44	
0.069955	0.255434	0.185479	0.254667	0.184712	0.000767	0.41	
PMMA/MWCNT (3wt%)							
0.070215	0.195627	0.125412	0.195088	0.124873	0.000539	0.43	**0.44**
0.069982	0.217410	0.147428	0.216762	0.146780	0.000648	0.44	
0.069524	0.211593	0.142069	0.210943	0.141419	0.000650	0.46	
0.069469	0.218068	0.148599	0.217439	0.147970	0.000629	0.42	

Table 34: CVCM and WVR of PMMA and PMMA/MWCNT (3wt%) Nanocomposite

Collectors before test (g)	Collectors after test (g)	Deposited Mass (g)	CVCM %	**CVCM % average**	Cups+sample after hygro (g)	Mass change after hygro (g)	WVR %	**WVR % average**
Pure PMMA								
0.250685	0.180561	0.000698	0.39	**0.01**	0.251243	0.000558	0.31	**0.31**
0.247084	0.176241	0.000652	0.37		0.247624	0.000540	0.31	
0.251494	0.182007	0.000805	0.44		0.252071	0.000577	0.32	
0.254667	0.184712	0.000767	0.41		0.255238	0.000571	0.31	
PMMA/MWCNT (3wt%)								
0.195088	0.124873	0.000539	0.43	**0.01**	0.195468	0.000380	0.30	**0.31**
0.216762	0.146780	0.000648	0.44		0.217215	0.000453	0.31	
0.210943	0.141419	0.000650	0.46		0.211377	0.000434	0.31	
0.217439	0.147970	0.000629	0.42		0.217901	0.000462	0.31	

It is clear to see that all materials, PMMA and nanocomposite have passed low outgassing test based on ASTM E 595 standard, which is developed by NASA. The TML and CVCM of each set of our samples are well below the limits. The average TML of PMMA/MWCNT (3wt%) is about 10% higher than the result of pure PMMA, but it is still much lower than the limit of 1.0% recommended by the standard. Moreover, the averages of CVCM of both materials are below the percentage of 0.02%, much smaller than the limit value of 0.1%. The mass loss may be due to outgassing of low molecular weight materials, such as residual solvent, surface contaminants and entrapped process solutions.